Comparison of Electron Elastic-Scattering Cross Sections Calculated from Two Commonly Used Atomic Potentials

A. Jablonski[a)]
Institute of Physical Chemistry, Polish Academy of Sciences, ul. Kasprzaka 44/52, 01-224 Warsaw, Poland

F. Salvat[b)]
Facultat de Fisica (ECM), Universitat de Barcelona, Diagonal 647, 08028 Barcelona, Spain

C. J. Powell[c)]
Surface and Microanalysis Science Division, National Institute of Standards and Technology, Gaithersburg, Maryland 20899-8370

(Received 22 January 2003; revised manuscript received 29 May 2003; accepted 3 June 2003; published online 26 March 2004)

We have analyzed differential cross sections (DCSs) for the elastic scattering of electrons by neutral atoms that have been derived from two commonly used atomic potentials: the Thomas–Fermi–Dirac (TFD) potential and the Dirac–Hartree–Fock (DHF) potential. DCSs from the latter potential are believed to be more accurate. We compared DCSs for six atoms (H, Al, Ni, Ag, Au, and Cm) at four energies (100, 500, 1000, and 10 000 eV) from two databases issued by the National Institute of Standards and Technology in which DCSs had been obtained from the TFD and DHF potentials. While the DCSs from the two potentials had similar shapes and magnitudes, there can be pronounced deviations (up to 70%) for small scattering angles for Al, Ag, Au, and Cm. In addition, there were differences of up to 400% at scattering angles for which there were deep minima in the DCSs; at other angles, the differences were typically less than 20%. The DCS differences decreased with increasing electron energy. DCSs calculated from the two potentials were compared with measured DCSs for six atoms (He, Ne, Ar, Kr, Xe, and Hg) at energies between 50 eV and 3 keV. For Ar, the atom for which experimental data are available over the largest energy range there is good agreement between the measured DCSs and those calculated from the TFD and DHF potentials at 2 and 3 keV, but the experimental DCSs agree better with the DCSs from the DHF potential at lower energies. A similar trend is found for the other atoms. At energies less than about 1 keV, there are increasing differences between the measured DCSs and the DCSs calculated from the DHF potential. These differences were attributed to the neglect of absorption and polarizability effects in the calculations. We compare transport cross sections for H, Al, Ni, Ag, Au, and Cm obtained from the DCSs for each potential. For energies between 200 eV and 1 keV, the largest differences are about 20% (for H, Au, and Cm); at higher energies, the differences are smaller. We also examine the extent to which three quantities derived from DCSs vary depending on whether the DCSs were obtained from the TFD or DHF potential. First, we compare calculated and measured elastic-backscattered intensities for thin films of Au on a Ni substrate with different measurement conditions, but it is not clear whether DCSs from the TFD or DHF potential should be preferred. Second, we compare electron inelastic mean free paths (IMFPs) derived from relative and absolute measurements by elastic-peak electron spectroscopy and from analyses with DCSs obtained from the TFD and DHF potentials. In four examples, for a variety of materials and measurement conditions, we find differences between the IMFPs from the TFD and DHF potentials ranging from 1.3% to 17.1%. Third, we compare mean escape depths for two photoelectron lines and two Auger-electron lines in solid Au obtained using DCSs from the TFD and DHF potentials. The relative differences between these mean escape depths

[a)]Electronic mail: jablo@ichf.edu.pl
[b)]Electronic mail: cesc@ecm.ub.es
[c)]Electronic mail: cedric.powell@nist.gov

vary from 4.3% at 70 eV to0.5% at 2016 eV at normal electron emission, and become smaller with increasing emission angle. Although measured DCSs for atoms can differ from DCSs calculated from the DHF potential by up to a factor of 2, we find that the atomic DCSs are empirically useful for simulations of electron transport in solids for electron energies above about 300 eV. The atomic DCSs can also be useful for energies down to at least 200 eV if relative measurements are made.
[DOI: 10.1063/1.1595653]

Key words: Auger electron spectroscopy, differential cross section, Dirac–Hartree–Fock potential, elastic electron scattering, elastic-peak electron spectroscopy, electron transport, solid surfaces, surface analysis, Thomas–Fermi–Dirac potential, x-ray photoelectron spectroscopy

Contents

List of Tables

List of Figures

1. Introduction

The elastic scattering of electrons by atoms, molecules, and solids is of widespread importance in many applications ranging from radiation dosimetry, radiation therapy, radiation processing, radiation sensors, and radiation protection to electron-beam lithography, plasma physics, and materials analysis by techniques such as electron-probe microanalysis (EPMA), analytical electron microscopy (AEM), Auger-electron spectroscopy (AES), and x-ray photoelectron spectroscopy (XPS). For these applications, knowledge of elastic-scattering cross sections can be needed to obtain information on the spatial distribution of energy deposition, to enable more accurate analyses, or to define the analytical volume. More specifically, data for differential elastic-scattering cross sections, total elastic-scattering cross sections, transport cross sections, or phase shifts may be required.

Elastic-electron-scattering phenomena in solids and liquids can be very different from the corresponding phenomena for the constituent atoms or molecules in the gas phase at pressures for which multiple elastic or inelastic scattering can be ignored. For crystalline solids, coherent scattering by the ordered atoms leads to electron diffraction, a powerful tool for obtaining information on the atomic structure. As the degree of atomic order decreases (e.g., for an amorphous solid, a liquid, or a polycrystalline solid consisting of many randomly oriented grains or assemblies of molecules), the diffraction effects become weaker and can be neglected for many practical purposes. Atomic elastic-scattering cross sections can then be used for describing electron transport in solids. Two other differences between elastic scattering of electrons by neutral atoms and by solids (differences in interaction potential and the occurrence of multiple scattering) will be discussed below.

We consider here data describing elastic scattering of electrons by neutral atoms for energies between 50 eV and 300 keV, although particular attention will be given to data for energies between 50 eV and 10 keV. Differential elastic-scattering cross sections, total elastic-scattering cross sections, and transport cross sections have been calculated and tabulated elsewhere for many elements, as indicated in Table 1.[1–12] There are also a limited number of measurements of these cross sections for certain elements and energies, and there are measurements of other parameters for certain solids and energies (to be discussed below) that depend on elastic-scattering cross sections. The latter measurements, in particular, provide indirect validation of the cross-section data. The present calculations of cross sections are valuable, however, because they can be made for all elements and for a wide range of energies, and are thus of general applicability.

There can be noticeable differences among cross-section data from the sources listed in Table 1. These differences mainly arise from the different theoretical models used in the calculations (e.g., relativistic or nonrelativistic theory used for description of the scattering event) or from differences in electrostatic potentials describing interaction with the target atom. The main characteristics of the available databases of differential elastic-scattering cross sections and/or total elastic-scattering cross sections available in the literature are shown in Table 1.

The theoretical models used for the calculation of atomic electron densities and/or atomic potentials are shown in Table 2. All of these models disregard electron correlations, i.e., the fact that a single determinant is not the most general wave function for the set of atomic electrons. Correlation is partially accounted for in the so-called multiconfigurational methods in which the trial function is approximated by a

linear combination of several Slater determinants corresponding to a set of configurations with energies close to that of the ground state.

The potentials that are used in published calculations of elastic-scattering cross sections can be roughly classified into two groups:

(1) potentials resulting from the statistical model of the atom, i.e. the Thomas–Fermi (TF) potential or the Thomas–Fermi–Dirac (TFD) potential; and
(2) potentials derived for atoms from relativistic or nonrelativistic Hartree–Fock self-consistent methods, e.g., the relativistic Dirac–Hartree–Fock (DHF) potential (Table 2) considered in the present work.

Elastic-scattering cross sections derived from the TFD potential have been frequently used in theoretical descriptions (e.g., by Monte Carlo simulations) of electron transport in solids.[13–35] Similar calculations have been made with elastic-scattering cross sections from the DHF potential.[36–45] These and related calculations have been performed for applications in surface analysis by AES (incident electron energies typically between 5 and 25 keV, and detected electron energies generally from 50 to 2500 eV) and XPS (detected electron energies typically from 200 to 1500 eV), and in bulk and thin-film analysis by EPMA (incident electron energies typically between 5 and 30 keV) and AEM (incident energies typically between 50 and 300 keV). Because self-consistent calculations provide a more accurate description of atomic structure, we expect that elastic-scattering cross sections based on the DHF potential will be more accurate than cross sections calculated from the TFD potential. As a result, electron-transport calculations are expected to be more reliable if the elastic-scattering cross sections were obtained from the DHF potential rather than from the TFD potential. The question then arises as to the magnitude of the difference between these cross sections, particularly in view of the frequent use of the latter cross sections.

We make systematic comparisons here of differential elastic-scattering cross sections and of transport cross sections (derived from the differential cross sections as indicated below) from the TFD and DHF potentials in order to determine the magnitudes of differences in these cross sections for a range of electron energies. These comparisons are made for six elements spanning a large range of atomic number, Z, i.e., H ($Z=1$), Al ($Z=13$), Ni ($Z=28$), Ag ($Z=47$), Au ($Z=79$), and Cm ($Z=96$). Most of the comparisons are made with cross sections obtained from two National Institute of Standards and Technology (NIST) databases, one which provided cross sections from the TFD potential[10] and the other which provided cross sections from the DHF potential.[12] These comparisons are made for electron energies between 100 and 10 000 eV, the energy range common to both databases. Additional comparisons have been made between cross sections from the latter database and those from another NIST database[11] for which the DHF potential was also used but for which a different exchange correction was applied. Comparisons were also made between differential cross sections from the TFD[10] and DHF[12] potentials and measurements of these cross sections for the rare gases and mercury.

We begin with a description of calculations of differential elastic-scattering cross sections by the partial-wave expansion method (PWEM) in Sec. 2. Information on calculations of differential cross sections from the TFD and DHF potentials is presented in Secs. 3 and 4, respectively. The transport cross section, a useful parameter in descriptions of signal-electron transport in AES and XPS, is defined in Sec. 5. We present comparisons of the TFD and DHF potentials for H, Al, Ni, Ag, Au, and Cm in Sec. 6. Differential cross sections for these elements from the TFD[10] and DHF[12] potentials are presented and compared in Sec. 7 for electron energies of 100, 500, 1000, and 10 000 eV. Similar comparisons are also made of differential cross sections from the DHF potential[11,12] at energies of 1000 and 10 000 eV to examine the effects of different exchange corrections in the calculations. In addition, we compare calculated differential cross sections from the TFD and DHF potentials with measured cross sections for He, Ne, Ar, Kr, Xe, and Hg at selected energies between 50 and 3000 eV. The latter comparisons are made at energies for which there were two or more independent experimental sets of data available. We present comparisons of transport cross sections obtained from the TFD and DHF potentials in Sec. 8. In Sec. 9, we present comparisons of three quantities derived from differential cross sections that were obtained from the TFD and DHF potentials: elastic-backscattered intensities for an overlayer film on a surface; electron inelastic mean free paths determined by the elastic-peak electron spectroscopy method; and mean escape depths for signal electrons in AES and XPS. Finally, we comment in Sec. 10 on the validity of differential cross sections for neutral atoms in the simulations of electron transport in solids. Our conclusions are presented in Sec. 11.

2. Calculation of Differential Elastic-Scattering Cross Sections by the Partial-Wave Expansion Method

Elastic collisions of electrons with atoms can be described by means of the so-called ''static-field'' approximation, i.e., as scattering of the projectile by the electrostatic field of the target atom. It is assumed that the atomic electron density $\rho(r)$ as a function of radius, r, is spherically symmetric; for atoms with open electron shells, this implies an average over orientations. The potential energy of the projectile, $V(r)$, is then also spherical. Exchange between the projectile and the atomic electrons can be accounted for approximately by adding a local correction to the electrostatic interaction. In nonrelativistic (Schrödinger) theory, the wave function describing the scattering event is a distorted plane wave with the asymptotic form

$$\psi(\mathbf{r}) \underset{r\to\infty}{\rightarrow} \exp(i\mathbf{K}\cdot\mathbf{r}) + \frac{\exp(iKr)}{r} f(\theta), \qquad (1)$$

where $\mathbf{r}$ is the position vector, $\mathbf{p}=\hbar\mathbf{K}$ is the momentum of the projectile, and $\hbar$ is the reduced Planck's constant. The first term in Eq. (1) represents the incident parallel monoenergetic electron beam, and the second term describes electrons deflected by the interaction with the scattering center. The differential cross section (DCS) for the scattering is completely determined by the scattering amplitude $f(\theta)$.

In nonrelativistic theory, the distorted plane waves [Eq. (1)] are solutions of the time-independent Schrödinger equation with the potential $V(r)$. In the relativistic formulation adopted here, $\psi(\mathbf{r})$ is a solution of the time-independent Dirac equation with the same potential. To calculate the DCS, the distorted wave [Eq. (1)] is expressed as a superposition of spherical waves (i.e., eigenfunctions of the total angular momentum) that are computed numerically by solving the radial wave equation. In fact, only a series of so-called phase shifts, δ_l, is required to determine the scattering amplitude and the DCS.

In the relativistic (Dirac) theory, the elastic-scattering differential cross section is expressed as[46]

$$d\sigma_e/d\Omega = |f(\theta)|^2 + |g(\theta)|^2, \tag{2}$$

where $f(\theta)$ and $g(\theta)$ are the direct and spin-flip scattering amplitudes. These amplitudes are defined in terms of the phase shifts δ_l^+ and δ_l^- for spin-up and spin-down scattering, respectively

$$f(\theta) = \frac{1}{2iK}\sum_l \{(l+1)[\exp(2i\delta_l^+)-1] + l[\exp(2i\delta_l^-)-1]\}P_l(\cos\theta), \tag{3}$$

$$g(\theta) = \frac{1}{2iK}\sum_l [\exp(2i\delta_l^-)-\exp(2i\delta_l^+)]P_l^1(\cos\theta). \tag{4}$$

In Eqs. (3) and (4), $P_l(\theta)$ are Legendre polynomials, and $P_l^1(\theta)$ are the associated Legendre polynomials

$$P_l^1(z) = (1-z^2)^{1/2}\frac{dP_l(z)}{dz}.$$

In the nonrelativistic limit, i.e., for slow electrons, $f(\theta)$ reduces to the Schrödinger scattering amplitude and $g(\theta)$ vanishes. Equations (2)–(4) for central fields were first derived by Mott,[47] and the resulting DCS is sometimes referred to as the Mott cross section.

We provide information in the following two sections on calculations of the phase shifts for the TFD and DHF potentials. These phase shifts fully characterize the elastic-scattering event. Calogero[48] proposed a formalism that provides absolute values of the phase shifts. For the nonrelativistic case, he introduced the phase function $\delta_l(r)$ that approaches asymptotically the value of the phase shift at large distances from the nucleus

$$\delta_l = \lim_{r\to\infty}\delta_l(r),$$

and that is equal to zero at the nucleus. The relativistic phase function $\delta_l^{\pm}(r)$ behaves in a similar manner. The phase function is described by a first-order differential equation with the right-hand side expressed in terms of Riccati–Bessel functions. Integration of this differential equation, however, is very slowly convergent, and the method cannot be readily used for practical calculations.[49]

The reliability of the calculated DCSs is determined mainly by the accuracy of the adopted interaction potential. Atomic potentials derived from statistical models, mostly the Thomas–Fermi–Dirac model,[50,51] are well described by simple analytical expressions. Due to this fact, they have been frequently used in calculations of elastic-scattering cross sections. Relativistic self-consistent calculations provide a more accurate description of the atomic structure; the relevant algorithms, however, can be very involved. For the databases of Refs. 9 and 12, atomic electron densities calculated with the multiconfiguration Dirac–Hartree–Fock code of Desclaux[52] were used. This code provides advanced atomic-structure calculations that account for exchange and relativistic effects in a consistent way. The program is an implementation of the multiconfigurational model mentioned above. In fact, one should refer to it as the multiconfiguration Dirac–Fock model. We also note here that coupling between elastic and available inelastic channels has generally been ignored in DCS calculations. Such coupling could occur, for example, at energies near thresholds for inner-shell excitation and lead to negative-ion inner-shell resonances in the elastic channel. The calculated DCSs (e.g., in Refs. 10 and 12) may then have larger uncertainties at energies where such coupling can occur.

3. Phase Shifts Calculated from the Thomas–Fermi–Dirac Potential

3.1. Differential Equation

Lin *et al.*[53] and Bunyan and Schonfelder[54] developed an effective algorithm for calculations of relativistic differential elastic-scattering cross sections. Details of the corresponding calculations, with the TFD potential to describe the electron–atom interaction, were published by Jablonski[22] and by Jablonski and Tougaard.[55] Elastic-scattering cross sections derived from this algorithm have been successfully used in numerous studies of elastic interactions of electrons with solids;[22,27–33] cross sections obtained in a similar way have also been applied to problems of the same type.[13–21,23–26] Elastic-scattering cross sections derived from the TFD potential were made available in two versions of a NIST elastic-scattering cross-section database.[8,10] The main features in the calculations of phase shifts for determination of these cross sections are briefly described below.

The Dirac equation for an electron interacting with the atomic potential $V(r)$ can be reduced to a first-order differential equation[53,54]

TABLE 1. Main characteristics of published databases containing differential and/or total elastic-scattering cross sections

Authors	Ref.	Theoretical model	Potential	Energies (eV)	Elements
M. Fink and A. C. Yates	1	Relativistic PWEM	Relativistic Hartree–Fock–Slater[a]	100–1500	H, He, C, Ne, Ar, Kr, Rb, Xe, Cs, Au, Hg, Pb, Bi
M. Fink and J. Ingram	2	Relativistic PWEM	Relativistic Hartree–Fock–Slater[a]	100–1500	Be, N, O, Al, Cl, V, Co, Cu, As, Nb, Ag, Sn, Sb, I, Ta
D. Gregory and M. Fink	3	Relativistic PWEM	Relativistic Hartree–Fock–Slater[a] Nonrelativistic Hartree–Fock[b]	100–1500	Li, Na, Mg, P, K, Ca, Sc, Mn, Ga, Br, Sr, Mo, Rh, Cd, Ba, W, Os
M. E. Riley, C. J. MacCallum, and F. Biggs	4	Relativistic PWEM	Relativistic Harteree–Fock[c] Nonrelativistic Hartree–Fock[d]	1000–256 000	He, Be, C, N, O, F, Ne, Al, Si, Ar, Ti Fe, Ni, Cu, Kr, Mo, Ag, Sn, Xe, Ta, Au, Hg, Pb, U Fits made for 80 elements
L. Reimer and B. Lödding	5	Relativistic PWEM WKB method[j]	Hartree–Fock[f] Thomas–Fermi–Dirac[e]	1000–100 000	C, Al, Si, Ti, Fe, Cu, Ge, Mo, Ag, Sb, Au, Pb, U
Z. Czyzewski, D. O. MacCallum, A. Romig, and D. C. Joy	6	Relativistic PWEM	Thomas–Fermi–Dirac[e] Hartree–Fock[f] Relativistic Hartree–Fock[g]	20–20 000	All elements (from internet site)
M. J. Berger, S. M. Seltzer, R. Wang, R. Wang, and A. Schechter	7	Relativistic PWEM	Dirac–Hartree–Fock[h]	1000–1 000 000	All elements (using enclosed software). Tables for H, He, Be, C, N, O, Ne, Al, Si, Ar, Ti, Fe, Cu, Ge, Kr, Mo, Ag, Xe, Ta, W, Au, Pb, U
A. Jablonski and S. Tougaard	8	Nonrelativistic PWEM Relativistic PWEM	Thomas–Fermi–Dirac[e,i]	50–9999	All elements
R. Mayol and F. Salvat	9	Relativistic PWEM	Dirac–Hartree Fock[h]	100–100 000 000	All elements
A. Jablonski and C. J. Powell	10	Relativistic PWEM	Thomas–Fermi Dirac[e,i]	50–20 000	All elements
M. J. Berger and S. M. Seltzer	11	Relativistic PWEM WKB method[j]	Dirac–Hartree–Fock[h]	1000–100 000 000	All elements (using enclosed software)
A. Jablonski, F. Salvat, and C. J. Powell	12	Relativistic PWEM	Dirac–Hartree–Fock[h]	50–300 000	All elements

[a]D. Liberman, J. T. Waber, and D. T. Cromer, Phys. Rev. **137**, A27 (1965); R. D. Cowan, A. C. Larson, D. Liberman, J. B. Mann, and J. Waber, Phys. Rev. **144**, 5 (1966).
[b]E. Clementi, *Tables of Atomic Functions* (International Business Machines Corp., San Jose, CA., 1965).
[c]J. B. Mann and J. T. Waber, At. Data **5**, 201 (1973).
[d]J. B. Mann, At. Data Nucl. Data Tables **12**, 1 (1973).
[e]R. A. Bonham and T. G. Strand, J. Chem. Phys. **39**, 2200 (1963).
[f]H. L. Cox and R. A. Bonham, J. Chem. Phys. **47**, 2599 (1967).
[g]A. W. Ross and M. Fink, J. Chem. Phys. **85**, 6810 (1986).
[h]J. P. Desclaux, Comput. Phys. Commun. **9**, 31 (1975).
[i]L. H. Thomas, J. Chem. Phys. **22**, 1758 (1954); A. Jablonski, Physica A **183**, 361 (1992).
[j]Wentzel–Kramers–Brillouin.

TABLE 2. Theoretical models used for calculations of the atomic electron density or the atomic potential

Name(s) and abbreviation	Short description
Thomas–Fermi (TF)	Statistical model. The electron cloud is considered as a locally homogeneous electron gas confined by the screened field of the nucleus.
Thomas–Fermi–Dirac (TFD)	Modification of the TF model that includes the effect of electron exchange using the exchange energy density derived by Dirac.
Hartree (H)	The simplest self-consistent method. Nonrelativistic. The Hartree equations are obtained from the variational method with a trial function equal to the (nonantisymmetrized) product of orbitals.
Hartree–Fock (HF)	Nonrelativistic. The HF equations are obtained by applying the variational method with a trial function expressed as a single Slater determinant, i.e., as the antisymmetrized product of orbitals. The antisymmetry of the wave function accounts for electron exchange effects in a systematic way.
Hartree–Fock–Slater (HFS) or Hartree–Slater (HS)	Nonrelativistic. The exchange potential in the HF equations is replaced by the local approximation of the Slater (proportional to $\rho^{1/3}$, similar to the Dirac correction in the TFD model). The resulting equations are much simpler to solve than the H and HF equations.
Dirac–Hartree–Fock (DHF) or Dirac–Fock (DF)	Relativistic version of the HF method. Includes exchange in the natural way, i.e., the wave function is a Slater determinant with orbitals that are solutions of the Dirac equation with a nonlocal exchange operator.
Dirac–Hartree–Fock–Slater (DHFS) or Dirac–Fock–Slater (DFS)	Relativistic version of the HFS or HS method; usually the nonrelativistic local exchange potential of Slater is adopted

$$\frac{d\Phi_l^{\pm}(r)}{dr}=\frac{k^{\pm}}{r}\sin[2\Phi_l^{\pm}(r)]+[W-V(r)]\cos[2\Phi_l^{\pm}(r)],\quad l=0,1,2,\ldots, \tag{5}$$

where W is the total energy of the electron, and the coefficients $k^{\pm}$ are defined as follows

$$k^{+}=-(l+1)\quad\text{for the ''spin-up'' case,}\quad j=l+\tfrac{1}{2},$$

$$k^{-}=l\quad\text{for the ''spin-down'' case,}\quad j=l-\tfrac{1}{2}.$$

The system of units is such that energy is expressed in units of mc^2 and length r is expressed in units of $\hbar/(mc)$, where m is the electron mass and c is the velocity of light in vacuum. For each quantum number l, there are two solutions, $\Phi^{+}(r)$ and $\Phi^{-}(r)$, which are related to the lth order spin-up and spin-down phase shifts, $\delta_l^{\pm}$

$$\delta_l^{\pm}=\tan^{-1}\frac{Kj_{l+1}(Kr)-j_l(Kr)[(W+1)\tan\Phi_l^{\pm}+(1+l+k^{\pm})/r]}{Kn_{l+1}(Kr)-n_l(Kr)[(W+1)\tan\Phi_l^{\pm}+(1+l+k^{\pm})/r]}, \tag{6}$$

where $K^2=W^2-1$, $j_l(x)$ and $n_l(x)$ are spherical Bessel functions, and $\Phi_l^{\pm}$ is the asymptotic value of the solution $\Phi_l^{\pm}(r)$

$$\Phi_l^{\pm}=\lim_{r\to\infty}\Phi_l^{\pm}(r).$$

The expression on the right-hand side of Eq. (6) is calculated for values of r for which $V(r)=0$.[53] The Thomas–Fermi–Dirac potential has a finite maximum radius r_0, and Eq. (6) is evaluated for this radius (see Sec. 3.4). The Sarafyan–Butcher embedding formula[56] was found to be very effective for integrating Eq. (5).

3.2. Interaction Potential

The interaction potential, $V(r)$, was approximated by the Thomas–Fermi–Dirac potential. The simple analytical fit of Bonham and Strand[57] was used in the calculations

$$V(r) = -\frac{Ze^2}{r}\Psi(r), \tag{7}$$

where e is the electronic charge and

$$\Psi(r) = \sum_{i=1}^{3} p_i \exp(-q_i r) \tag{8}$$

is the screening function, i.e., the function that takes into account the screening by the atomic electrons. In Eq. (8), p_i and q_i are fitted parameters that depend on the atomic number. Jablonski[58] has shown that this expression well describes the TFD potential for all elements except hydrogen. For this element, the fitted parameters p_i and q_i published by Jablonski[58] are recommended.

3.3. Initial Condition for Integration

The initial value of the solution $\Phi_l^{\pm}(r)$ for small r has been calculated from the series expansion

$$\Phi_l^{\pm}(r) = \Phi_0 + \Phi_1 r + \Phi_2 r^2 + \Phi_3 r^3 + \cdots .$$

The coefficients Φ_0, Φ_1, Φ_2, and Φ_3 were derived by Bunyan and Schonfelder[54]

$$\sin(2\Phi_0) = -Z_0/k^{\pm},$$

$$\Phi_1 = \frac{W + Z_1 - \cos(2\Phi_0)}{1 - 2k^{\pm}\cos(2\Phi_0)},$$

$$\Phi_2 = \frac{2\Phi_1 \sin(2\Phi_0)(1 - k^{\pm}\Phi_1) + Z_2}{2 - 2k^{\pm}\cos(2\Phi_0)},$$

$$\Phi_3 = \frac{2\Phi_2 \sin(2\Phi_0)(1 - 2k^{\pm}\Phi_1) + 2\Phi_1^2 \cos(2\Phi_0)(1 - \frac{3}{2}k^{\pm}\Phi_1) + Z_3}{3 - 2k^{\pm}\cos(2\Phi_0)},$$

where the parameters Z_0, Z_1, Z_2, and Z_3 are the coefficients of the series expansion of the potential $V(r)$ for small values of r

$$V(r) = -\frac{1}{r}(Z_0 + Z_1 r + Z_2 r^2 + Z_3 r^3 + \cdots).$$

3.4. Upper Limit of Integration

The TFD potential has a finite maximum radius, r_0. For this reason, the integration of Eq. (5) was performed up to the radius $r = r_0$. Values of r_0 were taken from compilations published by Thomas[59] and Jablonski.[58]

The r_0 values are independent of electron energy. For selected elements, these values (in units of the Bohr radius, a_0) are as follows[58,60]

$$\text{for } Z = 1 \quad r_0 = 2.975,$$
$$\text{for } Z = 13 \quad r_0 = 4.156,$$
$$\text{for } Z = 28 \quad r_0 = 4.442,$$
$$\text{for } Z = 47 \quad r_0 = 4.614,$$
$$\text{for } Z = 79 \quad r_0 = 4.771,$$
$$\text{for } Z = 96 \quad r_0 = 4.826.$$

3.5. Phase Shifts

A considerable number of phase shifts $\delta_l^{\pm}$ was found to be necessary to reach sufficient accuracy of the differential elastic-scattering cross section calculated from Eqs. (2)–(4). For energies up to 10 keV, the partial-wave series was summed with an accuracy of eight decimal places. At 10 keV, the following numbers of phase shifts were necessary to reach this accuracy

$$\text{for } Z = 1 \quad 0 \leqslant l \leqslant 95,$$
$$\text{for } Z = 13 \quad 0 \leqslant l \leqslant 126,$$
$$\text{for } Z = 28 \quad 0 \leqslant l \leqslant 133,$$
$$\text{for } Z = 47 \quad 0 \leqslant l \leqslant 137,$$
$$\text{for } Z = 79 \quad 0 \leqslant l \leqslant 141,$$
$$\text{for } Z = 96 \quad 0 \leqslant l \leqslant 142.$$

In the energy range $10\ \text{keV} < E \leqslant 20\ \text{keV}$, the summation was performed with an accuracy of six decimal places. At 20 keV, the number of needed phase shifts was distinctly larger than for 10 keV

$$\text{for } Z = 1 \quad 0 \leqslant l \leqslant 131,$$
$$\text{for } Z = 13 \quad 0 \leqslant l \leqslant 175,$$
$$\text{for } Z = 28 \quad 0 \leqslant l \leqslant 183,$$
$$\text{for } Z = 47 \quad 0 \leqslant l \leqslant 191,$$
$$\text{for } Z = 79 \quad 0 \leqslant l \leqslant 196,$$
$$\text{for } Z = 96 \quad 0 \leqslant l \leqslant 199.$$

3.6. Special Functions

The algorithm used for calculating the elastic-scattering cross sections requires routines to provide the special functions $j_l(x)$, $n_l(x)$, $P_l(x)$, and $P_l^1(x)$ [Eqs. (3), (4), and (6)]. Care was taken to ensure that these functions were calculated with an accuracy of ten decimal places for $0 \leqslant l \leqslant 200$. Details of the analysis and the resulting algorithm for calculating the function $j_l(x)$ have been published separately.[60] A similar analysis was made for the remaining special functions (see Jablonski and Tougaard[9]).

4. Phase Shifts Calculated from the Dirac–Hartree–Fock Potential

The calculation of phase shifts (and thus the elastic-scattering DCSs) from the Dirac–Hartree–Fock potential essentially follows the scheme described by Salvat and Mayol.[61]

4.1. Differential Equation

The phase shifts $\delta_l^{\pm}$ are obtained from the large r behavior of the radial wave functions, $P_l^{\pm}(r)$ and $Q_l^{\pm}(r)$, which are calculated by integrating the radial Dirac equations

$$\frac{dP_l^{\pm}}{dr} = -\frac{k^{\pm}}{r} P_l^{\pm}(r) + \frac{E - V + 2mc^2}{c\hbar} Q_l^{\pm}(r), \quad (9a)$$

$$\frac{dQ_l^{\pm}}{dr} = -\frac{E - V}{c\hbar} P_l^{\pm}(r) + \frac{k^{\pm}}{r} Q_l^{\pm}(r), \quad (9b)$$

where E is the kinetic energy of the projectile that is related to its total energy W by $E = W - mc^2$. The solution algorithm implements Bühring's power series method[62] and is based on a cubic-spline interpolation of the potential function $rV(r)$ that is tabulated on a dense grid of r values

$$r_1 = 0 < r_2 \cdots < r_{N-1} < r_N. \quad (10)$$

That is, between each pair of consecutive grid points, r_n and r_{n+1}, the potential function, $rV(r)$, is represented as a piecewise cubic polynomial in r

$$rV(r) = a_n + b_n r + c_n r^2 + d_n r^3. \quad (11)$$

Then, in the interval (r_n, r_{n+1}), the radial functions can be formally expressed by the power series

$$P_l^{\pm}(r) = r^{\alpha} \sum_{i=0}^{\infty} p_i r^i$$

and

$$Q_l^{\pm}(r) = r^{\beta} \sum_{i=0}^{\infty} q_i r^i, \quad (12)$$

with coefficients determined by the values of $P_l^{\pm}(r_n)$ and $Q_l^{\pm}(r_n)$ at the end point of the interval (see Salvat and Mayol[63]). As these series expansions can be summed up to the required accuracy (nine significant digits in the corresponding PWEM code), truncation errors are practically avoided.

4.2. Interaction Potential

The interaction potential is defined as

$$V(r) = -e\varphi(r) + V_{\text{exc}}(r), \quad (13)$$

where $\varphi(r)$ is the electrostatic potential of the target atom

$$\varphi(r) = \frac{Ze}{r} - e\left(\frac{1}{r} \int_0^r \rho(r') 4\pi r'^2 dr' + \int_r^{\infty} \rho(r') 4\pi r' dr' \right), \quad (14)$$

and where $\rho(r)$ is the atomic electron density which was calculated using the self-consistent DHF code of Desclaux.[52]

The term $V_{\text{exc}}(r)$ in Eq. (13) is a local approximation to the exchange interaction between the projectile and the electrons in the target; it should not be confused with the exchange interaction considered in the TFD model and in self-consistent calculations that accounts for exchange between atomic electrons. We use the exchange potential of Furness and McCarthy[64]

$$V_{\text{exc}}(r) = \frac{1}{2}[E + e\varphi(r)] - \frac{1}{2}\left\{ [E + e\varphi(r)]^2 + 4\pi \frac{\hbar^2 e^2}{m} \rho(r) \right\}^{1/2}. \quad (15)$$

The interaction potential [Eq. (13)] is thus completely determined by the atomic density $\rho(r)$.

4.3. Initial Condition for Integration

The integration of the radial equations is started from $r = 0$, with boundary values

$$P_l^{\pm}(0) = 0,$$

and

$$Q_l^{\pm}(0) = 0. \quad (16)$$

In the first r interval from $r_1 = 0$ to r_2 [Eq. (10)], the constants α and β are different from zero and are determined by the angular-momentum quantum numbers (see Salvat and Mayol[63]). For the outer intervals $(r > r_2)$, $\alpha = \beta = 0$.

4.4. Upper Limit of Integration

After determining the values of the radial functions at r_2, the solution is extended outwards by using the series expansions Eq. (12) (with $\alpha = \beta = 0$) up to a certain radial distance, $r_{\max}$, large enough to ensure that the potential energy of the electron $V(r)$ is negligible as compared to its kinetic energy E. For selected elements and at an energy of 10 keV, the maximum ranges were the following (in a_0 units)

for $Z=1$ $r_{max}=12.27$,

for $Z=13$ $r_{max}=20.15$,

for $Z=28$ $r_{max}=17.85$,

for $Z=47$ $r_{max}=19.37$,

for $Z=79$ $r_{max}=17.11$,

for $Z=96$ $r_{max}=21.54$.

At 20 keV

for $Z=1$ $r_{max}=11.96$,

for $Z=13$ $r_{max}=19.75$,

for $Z=28$ $r_{max}=17.48$,

for $Z=47$ $r_{max}=18.80$,

for $Z=79$ $r_{max}=16.74$,

for $Z=96$ $r_{max}=21.13$.

We see that these ranges are considerably larger than the maximum radius, r_0, of the TFD potential in Sec. 3.4.

4.5. Phase Shifts

At sufficiently large distances r, the radial function $P_l^{\pm}(r)$ adopts the asymptotic form

$$P_l^{\pm}(r) \cong \sin\left(Kr - l\frac{\pi}{2} + \delta_l^{\pm}\right), \tag{17}$$

where

$$\hbar K = \frac{1}{c}\sqrt{E(E+2mc^2)} \tag{18}$$

is the momentum of the projectile. Equation (17), which confers a geometrical meaning to the phase shift, is not directly usable to compute $\delta_l^{\pm}$ because $P_l^{\pm}(r)$ reaches the form given by Eq. (17) only at distances r that may be much larger than r_{max}. Instead, the phase shift is obtained from the calculated values of the radial functions at r_{max} by matching the numerical solution to the exact solution for $r>r_{max}$ $(V=0)$ that can be expressed as a linear combination of spherical Bessel functions $j_k(Kr)$ and $n_k(Kr)$ with indices $k=l$, $l\pm1$.[59]

The DHF potential requires a considerably larger number of phase shifts than the TFD potential. At 10 keV, we have

for $Z=1$ $0\leqslant l\leqslant 221$,

for $Z=13$ $0\leqslant l\leqslant 386$,

for $Z=28$ $0\leqslant l\leqslant 343$,

for $Z=47$ $0\leqslant l\leqslant 369$,

for $Z=79$ $0\leqslant l\leqslant 325$,

for $Z=96$ $0\leqslant l\leqslant 422$.

At 20 keV

for $Z=1$ $0\leqslant l\leqslant 307$,

for $Z=13$ $0\leqslant l\leqslant 538$,

for $Z=28$ $0\leqslant l\leqslant 478$,

for $Z=47$ $0\leqslant l\leqslant 514$,

for $Z=79$ $0\leqslant l\leqslant 452$,

for $Z=96$ $0\leqslant l\leqslant 589$.

4.6. Special Functions

The only special functions used in calculations of the DCSs for the DHF potential are the spherical Bessel functions $j_l(x)$ and $n_l(x)$. The algorithm used to compute these functions combines several analytical expressions and recurrence relations, and yields results that are accurate to 13 or more significant digits for ranges of l and x values used in the present calculations.[65]

5. Transport Cross Section

Values of the transport cross section are needed in the analytical formalism describing signal-electron transport in AES and XPS.[66,67] Determination of numerous parameters related to this application (e.g., depth distribution function for the signal electrons,[68–70] effective attenuation length,[70–72] signal-electron mean escape depth,[31] information depth,[73] etc.) requires knowledge of the transport cross section values.

The transport cross section (TCS) is defined as the quotient of the fractional momentum loss of a particle incident on the sample arising from elastic scattering by the areic density of the sample atoms, for an infinitesimally thin sample.[74] This cross section is expressed as an area per atom. In other words, the transport cross section describes the mean fractional momentum loss with respect to initial direction due to the elastic scattering alone. Let us denote by $\mathbf{k}$ the electron momentum before elastic scattering, and by $\mathbf{k}'$ the projection on the initial direction of the momentum after elastic scattering. Obviously, $\mathbf{k}'=\mathbf{k}\cos\theta$. Let us further denote the fractional momentum loss, due to elastic scattering alone, by

$$\Delta k = \frac{|\mathbf{k}-\mathbf{k}'|}{|\mathbf{k}|}.$$

We may consider the transport cross section, σ_{tr}, as the product of the total elastic-scattering cross section, σ_{el}, and the mean fractional momentum loss, $\langle\Delta k\rangle$

$$\sigma_{tr}=\sigma_{el}\langle\Delta k\rangle=\sigma_{el}\frac{\int_{4\pi}\Delta k(d\sigma/d\Omega)d\Omega}{\int_{4\pi}(d\sigma/d\Omega)d\Omega}. \tag{19}$$

Equation (19) can be transformed to

$$\sigma_{tr}=2\pi\int_0^{\pi}(1-\cos\theta)(d\sigma/d\Omega)\sin\theta\, d\theta. \tag{20}$$

As indicated frequently in the literature,[6,22,33,58] a change of the atomic potential (e.g., from the TFD potential to the DHF potential) can produce a pronounced variations of the differential cross section in the range of small scattering angles. Differences in the remaining angular range, with the exception of deep minima in the DCS, are rather small. However, the value of the DCS in the region of minima is small, and thus the DCS in this region does not appreciably influence the TCS. In the integrand of Eq. (20), we have two functions approaching zero in the region of small scattering angles: $\sin\theta$ and $(1-\cos\theta)$. Consequently, we may expect that the sensitivity of the transport cross section to the interaction potential will be much weaker than the sensitivity of the total elastic-scattering cross section. It has been shown in a recent work that, indeed, values of the transport cross section depend only weakly on the potential for different elements and for a wide range of electron energies.[33]

6. Comparison of TFD and DHF Potentials

Figures 1(a)–1(f) show the TFD screening function calculated from Eq. (8) and the electrostatic part of the DHF interaction potential, $r\varphi(r)/Ze$, calculated from Eq. (14) for H, Al, Ni, Ag, Au, and Cm. The TFD potential is plotted out to the atomic radius r_0 (Sec. 2.4). The DHF potential is shown only out to a distance of 6 Bohr radii (6 a.u.) which is slightly larger than the radii r_0 for the considered elements.

We see that both potentials agree well for small radii, up to 1 a.u., where the screening function has its largest values. At larger distances, there is a growing difference between the two potentials. There seems to be no systematic relationship between the potentials. There are different ranges of radii where the TFD potential is larger than the DHF potential, while in other ranges the DHF potential is larger than the TFD potential. The lack of clear trends in the differences between the TFD and DHF potentials can be partially understood by recalling that the TFD electron density varies monotonically with the atomic number *Z*, whereas the DHF density is affected by ''shell'' effects, i.e., the contribution from each shell has a characteristic shape with maxima and minima. As a result, the shape of the atomic electron density varies from one element to the next.

7. Comparisons of Differential Elastic-Scattering Cross Sections

We present a series of comparisons of differential elastic-scattering cross sections calculated from the TFD and DHF potentials and of these computed cross sections with measured cross sections. First, we make a systematic comparison of DCSs calculated from the TFD and DHF potentials for six elements (H, Al, Ni, Ag, Au, and Cm) at four representative electron energies (100, 500, 1000, and 10 000 eV). These cross sections were obtained from Version 2.0[10] and Version 3.0,[12] respectively, of the NIST Electron Elastic-Scattering Cross-Section Database. Second, we comment on the DCS values from the two potentials for H. Third, we compare DCSs from two NIST databases[11,12] for which the same DHF potential was used in the calculations but where different numerical procedures were employed. These comparisons were made for the same six elements at two electron energies (1000 and 10 000 eV). Finally, we compare DCSs calculated from the TFD and DHF potentials with measured DCSs for seven elements (He, Ne, Ar, Kr, Xe, Au, and Hg).

7.1. Comparisons of Differential Cross Sections Obtained from the TFD and DHF Potentials

A change of the potential leads to variations in the shape of the calculated differential cross sections (DCSs).[6,8,22,33,58] However, comparisons of DCSs have been made only for selected cases. For example, Jablonski and Powell[33] showed that the largest differences between DCSs resulting from the Dirac–Hartree–Fock–Slater and TFD potentials occur in the range of small scattering angles; this comparison, however, was limited to a single energy of 1000 eV. We intend here to systematically analyze the differences between DCSs for a wide range of atomic numbers and for a wide range of energies. Let us consider now the cross sections resulting from the two described algorithms.

Figures 2–7 show the differential cross sections, as functions of scattering angle, calculated for the six considered elements at electron energies, *E*, of 100, 500, 1000, and 10 000 eV using the TFD and DHF potentials. Qualitatively, the cross sections from the two potentials have similar shapes and have similar magnitudes. At low energies, the DCSs exhibit one or more minima (with the exception of hydrogen). The energy range over which the minima are present depends on the atomic number ($E<690$ eV for Al, $E<2600$ eV for Ni, $E<6600$ eV for Ag, $E<24\,000$ eV for Au, and $E<48\,000$ eV for Cm). Both potentials lead to the same number of minima (for a given element and energy), and their positions depend only slightly on potential. However, there are pronounced differences in the differential cross sections for the two potentials that can be summarized as follows:

(1) In most cases (Al, Ag, Au, and Cm), pronounced deviations are visible in the range of small scattering angles. This result is consistent with observation of Jablonski and Powell[33] at 1000 eV.
(2) Considerable differences between DCS values are noticeable in the vicinity of deep minima. Such differences may exceed more than 1 order of magnitude [see the DCS values for Ni at 100 eV in Fig. 4(a)].
(3) We see slight oscillations in the DCSs calculated for hydrogen using the TFD potential. These oscillations are not visible in the DCSs calculated from the DHF potential.
(4) The deviations between the cross sections tend to decrease with increase of electron energy. This result has also been reported by Jablonski.[22]

A useful measure of the difference between cross sections for the two potentials is the relative percentage deviation. Let us define this deviation, ΔDCS, by

$$\Delta\mathrm{DCS}=100(\mathrm{DCS}_{\mathrm{rel}}^{\mathrm{TFD}}-\mathrm{DCS}_{\mathrm{rel}}^{\mathrm{DHF}})/\mathrm{DCS}_{\mathrm{rel}}^{\mathrm{DHF}}, \quad (21)$$

where $\mathrm{DCS}_{\mathrm{rel}}^{\mathrm{TFD}}$ and $\mathrm{DCS}_{\mathrm{rel}}^{\mathrm{DHF}}$ denote the relativistic differential elastic-scattering cross sections calculated from the TFD and DHF potentials, respectively. The relative deviations ΔDCS for H, Al, Ni, Ag, Au, and Cm at 100, 500, 1000, and 10 000 eV are shown in Figs. 8–13. We see that the deviations in the region of small scattering angles may reach even 70% (e.g., Al or Cm at 100 eV). These deviations are associated with the ''tail'' of the scattering potential for large radii. For example, the DHF potential for Al is larger than the TFD potential for radii greater than about 1 Bohr radius [cf. Fig. 1(b)], and consequently the DCS calculated from the DHF potential is larger than the DCS from the TFD potential for small scattering angles (see Figs. 3 and 9). The largest percentage deviations, however, occur in the region of deep minima in the DCSs (Figs. 3–7), where the deviations may reach even 400%. For other scattering angles, the deviations depend on energy, and usually do not exceed 20%. For a given atom, the deviations decrease with increasing electron energy due to the increasing number of partial waves contributing to the DCS. As each partial wave corresponds roughly to a particular impact parameter, the whole volume of the atom is explored in great detail at the higher energies by the projectile wave function. As a result, the projectile experiences an average potential that is nearly the same for the DHF and TFD potentials. For H, the oscillations in the TFD DCSs are amplified when plotting the deviations ΔDCS. As one can see in Fig. 8, the number of oscillations depends on energy, reaching 26 at 10 keV.

DCSs from the TFD and DHF potentials for additional elements are presented in Sec. 7.4 where comparisons are made with measured DCSs.

7.2. Differential Cross Sections for Hydrogen

Let us compare the phase shifts δ_l^+ calculated for hydrogen from the TFD and DHF potentials. The results are shown in Fig. 14. At all considered energies, the phase shifts agree reasonably well up to a certain value of the angular momentum quantum number $l=l_0$. For larger l values, values of δ_l^+ calculated for the TFD potential decrease sharply while the phase shifts for the DHF potential decrease exponentially over a wide range of l. The oscillations in the DCS potential arise from the fact that there is not a sufficient number of Legendre functions in the series expressed by Eqs. (3) and (4).

The most conspicuous difference between the TFD and the DHF potentials is that the former drops to zero at $r=r_0$, whereas the DHF potential approaches zero asymptotically (i.e., for $r\to\infty$, cf. Fig. 1). The finite range of the TFD potential has a direct influence on the phase shifts. On classical grounds, we expect the phase shifts for the TFD potential to vanish for $l>l_0$, where $l_0\hbar$ is the angular momentum of the projectile corresponding to the impact parameter r_0, i.e.,

$$l_0=\frac{pr_0}{\hbar}\cong\sqrt{\frac{2E}{27.21}}\frac{r_0}{a_0}, \quad (22)$$

where $p=\hbar K$ is the momentum of the projectile, and the kinetic energy E is expressed in units of eV. This situation is illustrated in Fig. 14 which displays phase shifts for scattering by hydrogen atoms obtained from the TFD ($r_0=2.97\,a_0$) and DHF potentials. The TFD phase shifts are seen to fall rapidly for l values of about l_0, as predicted by the classical picture. As the partial-wave series for the TFD potential effectively converges with about l_0 terms, the difference between the TFD and DHF DCSs has an oscillatory structure (see Figs. 2 and 8), and the number of oscillations increases with E.

7.3. Comparisons of Differential Cross Sections Obtained from Different Evaluations with the DHF Potential

As shown in Secs. 7.1 and 7.2, differences between DCSs (for the same element and energy) can be mainly ascribed to two sources:

(1) differences between atomic potentials used in the calculations, and
(2) differences in the maximum radius of the potential utilized in the calculations.

We expect, however, that other factors could contribute to the observed differences. One possible factor could be differences among algorithms used for calculating the phase shifts, in particular, differences in numerical procedures used for integrating the differential equation. The resulting DCS differences can to a large extent be controlled, e.g., by varying the integration step. In the present analysis, the algorithm described in Sec. 4 was used in calculations of the phase shifts for the TFD potential. The results obtained were in agreement to within 3–4 decimal places with results from the algorithm described in Sec. 3. Thus, we expect that such errors are not significant here. A second factor for differences in DCSs could be associated with different approximations used for the exchange interaction, which in the calculations with the DHF potential is accounted for by the local approximation [Eq. (15)] and is neglected in the DCS calculations using the TFD potential [Eq. (7)]. A final factor could be related to the interpolation procedure that is needed in the program running the database, i.e., to provide DCS values at finer intervals of electron energy and scattering angle than those used for the main DCS calculations. Considerable deviations (particularly relative deviations) could occur in the regions of deep minima in the DCSs as a result of limitations of the interpolation procedure.

To examine changes in DCSs that arise from reasons other than the potentials, we decided to compare DCSs provided by two NIST databases listed in Table 1:

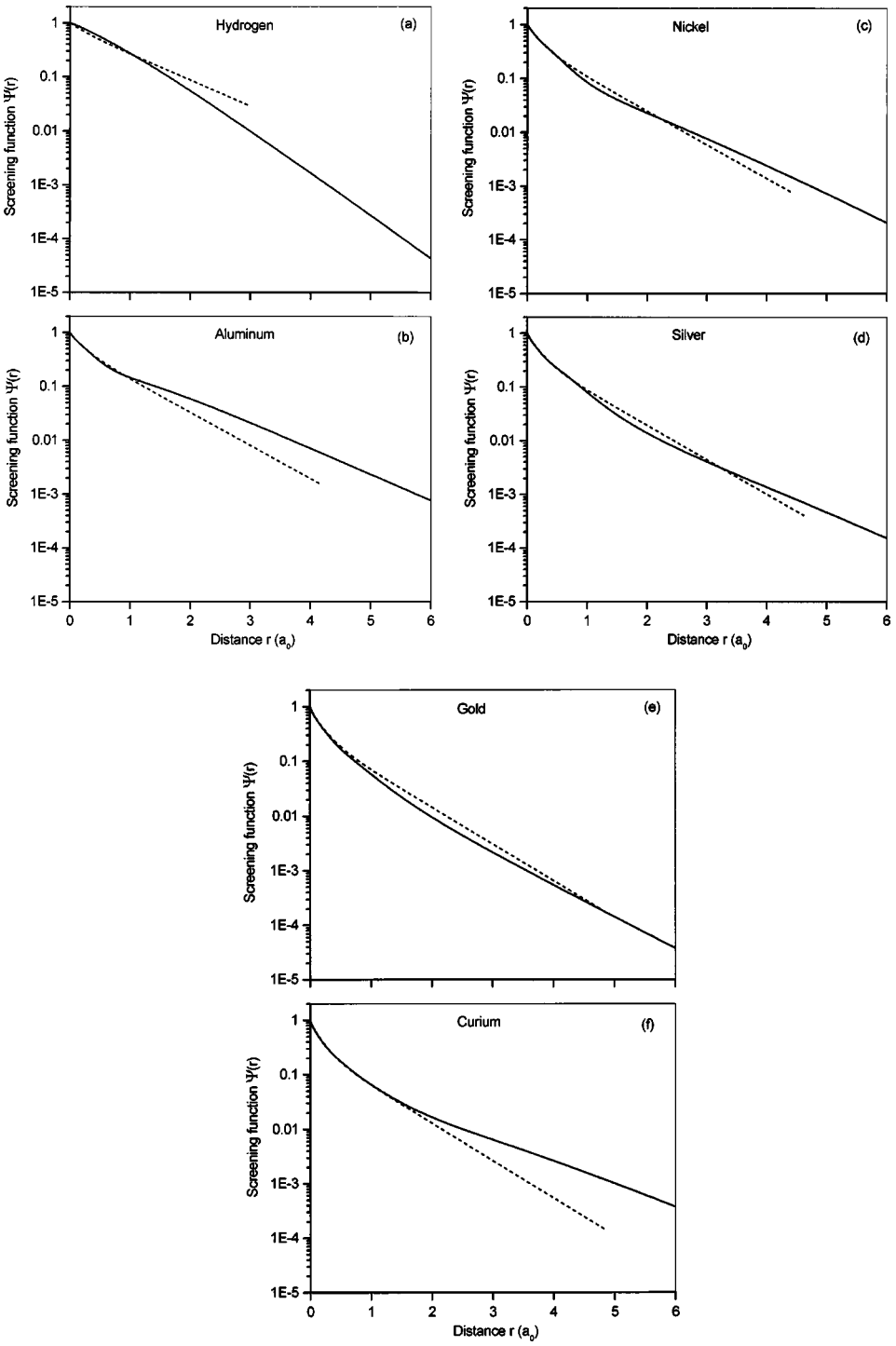

FIG. 1. Comparison of screening functions corresponding to the potentials used in calculations of the differential elastic-scattering cross sections as a function of radial distance (in units of the Bohr radius, a_0): (solid line) the DHF potential; (dashed line) the TFD potential: (a) hydrogen; (b) aluminum; (c) nickel; (d) silver; (e) gold; and (f) curium. Note the finite range of the TFD potential.

(1) the Berger and Seltzer database,[11] and
(2) the Jablonski, Salvat and Powell database.[12]

The DCSs in each database were calculated using the same DHF potential (for each atom). Different numerical methods, however, were used for calculating the DCSs. In addition, the exchange corrections adopted in the two databases are different. Berger and Seltzer[11] used a high-energy approximation from Riley and Truhlar[75] [Eq. (9a) in Ref. 11], whereas Jablonski *et al.*[12] used the exchange correction of Furness and McCarthy[64] [Eq. (15)]. As shown by Riley and Truhlar,[75] their high-energy approximation is the lowest-order term in the expansion of the Furness–McCarthy local-exchange potential in powers of the inverse kinetic energy of the projectile. Therefore, at low energies, the Furness–McCarthy potential is expected to yield more accurate phase shifts and DCSs.

Since the lowest energy in the Berger and Seltzer database is 1 keV, our DCS comparisons were made for two energies:

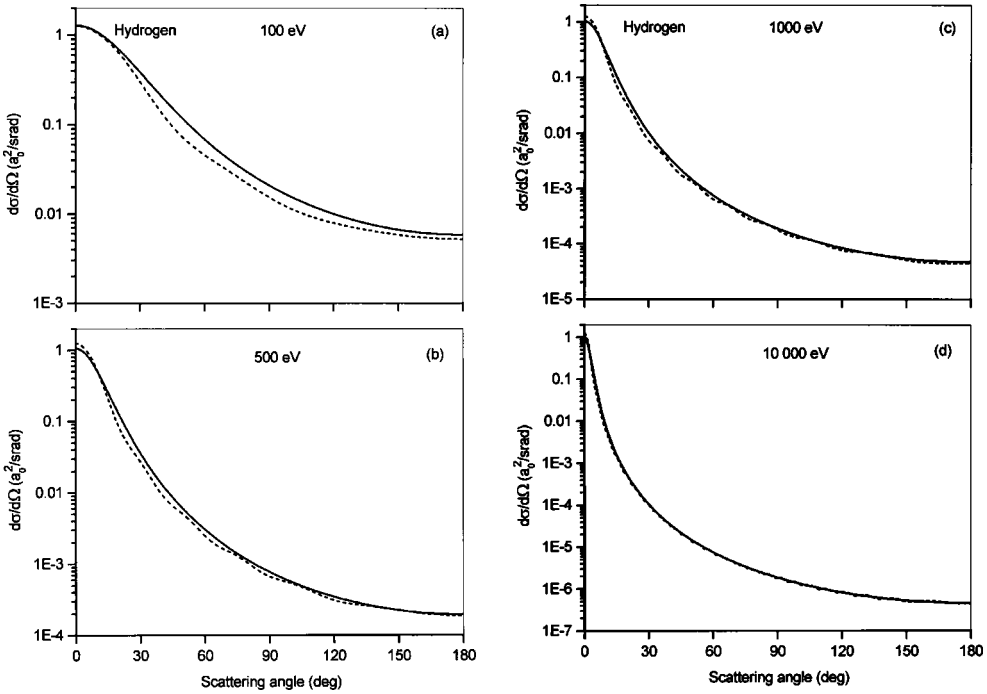

FIG. 2. Differential elastic-scattering cross sections, $d\sigma/d\Omega$, calculated for hydrogen for two potentials as a function of scattering angle: (solid line) DHF potential; (dashed line) TFD potential: (a) energy of 100 eV; (b) energy of 500 eV; (c) energy of 1000 eV; and (d) energy of 10 000 eV.

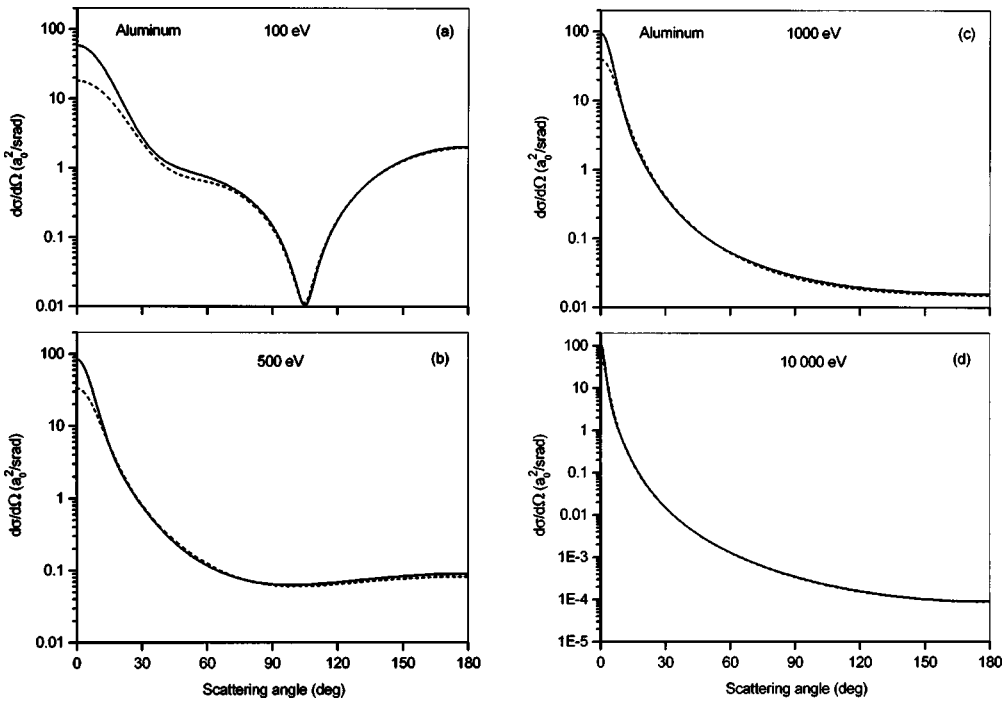

FIG. 3. Differential elastic-scattering cross sections, $d\sigma/d\Omega$, calculated for aluminum for two potentials as a function of scattering angle: (solid line) DHF potential; (dashed line) TFD potential: (a) energy of 100 eV; (b) energy of 500 eV; (c) energy of 1000 eV; and (d) energy of 10 000 eV.

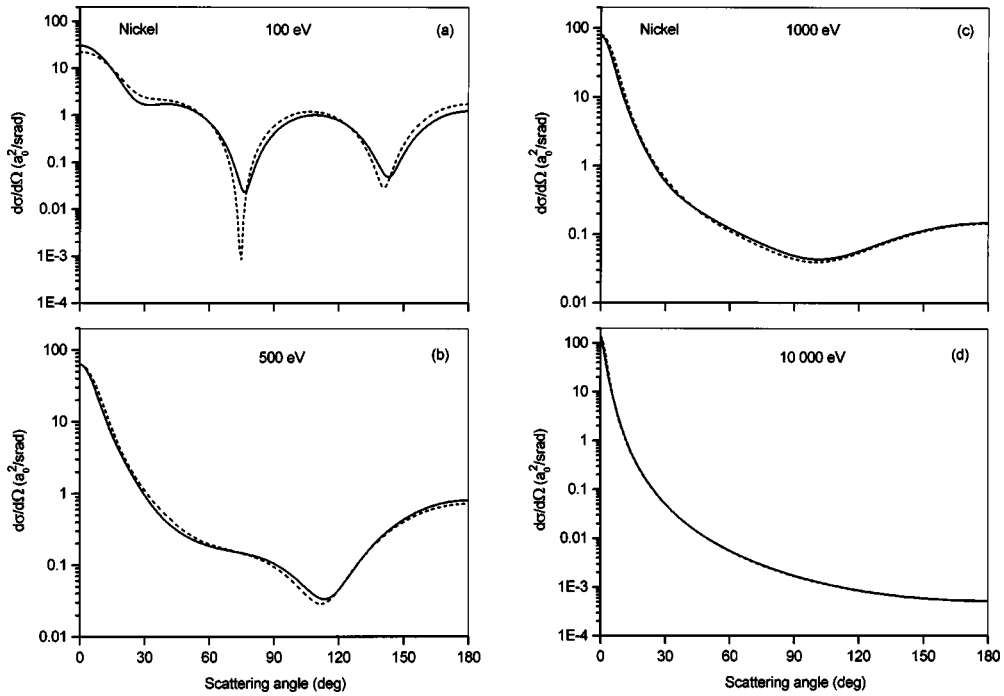

FIG. 4. Differential elastic-scattering cross sections, $d\sigma/d\Omega$, calculated for nickel for two potentials as a function of scattering angle: (solid line) DHF potential; (dashed line) TFD potential: (a) energy of 100 eV; (b) energy of 500 eV; (c) energy of 1000 eV; and (d) energy of 10 000 eV.

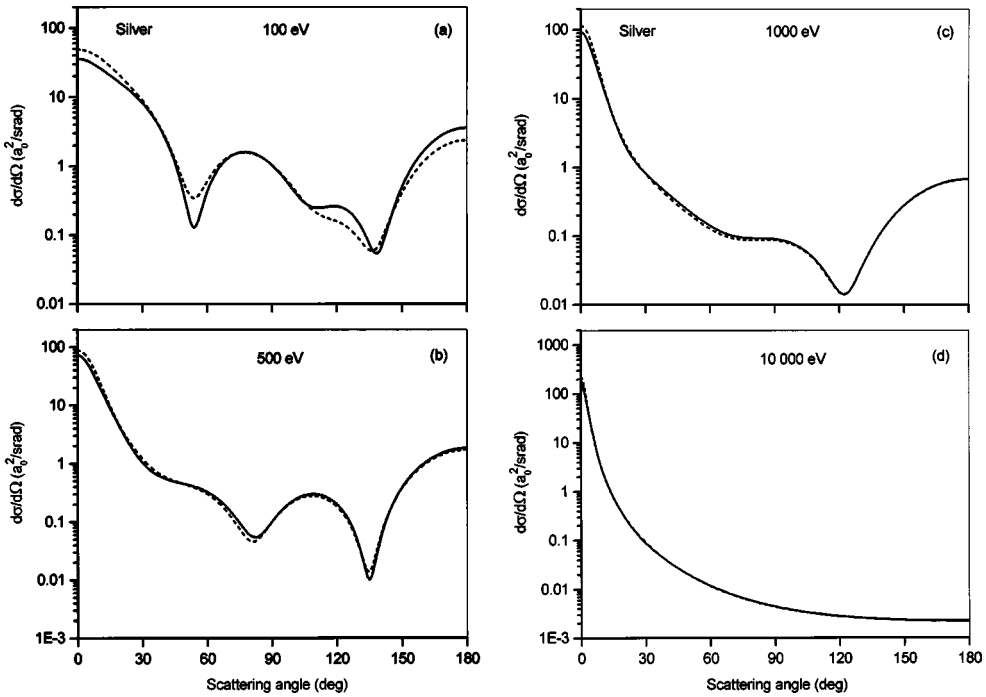

FIG. 5. Differential elastic-scattering cross sections, $d\sigma/d\Omega$, calculated for silver for two potentials as a function of scattering angle: (solid line) DHF potential; (dashed line) TFD potential: (a) energy of 100 eV; (b) energy of 500 eV; (c) energy of 1000 eV; and (d) energy of 10 000 eV.

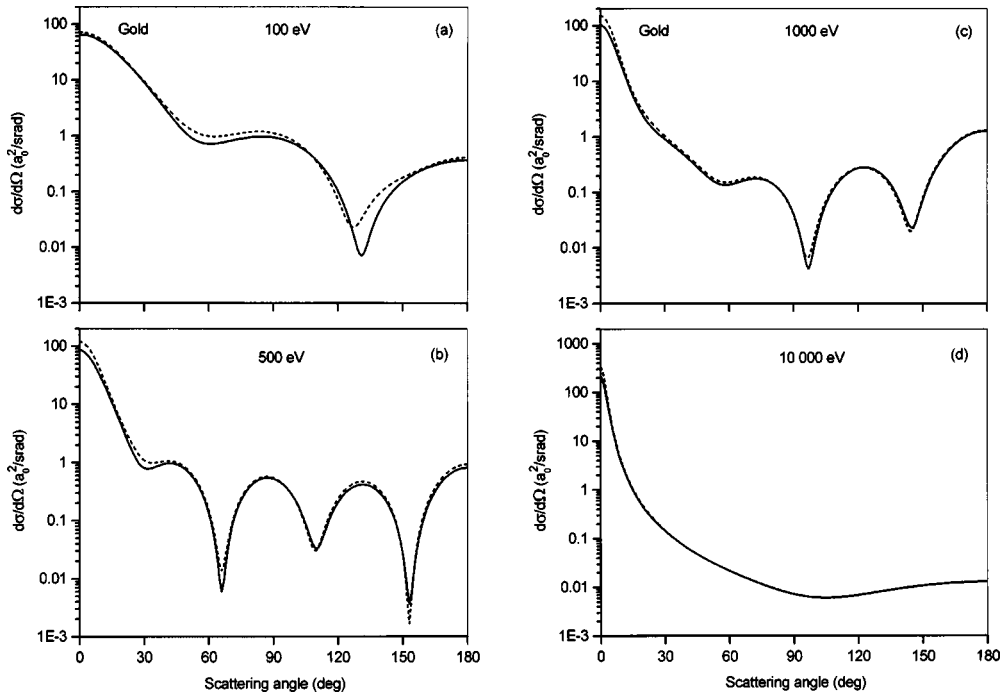

FIG. 6. Differential elastic-scattering cross sections, $d\sigma/d\Omega$, calculated for gold for two potentials as a function of scattering angle: (solid line) DHF potential; (dashed line) TFD potential: (a) energy of 100 eV; (b) energy of 500 eV; (c) energy of 1000 eV; and (d) energy of 10 000 eV.

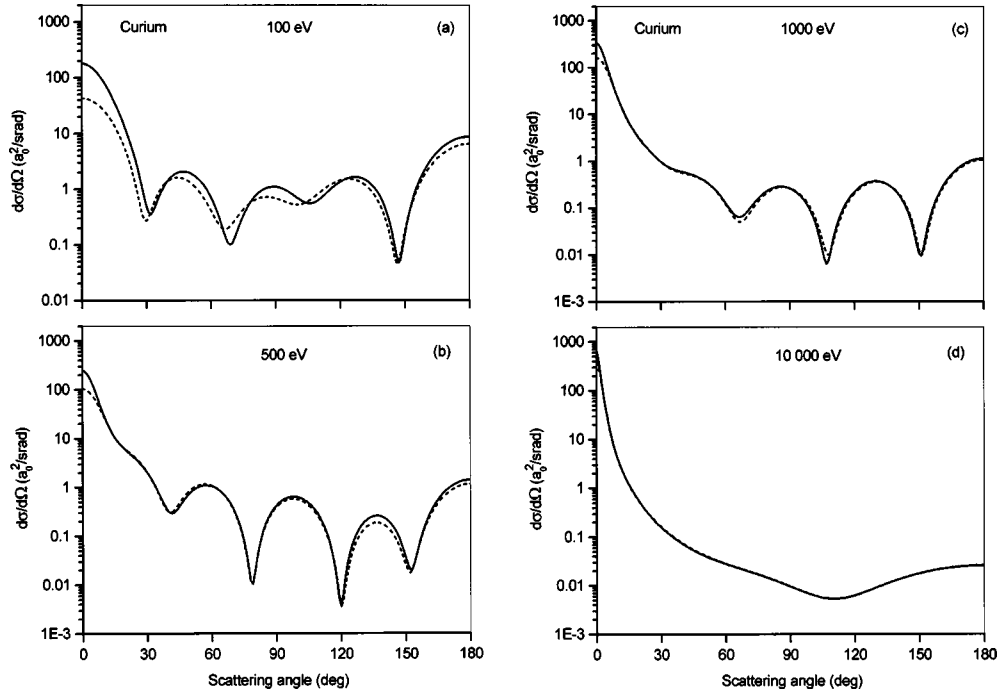

FIG. 7. Differential elastic-scattering cross sections, $d\sigma/d\Omega$, calculated for curium for two potentials as a function of scattering angle: (solid line) DHF potential; (dashed line) TFD potential: (a) energy of 100 eV; (b) energy of 500 eV; (c) energy of 1000 eV; and (d) energy of 10 000 eV.

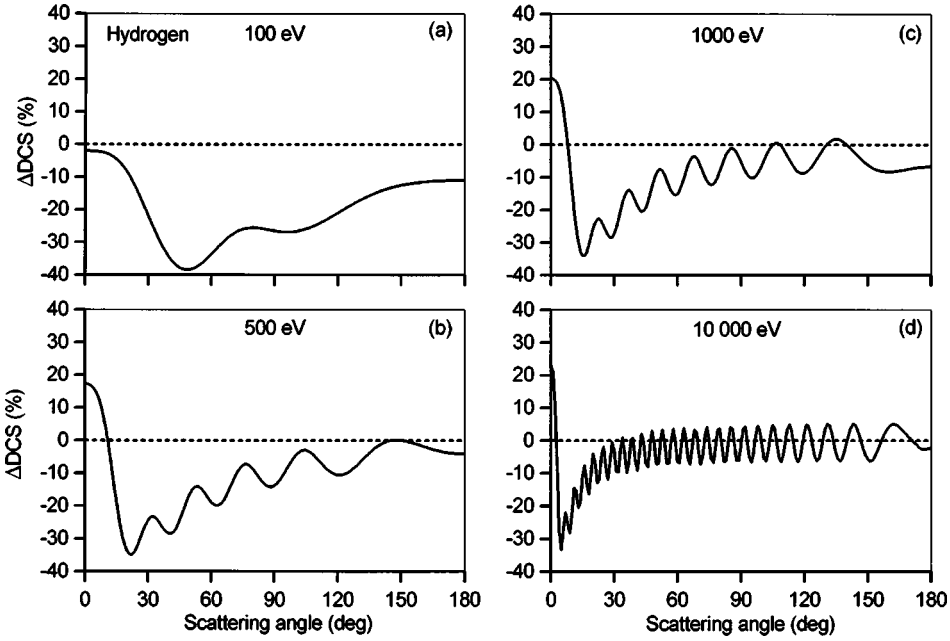

FIG. 8. Percentage differences between differential elastic-scattering cross sections, ΔDCS, calculated for hydrogen from Eq. (18) for the TFD and DHF potentials as a function of scattering angle, θ: (a) energy of 100 eV; (b) energy of 500 eV; (c) energy of 1000 eV; and (d) energy of 10 000 eV.

1 and 10 keV. Generally, the observed deviations are much smaller than those found in comparisons of DCSs from the TFD and DHF potentials that were considered in Sec. 7.1. The differences are not visible in semilogarithmic plots showing the DCSs as functions of scattering angle (such as Figs. 2–7); the plots seem to be identical within the thickness of the lines. Thus, as a measure of relative deviations, we used an expression similar to Eq. (22)

$$\Delta\mathrm{DCS} = 100(\mathrm{DCS}_{\mathrm{BS}}^{\mathrm{DHF}} - \mathrm{DCS}_{\mathrm{JSP}}^{\mathrm{DHF}})/\mathrm{DCS}_{\mathrm{JSP}}^{\mathrm{DHF}}, \qquad (23)$$

where $\mathrm{DCS}_{\mathrm{BS}}^{\mathrm{DHF}}$ is the differential elastic-scattering cross section taken from the Berger and Seltzer database, and $\mathrm{DCS}_{\mathrm{JSP}}^{\mathrm{DHF}}$ is the differential elastic-scattering cross section taken from the Jablonski, Salvat, and Powell database. Plots of ΔDCS are shown as a function of scattering angle for H, Al, Ni, Ag, Au, and Cm at the two energies in Fig. 15. We see that for elements and energies where there are no pronounced minima in the DCSs (Figs. 2–7), the differences between cross sections are very small. For H, Al, Ni, and Ag, the differences do not exceed 0.02% for most scattering angles. Slightly larger deviations are observed for scattering angles near 180° where the deviation reaches −0.28% for hydrogen at 10 000 eV. A common feature of Figs. 15(a)–15(d) is a fine oscillatory structure. This is probably due to the different number of l terms in the partial-wave series used in the calculations of DCSs. For high-atomic-number elements, the

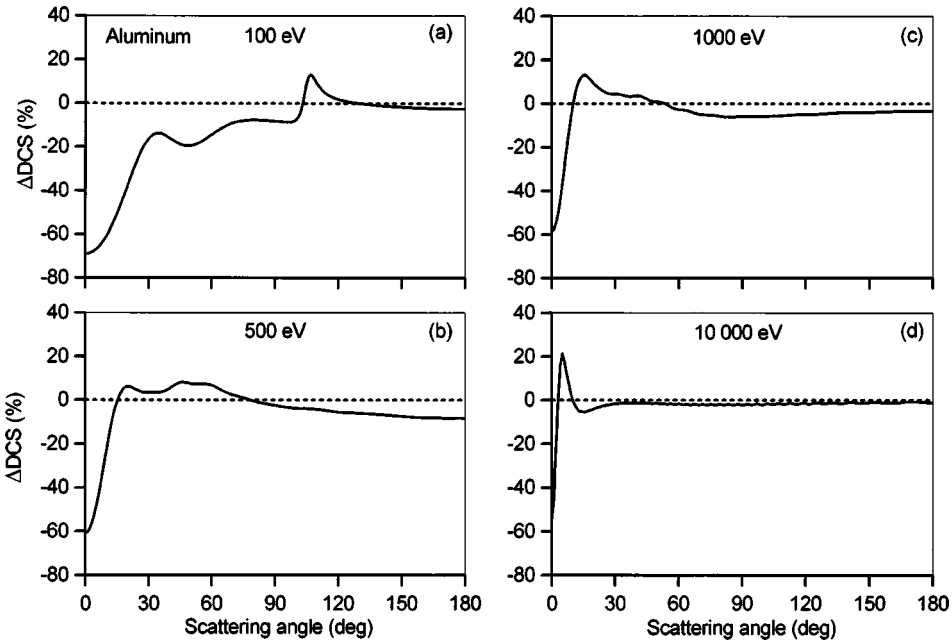

FIG. 9. Percentage differences between differential elastic-scattering cross sections, ΔDCS, calculated for aluminum from Eq. (18) for the TFD and DHF potentials as a function of scattering angle, θ: (a) energy of 100 eV; (b) energy of 500 eV; (c) energy of 1000 eV; and (d) energy of 10 000 eV.

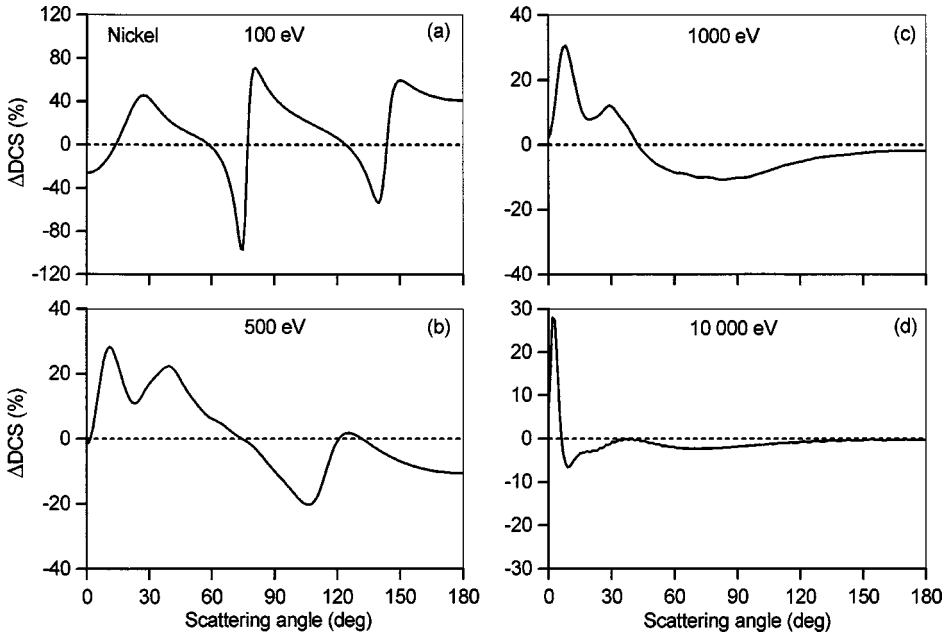

FIG. 10. Percentage differences between differential elastic-scattering cross sections, ΔDCS, calculated for nickel from Eq. (18) for the TFD and DHF potentials as a function of scattering angle, θ: (a) energy of 100 eV; (b) energy of 500 eV; (c) energy of 1000 eV; and (d) energy of 10 000 eV.

oscillations are much less pronounced. However, the deviations are larger than for low- and medium-atomic-number elements. For gold, the largest deviation is -0.3%, and for curium $\pm 1\%$. Furthermore, the largest deviations observed for Au and Cm at 1000 eV occur in the same positions as the deep minima in the DCSs.

We find that the DCSs from the two databases considered are practically equivalent. For the low- and medium-atomic-number elements, the agreement is within 3–4 decimal places. Larger deviations, observed for high-atomic-number elements, should be ascribed to the different exchange potentials used in the respective algorithms. Some part of the deviations might possibly be due to numerical round-off errors and interpolation errors. These contributions, however, do not seem to be significant.

An obvious question arises as to the magnitude of the contribution to the DCS due to the exchange correction. To evaluate this contribution, the algorithm described in Sec. 4 has been used in calculations of the DCSs that include or neglect the exchange correction [cf. Eq. (13)]. The deviations between calculated DCSs were determined from an equation similar to Eq. (23)

$$\Delta\mathrm{DCS} = 100(\mathrm{DCS}_{\mathrm{nexc}}^{\mathrm{DHF}} - \mathrm{DCS}_{\mathrm{exc}}^{\mathrm{DHF}})/\mathrm{DCS}_{\mathrm{exc}}^{\mathrm{DHF}}, \qquad (24)$$

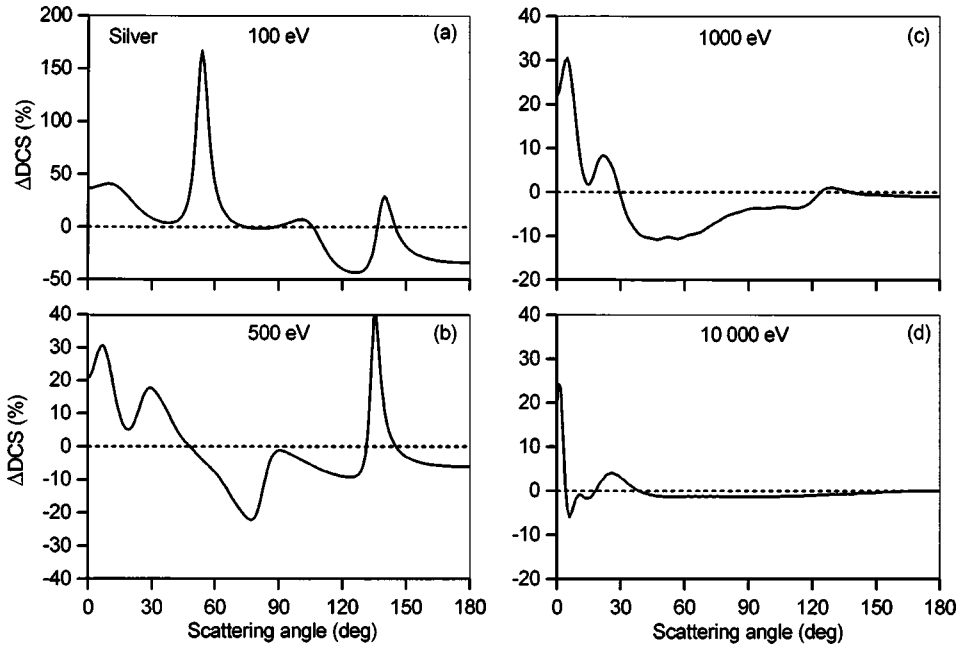

FIG. 11. Percentage differences between differential elastic-scattering cross sections, ΔDCS, calculated for silver from Eq. (18) for the TFD and DHF potentials as a function of scattering angle, θ: (a) energy of 100 eV; (b) energy of 500 eV; (c) energy of 1000 eV; and (d) energy of 10 000 eV.

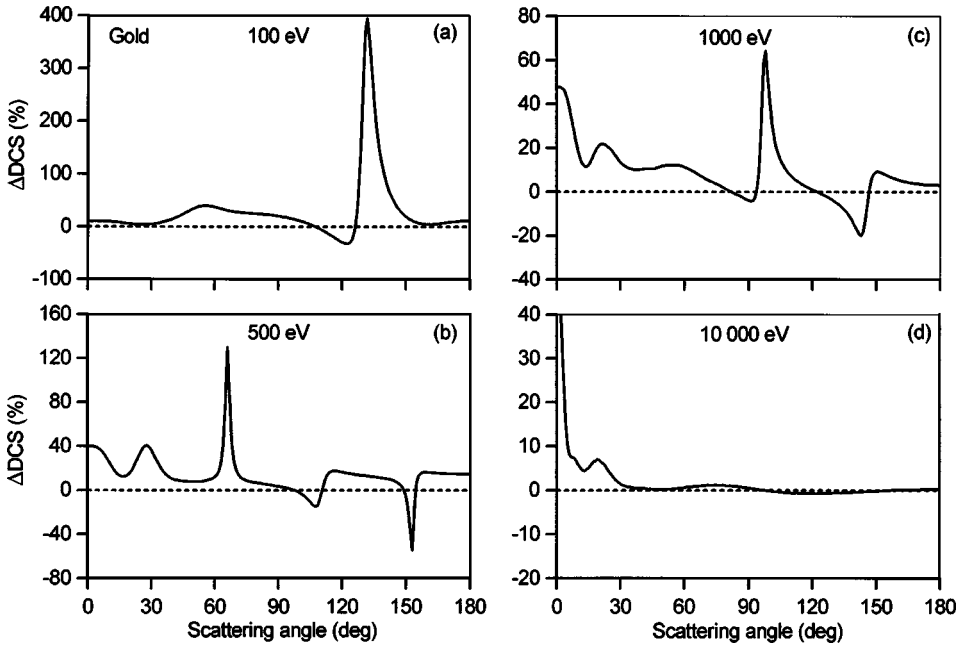

FIG. 12. Percentage differences between differential elastic-scattering cross sections, ΔDCS, calculated for gold from Eq. (18) for the TFD and DHF potentials as a function of scattering angle, θ: (a) energy of 100 eV; (b) energy of 500 eV; (c) energy of 1000 eV; and (d) energy of 10 000 eV.

where $\mathrm{DCS}_{\mathrm{exc}}^{\mathrm{DHF}}$ is the DCS calculated with the exchange correction and $\mathrm{DCS}_{\mathrm{nexc}}^{\mathrm{DHF}}$ is the DCS calculated with neglect of the term $V_{\mathrm{exc}}(r)$ in Eq. (13). Values of ΔDCS from Eq. (24) are shown as a function of scattering angle for H, Al, Ni, Ag. Au, and Cm in Fig. 16 at the two electron energies. We see that the contribution of the exchange potential to the DCS can be substantial, in particular, for elements and energies for which there are deep minima in the DCSs (Ag, Au, and Cm at 1 keV). In the vicinity of minima, the deviations between DCSs may exceed 35%. The DCSs for H, Al, and Ni at 1 keV differ by up to 5%. Smaller deviations are observed at 10 keV where the deviations usually do not exceed 2%. In all cases, the values of ΔDCS are much larger, by up to 2–3 orders of magnitude, than the deviations between DCSs from the two databases considered here [cf. Figs. 15(a) and 16(a), or Figs. 15(c) and 16(c)].

We therefore conclude that the exchange correction of Riley and Truhlar[75] leads to practically identical DCSs as the correction of Furness and McCarthy.[64] The slight differences between these DCSs are considerably smaller than the differences due to neglect of the exchange correction.

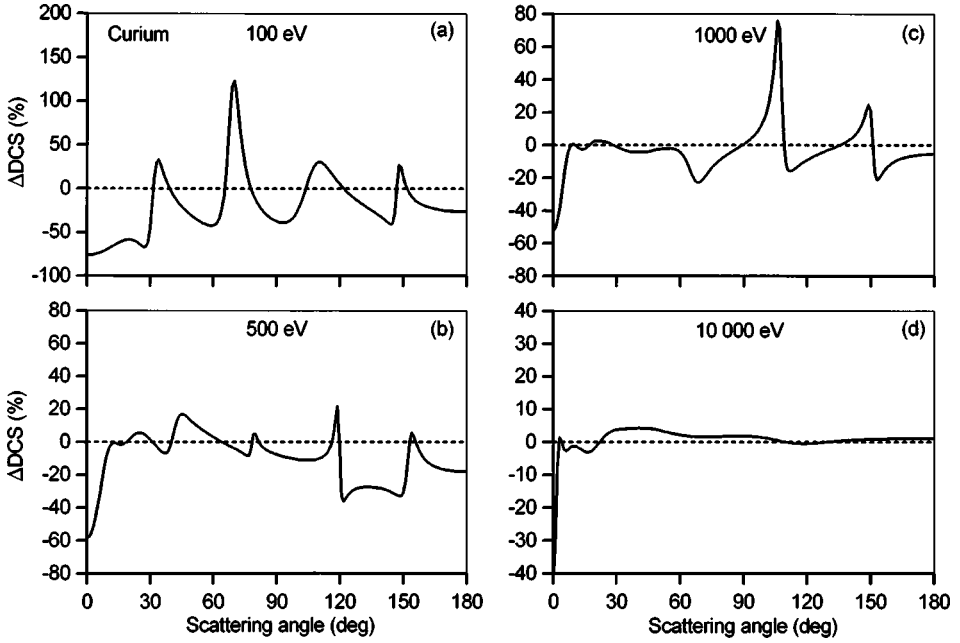

FIG. 13. Percentage differences between differential elastic-scattering cross sections, ΔDCS, calculated for curium from Eq. (18) for the TFD and DHF potentials as a function of scattering angle, θ: (a) energy of 100 eV; (b) energy of 500 eV; (c) energy of 1000 eV; and (d) energy of 10 000 eV.

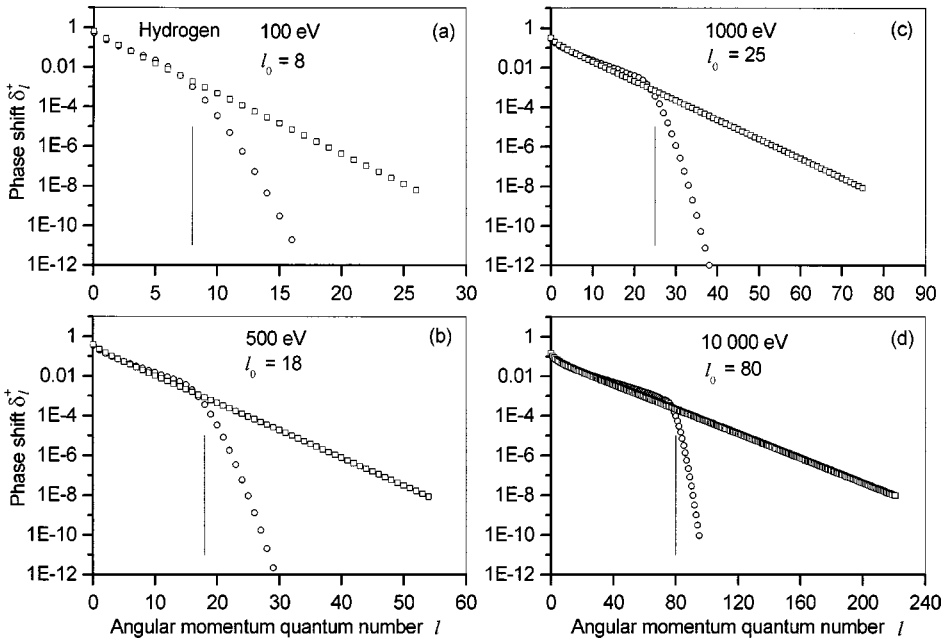

FIG. 14. Comparison of phase shifts, δ_l^+, for hydrogen corresponding to the potentials used in the calculations: (squares) the DHF potential; (circles) the TFD potential: (a) energy of 100 eV; (b) energy of 500 eV; (c) energy of 1000 eV; and (d) energy of 10 000 eV. Vertical lines indicate the values of l_0 calculated from Eq. (22).

7.4. Comparisons of Differential Cross Sections Obtained from the TFD and DHF Potentials with Measured Differential Cross Sections

We present illustrative comparisons here of DCSs calculated from the TFD and DHF potentials with measured DCSs for six elements (He, Ne, Ar, Kr, Xe, and Hg) at energies between 50 and 3000 eV. These elements were selected because in most cases there were at least two independent measurements available for the chosen electron energies. In some cases (Ne at 800 eV; Ar at 800 eV, 2000 eV, and 3000 eV; Kr at 750 eV; Xe at 750 eV; Hg at 500 eV), measured DCSs from a single source were used to extend the range of electron energy or atomic number in the comparisons. For all such sources, DCS measurements were available at other energies and were in satisfactory agreement with results from other groups. The calculated cross sections in these comparisons were obtained from Version 2.0[10] (for the TFD potential) and Version 3.0[12] (for the DHF potential) of the NIST Electron Elastic-Scattering Cross-Section Database.

Several review articles have identified and discussed requirements for reliable measurements of differential elastic-scattering and other cross sections in electron–atom interactions.[76–80] The requirements relevant to elastic-DCS measurements include knowledge of the uncertainties in measurements of the incident electron-beam current, the beam energy, the effective product of path length of the beam in the scattering gas and solid angle of the detector system, the scattered-electron current, and the gas pressure. In addition, the gas pressure clearly has to be low enough to avoid unwanted multiple-scattering effects.

Figures 17–22 show measured[81–106] and calculated DCS values for He (at 50, 100, 300, 500, and 700 eV), Ne (at 100, 300, 500, and 800 eV), Ar (at 50, 100, 300, 500, 800, 1000, 2000, and 3000 eV), Kr (at 100, 200, 500, and 750 eV), Xe (at 50, 100, 200, 400, and 750 eV), and Hg (at 100, 150, 300, and 500 eV), respectively. The standard uncertainty in the measured DCS values has been typically estimated by the authors of the reported DCS measurements to be between 5% and 25%. Examination of the measured DCSs for Ar at 100 eV in Fig. 19(b), the element and energy for which there is the largest number of independent measurements (9), shows that the ratio of the largest DCS to the smallest DCS at a scattering angle away from the minimum can be up to about 1.8. The measurements of Vuskovic and Kurepa[95] appear to be systematically larger than the other measurements for most scattering angles; if their results are excluded, the ratio of the largest DCS to the smallest DCS is less than 1.5. Similar inspections of other figures where there are three or more DCS measurements at various scattering angles (e.g., He at 50 eV and 100 eV in Figs. 17; Ne at 100 eV in Fig. 18(a); Ar at 500 eV in Fig. 19(b); Kr at 100 and 200 eV in Fig. 20; Xe at 100 and 200 eV in Fig. 21; and Hg at 100 and 300 eV in Fig. 22) indicate that the consistency of the measured DCSs is typically within $\pm 25\%$ although there are some larger ranges [e.g., for He at 100 eV in Fig. 17(b) and for Kr at 200 eV in Fig. 20(b)]. We also note that the measurements of Kurepa and Vuskovic[84] for He at 100 eV in Fig. 17(b) are also systematically larger than the other measurements shown, a result consistent with the Ar data in Fig. 19(b).

We now consider the extent to which the measured DCSs agree with the calculated DCSs as a function of electron energy. Argon is the element for which there are two or more DCS measurements over the energy range from 50 eV to 1 keV (with additional data from one group at 2 and 3 keV). Figures 19(g) and 19(h) show that there is excellent agreement between the measured DCSs and the DCSs from both the TFD and DHF potentials. At lower energies, the mea-

sured DCS agree generally better with DCSs from the DHF potential than the TFD potential [e.g., in the positions and magnitudes of the deep minima in Figs. 19(a) and 19(b)], although it is clear that the measured DCSs are smaller than the computed DCSs at other scattering angles. For other elements, there is generally close agreement between the measured DCSs and the DCSs calculated from the DHF potential at the highest available energies [e.g., He at 700 eV in Fig. 17(e); Ne at 800 eV in Fig. 18(d); Kr at 750 eV in Fig. 20(d); Xe at 750 eV in Fig. 21(e); and Hg at 500 eV in Fig. 22(d)]. At lower energies, the measured DCSs are often smaller than the calculated DCSs for most scattering angles, and the deviations between the measured DCSs and the DCSs from the DHF potential generally become larger with decreasing energy. In most cases, the DCSs from the DHF potential agree better with the measured DCSs in the vicinity of deep minima than DCSs from the TFD potential [e.g., for Ne at 100 eV in Fig. 18(a); Kr at 100 eV in Fig. 20(a); Xe in Fig. 21; and Hg at 300 eV in Fig. 22(c)]. There are some situations, however, where the reverse occurs [e.g., for Kr at 200 eV in Fig. 20(b) and Hg at 100 and 150 eV in Fig. 22], although the result for Kr might be associated with limited angular resolution in the experiments for the particularly narrow minimum expected at a scattering angle of about 81°. Finally, we point out that the measured DCSs are larger than the DCSs from the DHF potential, particularly at lower energies, for scattering angles less than about 25° (particularly He in Fig. 17; Ne at 100, 300, and 500 eV in Fig. 18; Ar at 50, 100, 300, and 500 eV in Fig. 19; Kr at 100 and 200 eV in Fig. 20; Xe at 50 and 100 eV in Fig. 21; and Hg in Fig. 22). The range of scattering angles where these positive differences occur nevertheless gets smaller with increasing electron energy.

For electron energies below 1 keV, the DCSs calculated from the DHF potential have the same shapes as a function of scattering angle as the measured DCSs and the correct number of minima. The absolute values of these DCSs for scattering angles larger than about 25°, however, are systematically larger than the measured DCSs, as just noted. The cause for this systematic difference is believed to be the neglect of absorption (or inelastic-scattering) effects that cannot be accounted for in the calculational algorithm.[107] In principle, these absorption effects can be described by an imaginary potential;[107,108] an imaginary potential in the Schroedinger equation is equivalent to a loss of particles,[109] a result to be expected due to open inelastic channels. Unfortunately, this approach is difficult to implement. On the one hand, it is hard to calculate the local absorption potential from first principles,[107] because it depends on the details of the wave functions of excited atomic states. On the other hand, the solution of the radial equations for complex potentials requires numerical algorithms different from those used for real potentials.

A second intrinsic limitation of the DCSs calculated from the DHF potential is the atomic polarizability correction. This correction, which can be described empirically by means of a long-range polarization potential ($\propto r^{-4}$) for the gas phase, increases the DCS at relatively small scattering angles and is responsible for the deviations mentioned above in this angular range.

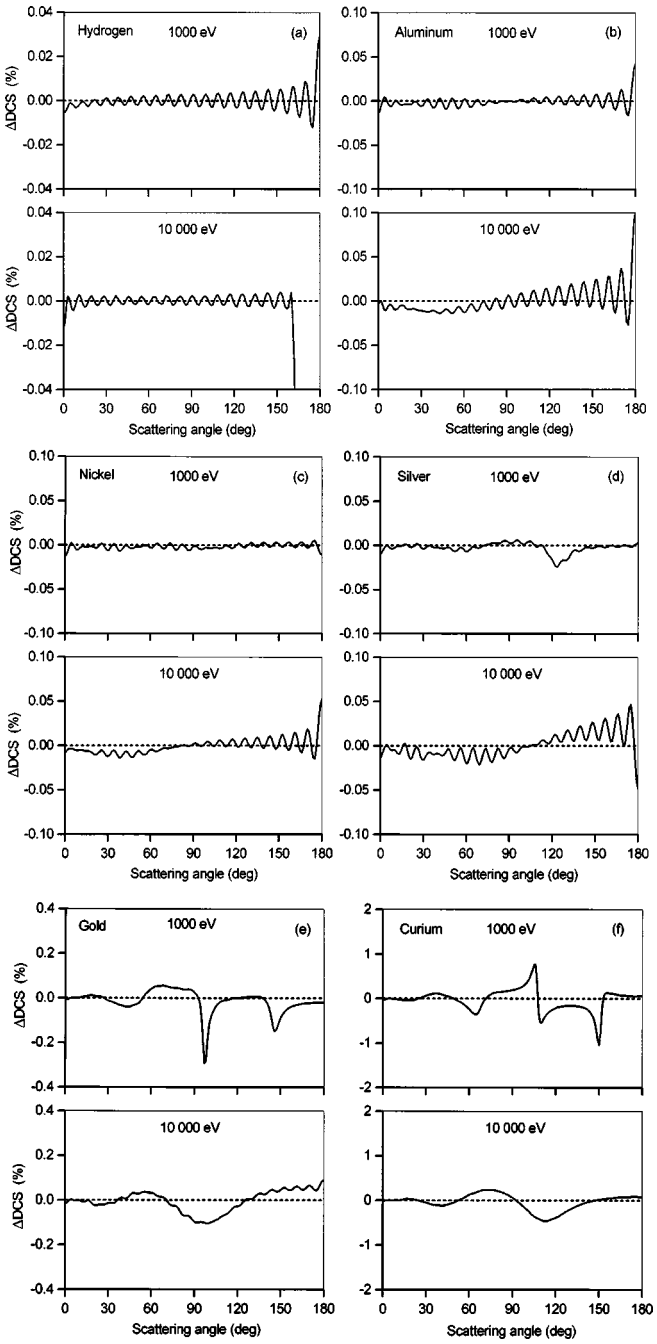

FIG. 15. Percentage differences between differential elastic-scattering cross sections, ΔDCS, obtained from the Berger and Seltzer (Ref. 11) database and the Jablonski *et al.* (Ref. 12) database at energies of 1000 and 10 000 eV from Eq. (23) as a function of scattering angle, θ: (a) hydrogen; (b) aluminum; (c) nickel; (d) silver; (e) gold; and (f) curium.

The arguments that lead to an imaginary potential and a long-range polarization potential in elastic-electron scattering are the following. In a perturbation expansion of the elastic-transition rate to second order, the second-order terms involve virtual transitions to excited states. As mentioned above, the formalism is very involved because it requires

knowing the wave functions of excited states. A method to bypass this difficulty is based on the so-called eikonal theory that allows the calculation of the scattering amplitude to second order in terms of only the ground-state wave function.[107] From the eikonal scattering amplitude, one can obtain an ''equivalent'' approximate local potential that yields approximately the eikonal scattering amplitude. This potential consists of the electrostatic potential used in our calculations and a second-order term that is complex. The real part of this term corresponds to the polarization potential, and the imaginary part is the absorption potential. Alternatively, approximate absorption and polarization potentials can be obtained from semiclassical arguments (see Ref. 108 and references therein). Recently, Salvat[110] has proposed a semiempirical optical-model potential in which the absorption and short-range polarization potentials are obtained from the local density approximation, i.e., by assuming that the atomic electron cloud behaves locally as an homogeneous electron gas. The model parameters, determined by fitting a large set of experimental DCS data (essentially those presented in Figs. 17–22), were found to be essentially independent of the energy of the projectile and the atomic number of the target atom. Although this type of approach yields more accurate DCSs at low energies, calculations are substantially more difficult than for the TFD and DHF potentials considered here. For condensed matter, there is no empirical information available on the magnitude of the polarizability and absorption effects. In principle, the absorption correction should be similar to that for the gas phase. The polarization potential is expected to be much weaker than for the gas phase because both the polarizing field of the projectile and the field of the induced atomic dipole will be screened by the medium.[111] It should also be noted that it is customary to construct a muffin-tin potential for solids to describe elastic-electron scattering in the medium. This change from an atomic potential will modify the DCSs at small scattering angles[6,11] but the resulting changes are in the opposite direction to the atomic-polarizability correction. The long-range polarization field is attractive. This field therefore increases the DCS at small angles where, classically, trajectories have large impact parameters and the projectile sees only the ''tail'' of the potential. On the other hand, the muffin-tin potential for a solid vanishes outside the muffin-tin sphere. As a result, the tail of the atomic potential is suppressed and the small-angle DCS for an atom in a solid is smaller (in the absence of polarization) than the corresponding DCS for a free atom. In practice, the degree of partial cancellation of these two effects will depend on atomic number and electron energy.

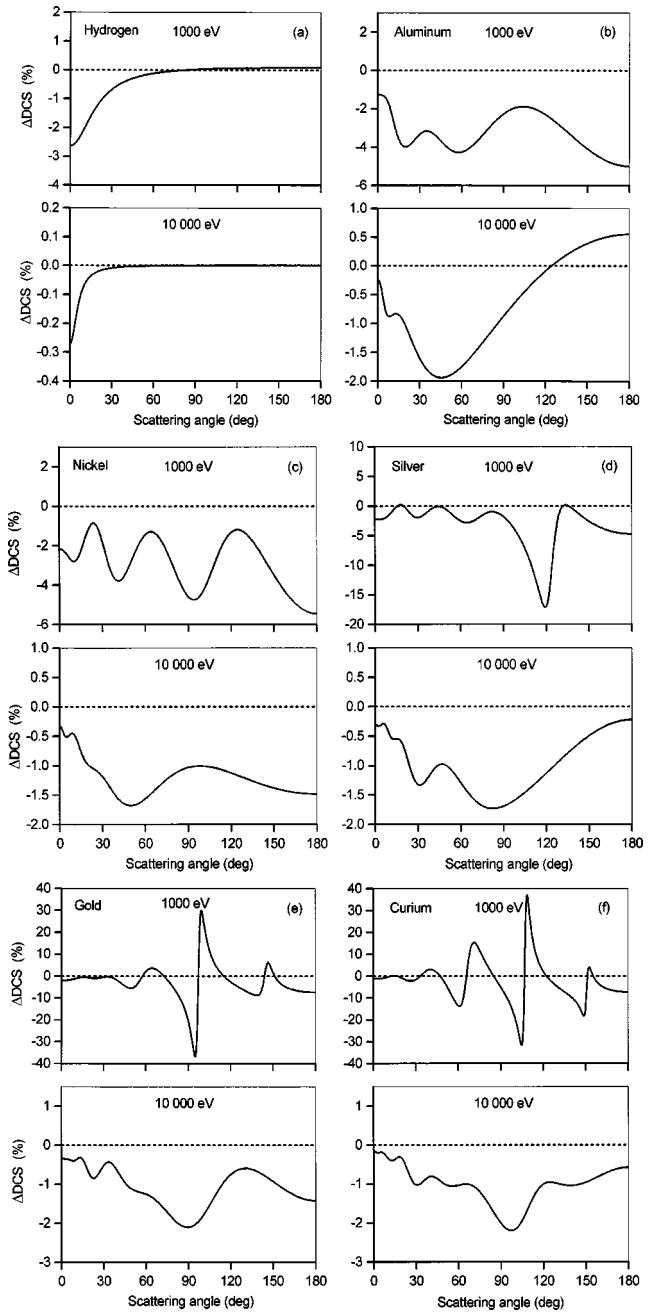

FIG. 16. Percentage differences between differential elastic-scattering cross sections, ΔDCS, with and without exchange correction calculated at energies of 1000 and 10 000 eV from Eq. (24) as a function of scattering angle, θ: (a) hydrogen; (b) aluminum; (c) nickel; (d) silver; (e) gold; and (f) curium.

8. Comparisons of Transport Cross Sections

8.1. Comparisons of Transport Cross Sections Obtained from the TFD and DHF Potentials

The energy dependences of the TCSs for H, Al, Ni, Ag, Au, and Cm obtained from the TFD and DHF potentials are compared in Fig. 23; these TCS values were obtained from Versions 2.0[10] and 3.0,[12] respectively, of the NIST Electron Elastic-Scattering Cross-Section Database. We see that the agreement is generally rather good. With the exception of energies below about 200 eV, the dependences seem to be nearly identical. To evaluate the deviations between the TCSs quantitatively, let us consider the following percentage difference, $\Delta\sigma_{tr}$:

$$\Delta\sigma_{tr} = 100(\sigma_{tr}^{TFD} - \sigma_{tr}^{DHF})/\sigma_{tr}^{DHF}, \qquad (25)$$

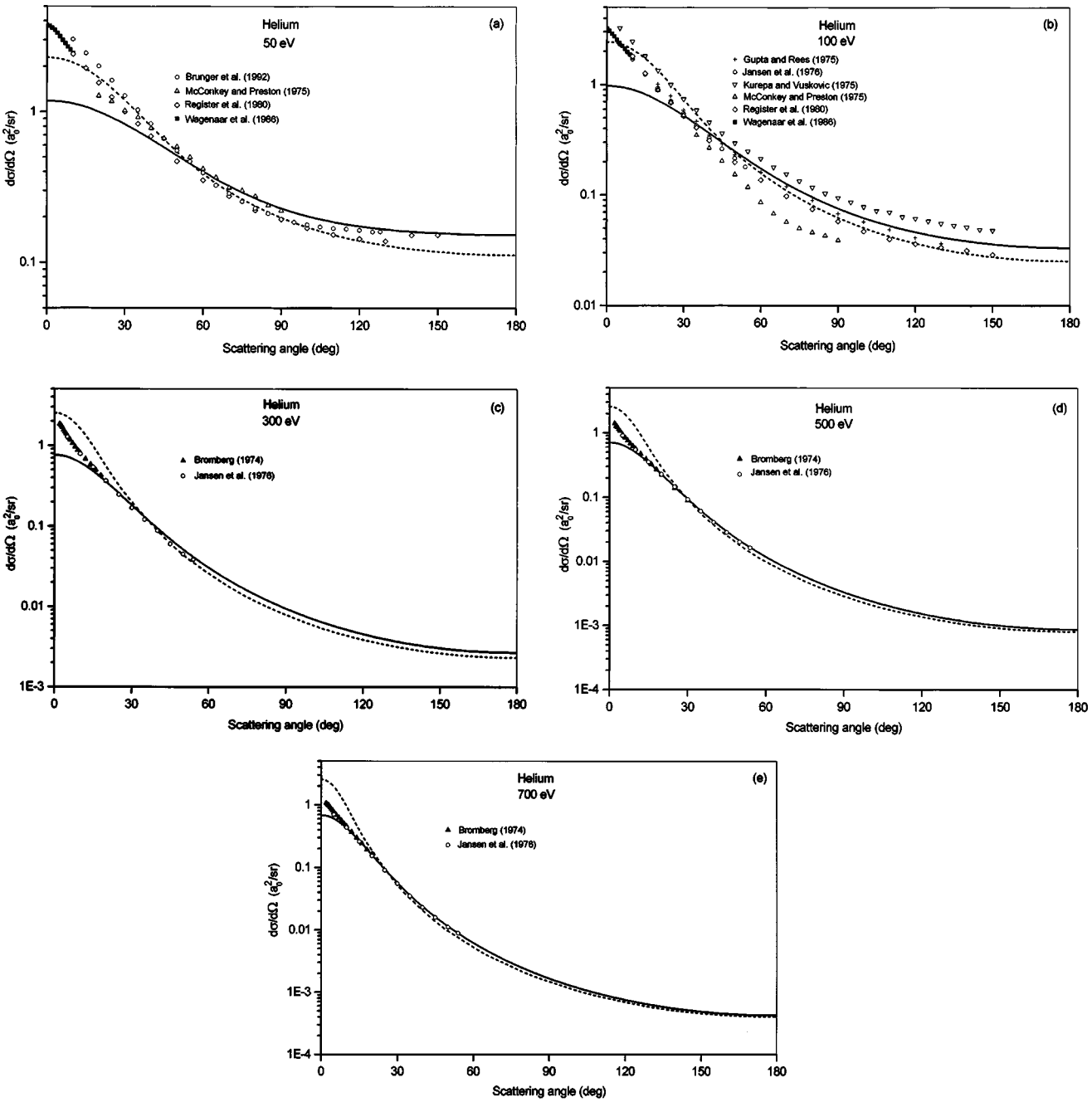

FIG. 17. Comparison of differential elastic-scattering cross sections, $d\sigma/d\Omega$, calculated for helium for two potentials as a function of scattering angle with measured differential cross sections: (solid line) DHF potential; (dashed line) TFD potential: (a) energy of 50 eV; (b) energy of 100 eV; (c) energy of 300 eV; (d) energy of 500 eV; (e) energy of 700 eV. The symbols show the measurements of Bromberg,[81] McConkey and Preston,[82] Gupta and Rees,[83] Kurepa and Vuskovic,[84] Jansen *et al.*,[85] Register *et al.*,[86] Wagenaar *et al.*,[87] and Brunger *et al.*[88]

where σ_{tr}^{TFD} and σ_{tr}^{DHF} are the transport cross sections resulting from the TFD and DHF potentials, respectively. Values of $\Delta\sigma_{tr}$ for the six elements are shown as a function of energy in Fig. 24. Above 200 eV, the largest percentage difference is observed for hydrogen. The value of $\Delta\sigma_{tr}$ is close to 20% for H at 200 eV, and decreases with increasing energy to 10% at 20 000 eV. For low and medium atomic number elements (Al,Ni,Ag), the value of $\Delta\sigma_{tr}$ is less than 5% for energies above 200 eV. At lower energies, however, $\Delta\sigma_{tr}$ may exceed 40%. For high atomic number elements (Au and Cm), $\Delta\sigma_{tr}$ varies considerably in the energy range up to 1000 eV, and exceeds 20% at some energies. For energies larger than 1000 eV, $\Delta\sigma_{tr}$ is less than 5%.

A similar analysis, for the same potentials, was published by Jablonski and Powell[33] for Be, C, Al, Cu, Ag, and Au. The energy range considered by these authors, however, was smaller (100 eV–10 keV) than that considered here. Furthermore, the percentage difference between DCS values was defined by a slightly different relation than Eq. (25). None-

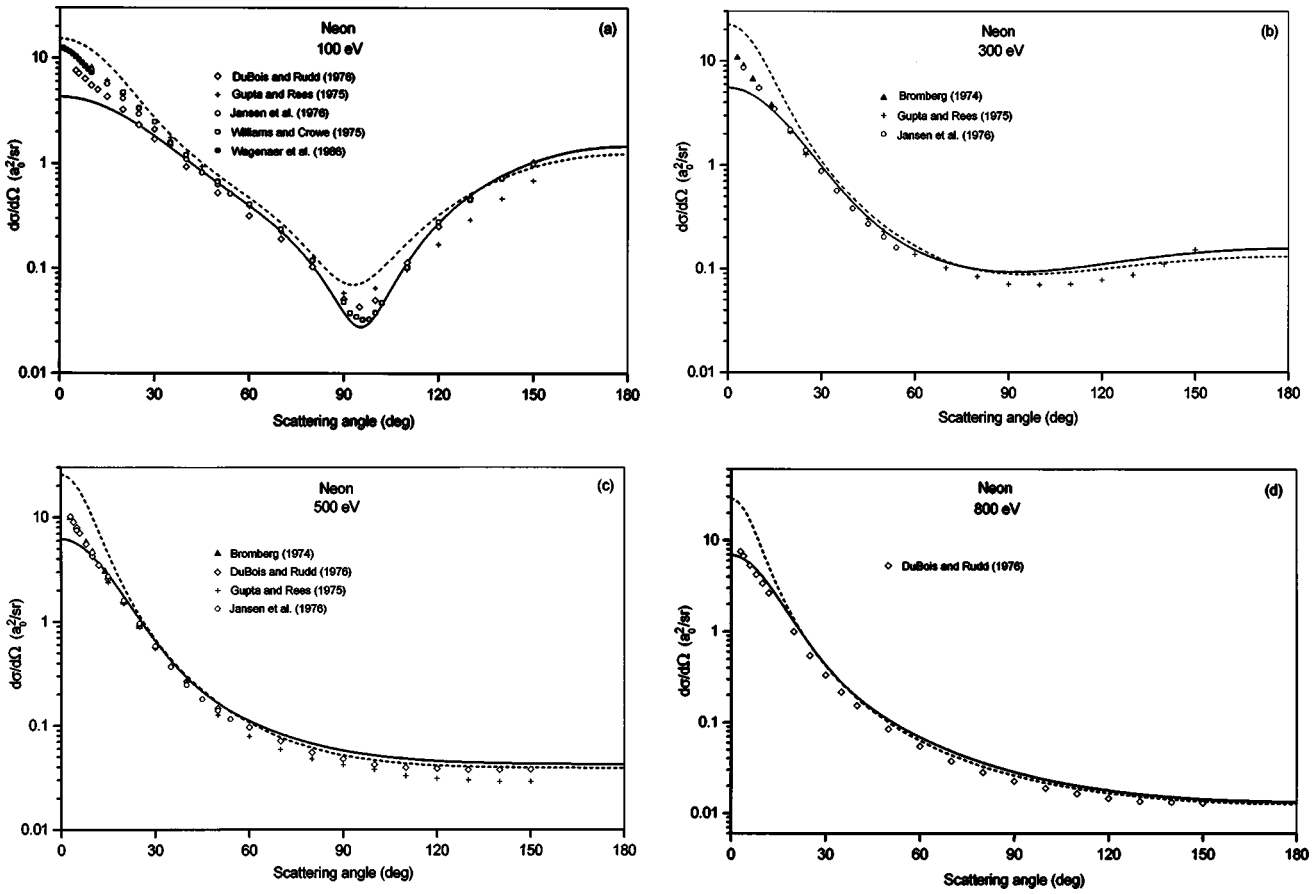

FIG. 18. Comparison of differential elastic-scattering cross sections, $d\sigma/d\Omega$, calculated for neon for two potentials as a function of scattering angle with measured differential cross sections: (solid line) DHF potential; (dashed line) TFD potential: (a) energy of 100 eV; (b) energy of 300 eV; (c) energy of 500 eV; and (d) energy of 800 eV. The symbols show the measurements of DuBois and Rudd,[89] Gupta and Rees,[90] Jansen *et al.*,[85] Williams and Crowe,[91] Wagenaar *et al.*,[87] and Bromberg.[81]

theless, the energy dependences of $\Delta\sigma_{tr}$ found by Jablonski and Powell[33] are very similar to the dependences shown in Fig. 24.

8.2 Comparisons of Transport Cross Sections Obtained from the TFD and DHF Potentials with Measured Transport Cross Sections

Elford and Buckman[112] have discussed experimental determinations of transport cross sections (often also referred to as momentum-transfer cross sections). For electron energies of interest here, TCSs are determined from measured DCSs and Eq. (20). Unfortunately, it is not generally possible to measure DCSs over the complete range of scattering angles due to the difficulty of defining the interaction volume accurately for small scattering angles and to geometrical constraints for large scattering angles. As a result, it is necessary either to extrapolate measured DCSs to scattering angles of 0 and π, perhaps using calculated DCSs as a guide, or to fit measured DCSs as a function of scattering angle with Eqs. (2) and (3) using a selected number of phase shifts as free parameters. The latter approach can be useful for low electron energies ($E \leqslant 200$ eV) where the number of phase shifts is sufficiently small.[113,114]

Elford and Buckman have published "preferred" TCS values for a number of atoms based on an analysis of measurements and calculations.[112] Most of the preferred TCSs are for electron energies of less than 10 eV although some data are given for energies of up to 100 eV. We show illustrative TCSs in Table 3 for two atoms, He and Hg, that are based on measured DCSs for electron energies of 50 and 100 eV.[86,88,104] Register *et al.*[86] and Brunger *et al.*[88] derived TCSs after performing a phase-shift analysis of their DCSs while Panajotovic *et al.*[104] obtained TCSs after extrapolating their DCSs to 0 and π. For Hg and an energy of 100 eV, the experimental TCSs are smaller than the calculated TCSs by about a factor of two, as would be expected from a casual inspection of Fig. 22(a).

9. Comparisons of Quantities Derived from Differential Cross Sections that were Obtained from the TFD and DHF Potentials

Differential elastic-scattering cross sections are used for a variety of purposes, as noted in Sec. 1. We discuss here the extent to which certain quantities derived from DCSs may

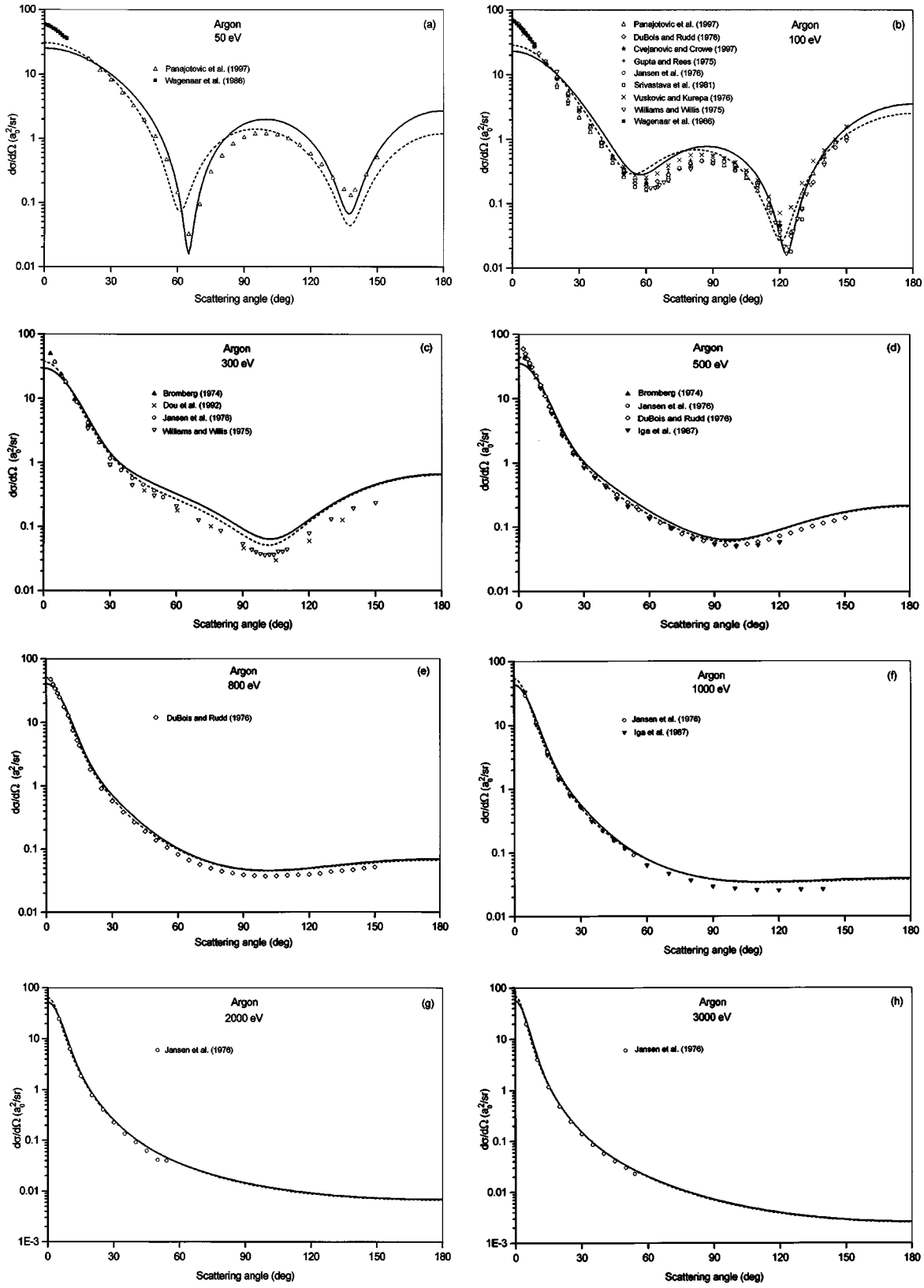

FIG. 19. Comparison of differential elastic-scattering cross sections, $d\sigma/d\Omega$, calculated for argon for two potentials as a function of scattering angle with measured differential cross sections: (solid line) DHF potential; (dashed line) TFD potential: (a) energy of 50 eV; (b) energy of 100 eV; (c) energy of 300 eV; (d) energy of 500 eV; (e) energy of 800 eV; (f) energy of 1000 eV; and (g) energy of 2000 eV; energy of 3000 eV. The symbols show the measurements of Panajotovic *et al.*,[92] Wagenaar *et al.*,[87] DuBois and Rudd,[89] Cvejanovic and Crowe,[93] Gupta and Rees,[83] Jansen *et al.*,[85] Srivastava *et al.*,[94] Vuskovic and Kurepa,[95] Williams and Willis,[96] Bromberg,[81] Dou *et al.*,[97] and Iga *et al.*[98]

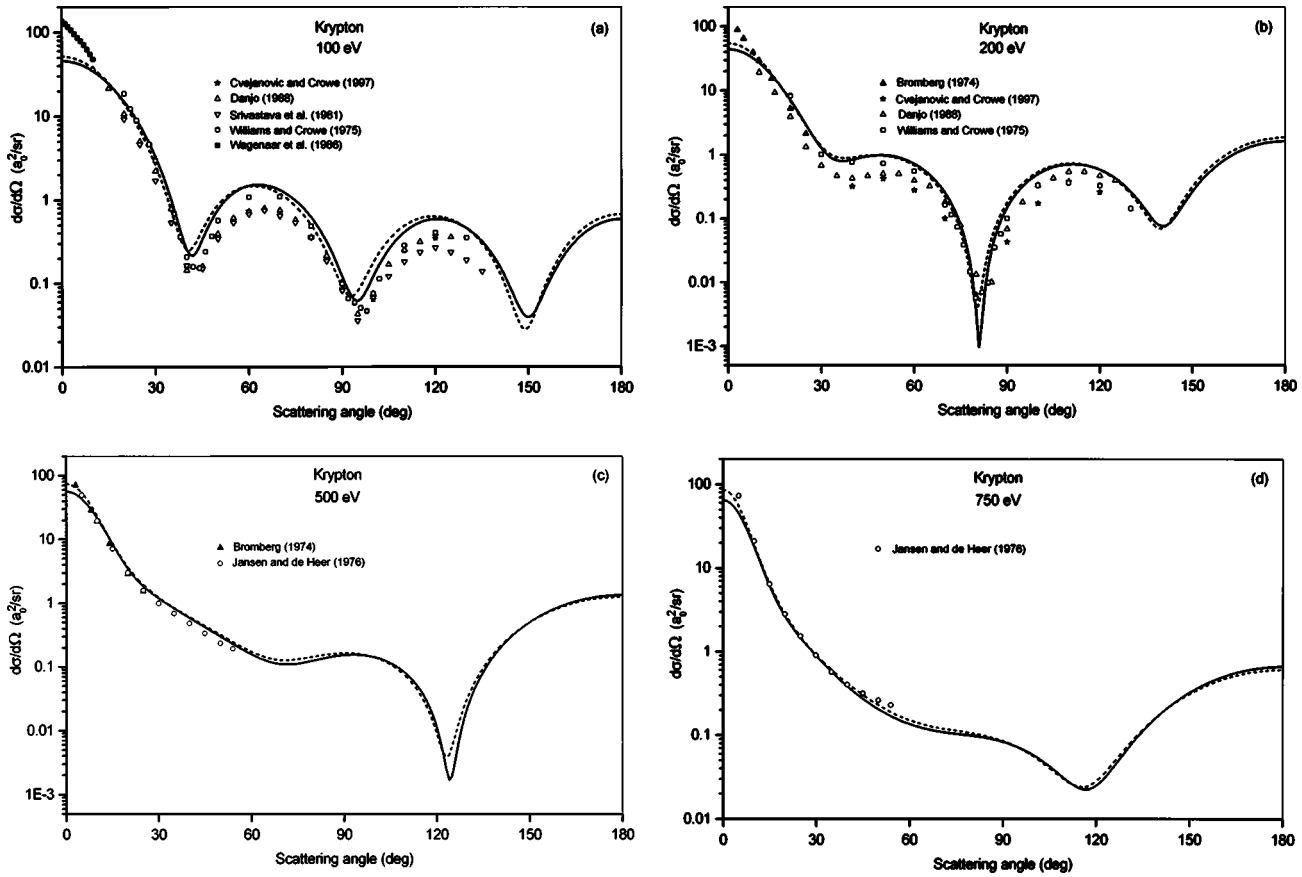

FIG. 20. Comparison of differential elastic-scattering cross sections, $d\sigma/d\Omega$, calculated for krypton for two potentials as a function of scattering angle with measured differential cross sections: (solid line) DHF potential; (dashed line) TFD potential: (a) energy of 100 eV; (b) energy of 200 eV; (c) energy of 500 eV; and (d) energy of 750 eV. The symbols show the measurements of Cvejanovic and Crowe,[93] Danjo,[99] Srivastava *et al.*,[94] Williams and Crowe,[91] Wagenaar *et al.*,[87] Bromberg,[81] and Jansen and de Heer.[100]

vary depending on whether the cross sections were obtained from the TFD or DHF potentials. Specific consideration is given here to three quantities relevant to materials characterization: (1) elastic-backscattered intensities for an overlayer-film on a substrate; (2) electron inelastic mean free paths determined by elastic-peak electron spectroscopy; and (3) mean escape depths for signal electrons in AES and XPS. Comparisons will be made of these quantities for DCSs obtained, as before, from the TFD and DHF potentials, specifically Versions 2.0[10] and 3.0,[12] respectively, of the NIST Electron Elastic-Scattering Cross-Section Database.

9.1 Elastic-Backscattered Intensities for an Overlayer Film on a Substrate

Elastic-scattering cross sections are needed for a description of elastic backscattering of electrons from solid surfaces. An electron impinging on the solid surface may leave the solid as a result of multiple elastic collisions. The process of multiple scattering, however, is usually dominated by one large-angle elastic collision. We have seen from Figs. 8–13 that the largest differences between DCSs calculated from the DHF and TFD potentials occur at scattering angles corresponding to deep minima in the DCSs. The scattering potential for the solid will, in general, be different from that of the corresponding neutral atom (see also Sec. 9.4). It is possible that the deep minima in the DCSs for atoms shown in Figs. 2–7 may occur for the DCSs in solids at different scattering angles and with different strengths. We therefore suggest that, where possible, experimental configurations be avoided for which the DCS has a deep minimum. Otherwise, simulations describing elastic backscattering might have large uncertainties.

Problems associated with the theory of elastic backscattering were demonstrated in studies of gold overlayers deposited on nickel.[115,116] In the experimental configuration used by Jablonski *et al.*,[115] the direction of the electron beam was at 25° with respect to the surface normal while the analyzer axis was located along the surface normal (with an acceptance angle of ±6°). At energies of 300 and 500 eV, the elastic-backscattering probability was found to decrease with thickness of the gold overlayer despite the fact that the total elastic-scattering cross section for gold is much larger than that for nickel. At energies of 1000 eV or more, the elastic-backscattering probability increased with overlayer thickness. These experimental results were confirmed in a later work[116] in which the experiment was performed in a slightly different configuration (normal incidence of the primary beam, emission angle of 25°, and an acceptance angle of

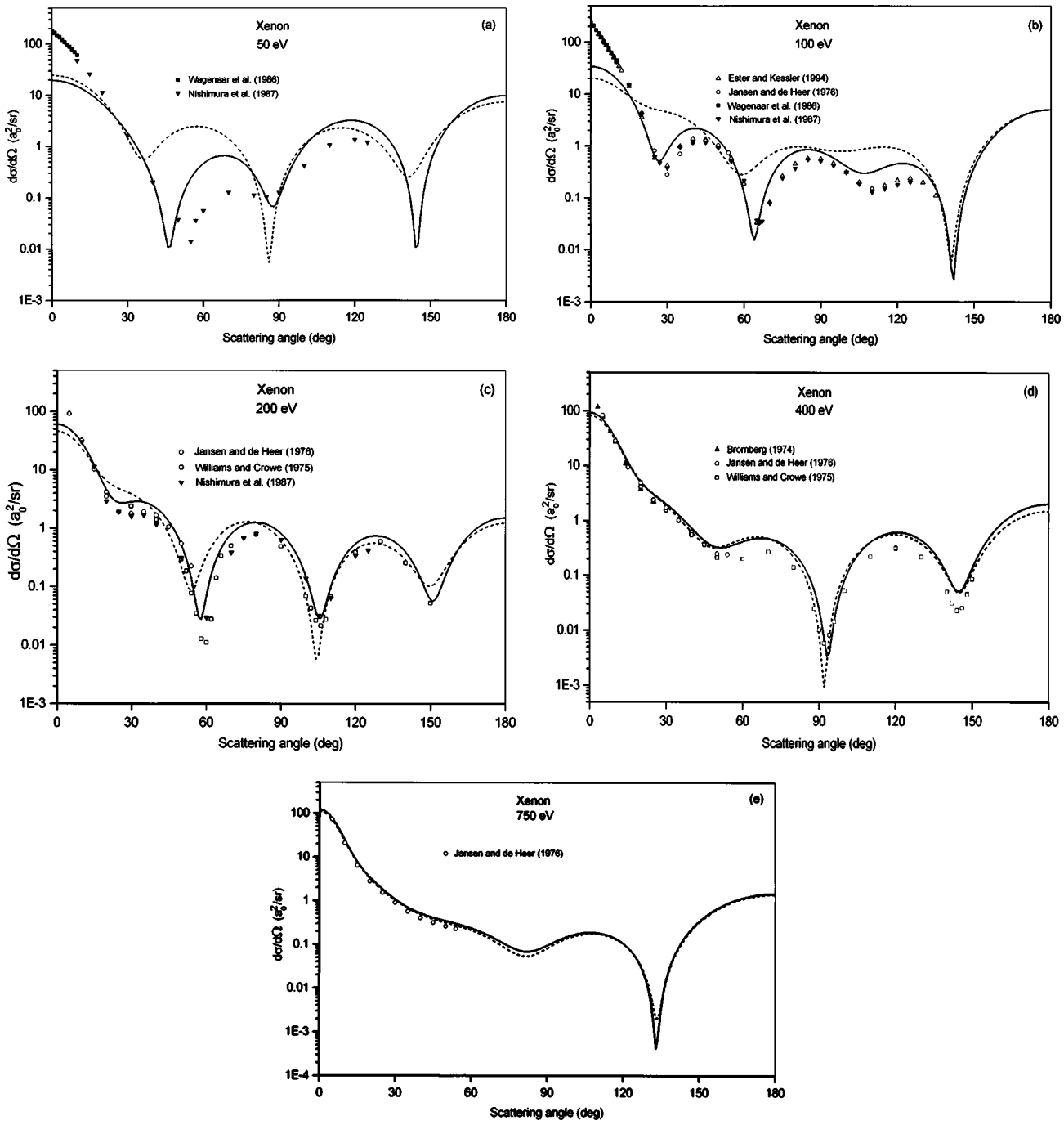

FIG. 21. Comparison of differential elastic-scattering cross sections, $d\sigma/d\Omega$, calculated for xenon for two potentials as a function of scattering angle with measured differential cross sections: (solid line) DHF potential; (dashed line) TFD potential: (a) energy of 50 eV; (b) energy of 100 eV; (c) energy of 200 eV; (d) energy of 400 eV; and (e) energy of 750 eV. The symbols show the measurements of Wagenaar *et al.*,[87] Nishimura *et al.*,[101] Ester and Kessler,[102] Jansen and de Heer,[100] Williams and Crowe,[91] and Bromberg.[81]

$\pm 4°$). These results were in good agreement with Monte Carlo simulations of elastic backscattering that made use of differential elastic-scattering cross sections obtained from the TFD potential. These simulations were performed for the same configurations (incidence angle, emission angle, and acceptance angle) as in the respective experiments. The decrease of the backscattering probability at energies up to 500 eV was ascribed to the presence of a deep minimum located in the DCS for Au at a scattering angle close to 155° [cf. Fig. 6(b)]. For the angular range relevant to these experiments, the DCS for nickel is much larger than that for gold. At higher energies, the minimum in the Au DCS shifts towards smaller scattering angles [cf. Fig. 6(c)], and the DCS for gold is larger than that for nickel.

We have repeated the Monte Carlo calculations for these experiments at energies of 500 and 1000 eV using differen-

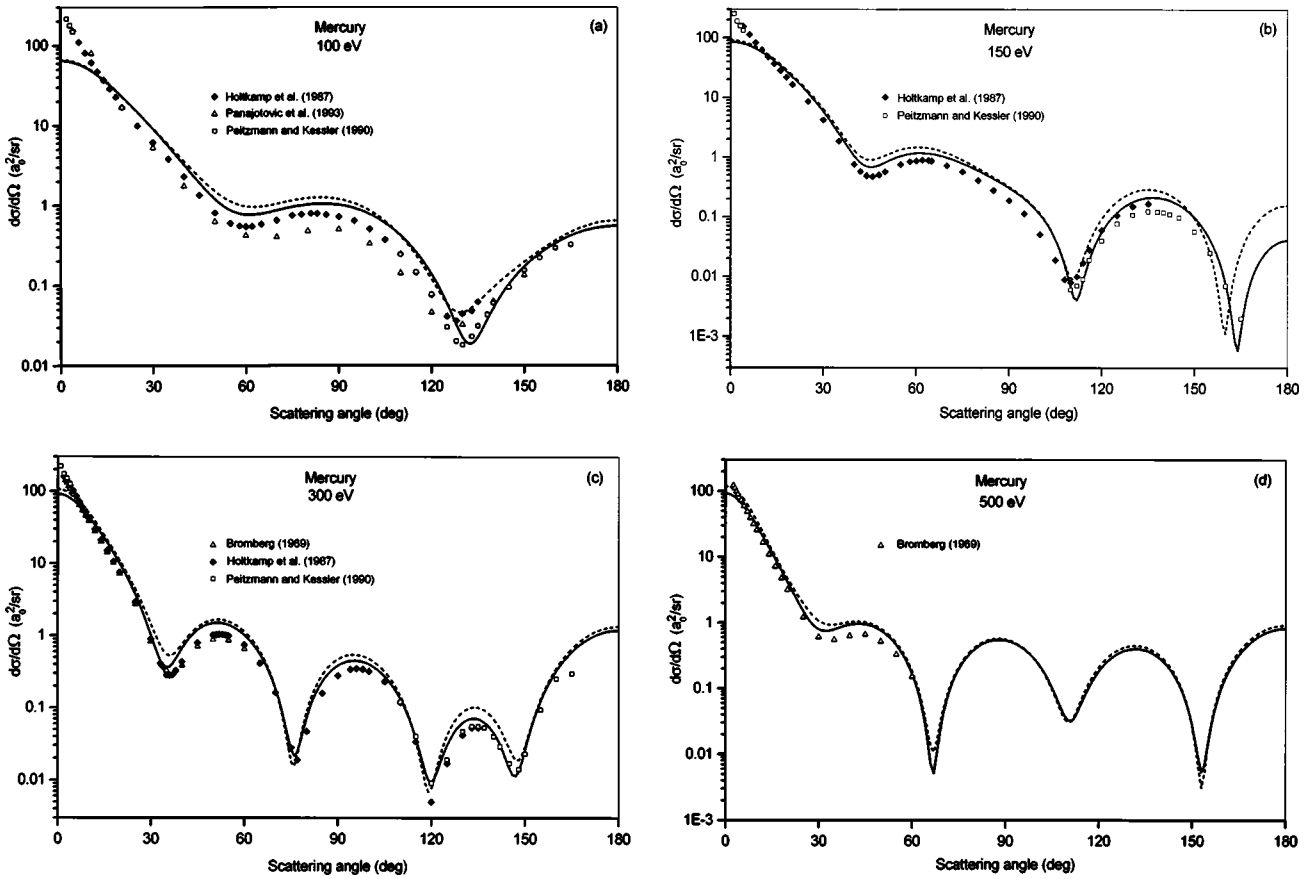

FIG. 22. Comparison of differential elastic-scattering cross sections, $d\sigma/d\Omega$, calculated for mercury for two potentials as a function of scattering angle with measured differential cross sections: (solid line) DHF potential; (dashed line) TFD potential: (a) energy of 100 eV; (b) energy of 150 eV; (c) energy of 300 eV; and (d) energy of 500 eV. The symbols show the measurements of Holtkamp *et al.*,[103] Panajotovic *et al.*,[104] Bromberg,[105] and Peitzmann and Kessler.[106]

tial cross sections for gold and nickel calculated from the DHF potentials for these atoms. We determined the elastic-backscattering probability for an uncovered nickel substrate, $\eta(0)$, and for a gold overlayer with thickness t deposited on nickel, $\eta(t)$. It was convenient to compare values of the ratio, $R(t)$, of elastic-backscattering probabilities

$$R(t)=\frac{\eta(t)}{\eta(0)}, \tag{26}$$

that were obtained from either measured or calculated backscattering data. Figures 25 and 26 show comparisons of measured values of R as a function of Au thickness from Refs. 115 and 116, respectively, with the corresponding values of R determined from Monte Carlo simulations for each experimental configuration and with differential cross sections from each of the two potentials. We see that both cross sections lead to reasonably good agreement with the experimental data. There is a distinct difference, however, between the relative intensities calculated for each potential. In one case, use of differential cross sections from the DHF potential (DCS_{rel}^{DHF}) leads to ratios that are closer to the experimental results while, in other cases, the differential cross sections from the TFD potential (DCS_{rel}^{TFD}) lead to better agreement.

As mentioned above, the experiments reported in Refs. 115 and 116 were performed in slightly different configurations; nevertheless, the experimental ratios differed noticeably (see Figs. 25 and 26). Although the angle between the electron beam and the analyzer axis was the same in both experiments (155°), the location of these directions with respect to the surface was different. The differences between the experimental ratios might also be partially due to systematic errors associated with the different experiments (e.g., accuracy of determining the angles, different sample-preparation procedure, etc.). Finally, the observed differences may result from the different analyzer-acceptance angles. In both experiments, hemispherical electron-energy analyzers (HSAs) were used of different constructions, and these had nominal acceptance angles of ±4° (Ref. 116) or ±6° (Ref. 115). In general, we expect that the measured intensities may depend on the acceptance angle, especially in the vicinity of deep minima in the DCS.

9.2. Electron Inelastic Mean Free Paths Determined by Elastic-Peak Electron Spectroscopy (EPES)

Measurements of elastic-backscattered probabilities, a technique known as elastic-peak electron spectroscopy (EPES), can be used to obtain inelastic mean free paths (IM-

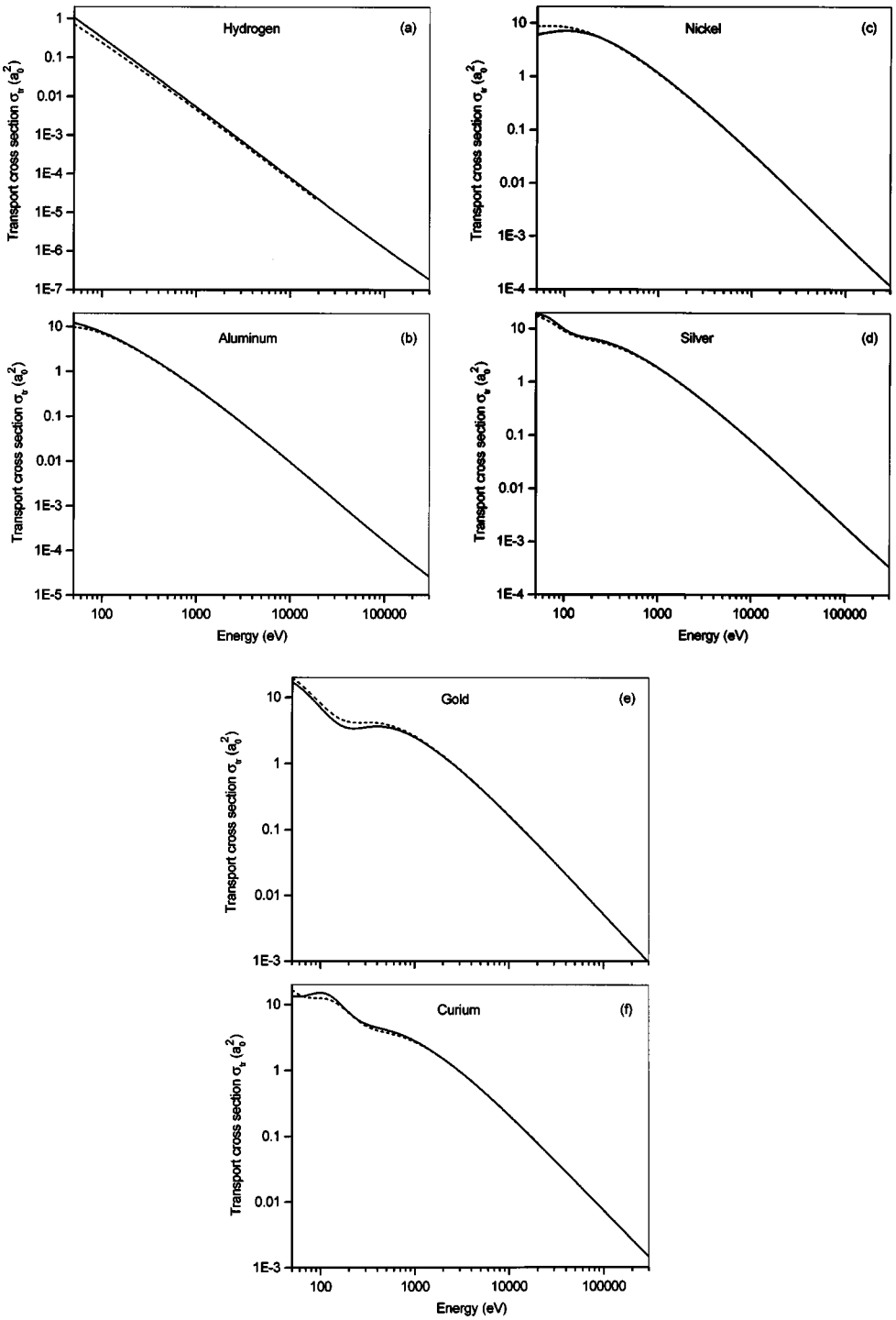

FIG. 23. Energy dependence of the transport cross sections calculated from the TFD and DHF potentials: (solid line) the DHF potential; (dashed line) the TFD potential: (a) hydrogen; (b) aluminum; (c) nickel; (d) silver; (e) gold; and (f) curium.

FPs) at various electron energies.[117] The IMFP is an important parameter that is needed for quantification of surface-analytical techniques such as AES and XPS.[117]

The EPES experiments can be performed in two ways. Most commonly, relative measurements are made of the intensities of electrons backscattered from two surfaces, one the specimen of interest and the other a ''standard'' material for which the IMFP is considered to be sufficiently well known. These measurements are made for the same incident beam energy and current, the same scattering conditions, and the same analyzer conditions. In the other type of EPES experiment, absolute measurements are made of the ratio of the elastically backscattered current to the incident beam current for a selected sample material. No standard material is used. We consider these two types of experiments in Secs. 9.2.1 and 9.2.2, respectively.

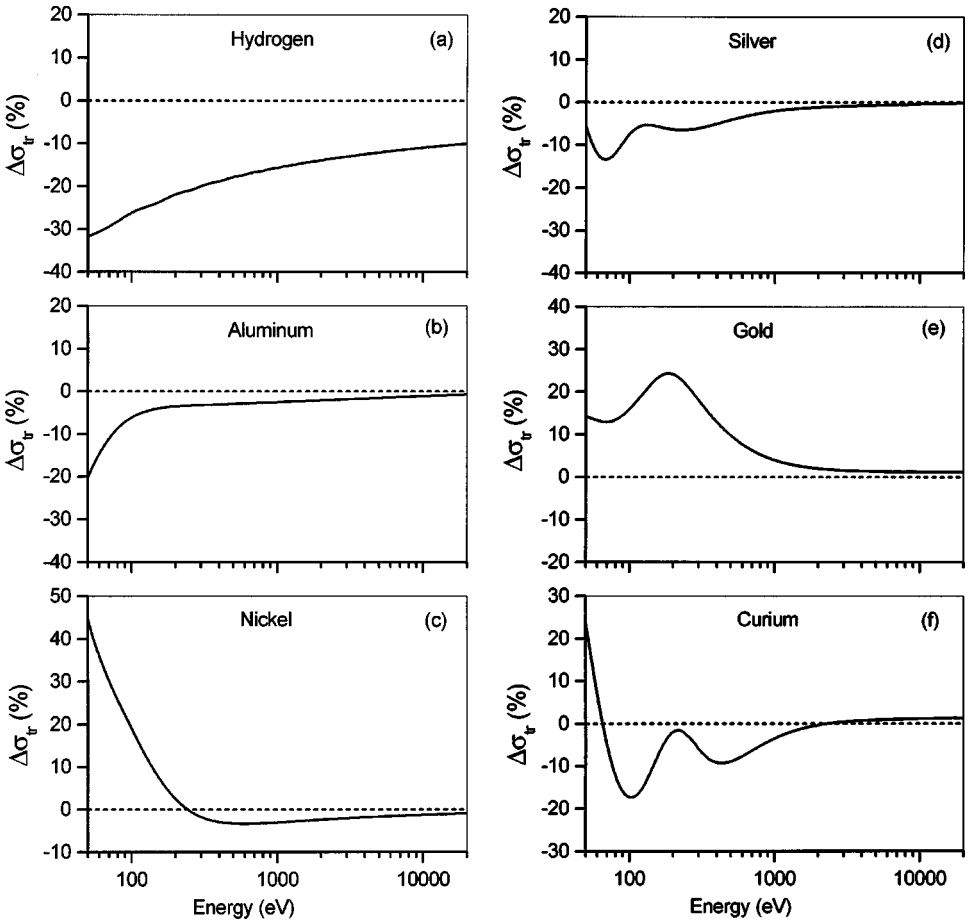

FIG. 24. Energy dependence of percentage differences, $\Delta\sigma_{tr}$, from Eq. (25) between transport cross sections obtained from the TFD and DHF potentials: (a) hydrogen; (b) aluminum; (c) nickel; (d) silver; (e) gold; and (f) curium.

9.2.1. EPES Experiments with a Standard Material

In typical EPES experiments with a standard material, measurements are made of the ratio of the elastic-backscattering probabilities for a sample of interest, η_{sample}, and for a selected standard material, η_{standard}, with a ''known'' IMFP. Four elemental solids were recommended in a previous analysis as suitable standards: Ni, Cu, Ag, and Au.[117] The same ratio is calculated from a suitable theoretical model describing the backscattering phenomenon. Monte Carlo simulations of electron backscattering are usually made for this purpose, and DCS values are required for the sample and standard materials at the electron energies of interest. Simulations are performed at a particular electron energy for different assumed values of the IMFP for the sample, and a so-called calibration curve is produced in which the ratio of elastic-backscattering probabilities is given as a function of the sample IMFP. The measured ratio can then be used to determine the sample IMFP.

To determine experimentally the ratio of elastic-backscattering probabilities, one does not need to measure their absolute values. It is sufficient to measure elastic-peak intensities for the sample and standard in the energy distributions of backscattered electrons, I_{sample} and I_{standard}, respectively. We then have the ratio of interest, R_{sample}

$$R_{\text{sample}}=\frac{\eta_{\text{sample}}}{\eta_{\text{standard}}}=\frac{I_{\text{sample}}}{I_{\text{standard}}}. \tag{27}$$

We showed in Sec. 7.2 that DCS values from the TFD and DHF potentials can differ considerably at scattering angles close to those where deep minima occur in the DCSs. We therefore now consider a ''worst-case'' situation in which an EPES experiment is performed with a material, electron energy, and experimental configuration for which there is a deep minimum in the DCS (for a single elastic-scattering event). Figure 27 shows the large-scattering-angle region of

TABLE 3. Values of transport cross sections, σ_{tr}^{m}, derived from measured differential cross sections for He and Hg at energies of 50 and 100 eV and the corresponding calculated transport cross sections, σ_{tr}^{TFD} and σ_{tr}^{DHF}, obtained from Refs. 10 and 12 with use of the TFD and DHF potentials, respectively

Atom	Energy (eV)	σ_{tr}^{m} (a_0^2)	Ref.	σ_{tr}^{TFD} (a_0^2)	σ_{tr}^{DHF} (a_0^2)
He	50	2.51	86	2.45	2.77
	50	3.32	88	2.45	2.77
	100	0.754	86	0.834	0.928
Hg	50	12.3	104	20.4	18.4
	100	4.29	104	8.70	7.70

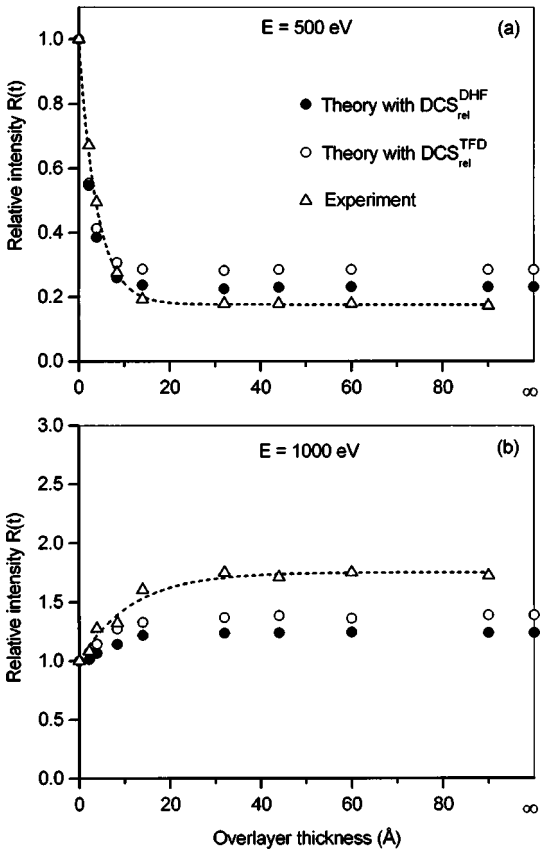

FIG. 25. Relative intensity of electrons elastically backscattered from a gold overlayer on Ni, $R(t)$ defined by Eq. (26), as a function of overlayer thickness at energies of: (a) 500 eV and (b) 1000 eV: (triangles and dashed line) experimental data taken from Jablonski *et al.*[115]; results of Monte Carlo simulations for the same configuration as used in Jablonski *et al.*[115] with elastic-scattering cross sections calculated from the TFD potential (open circles) and from the DHF potential (filled circles).

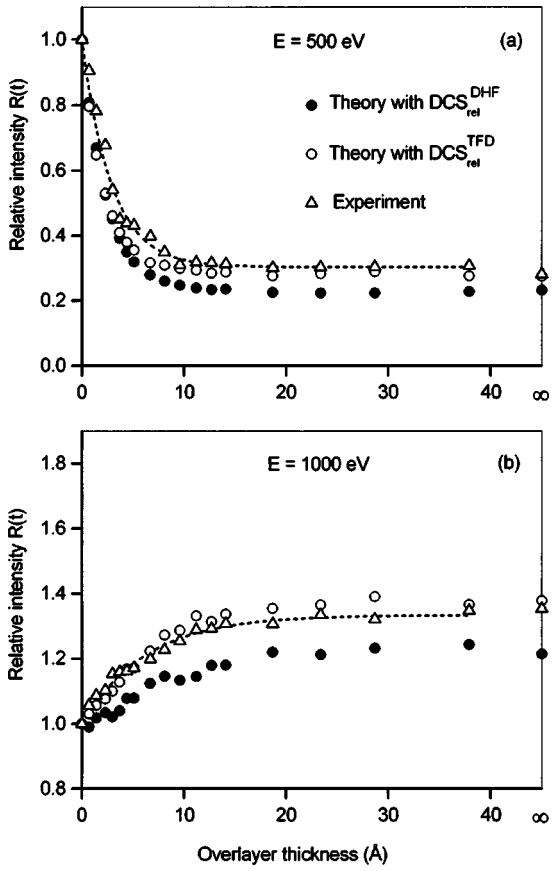

FIG. 26. Relative intensity of electrons elastically backscattered from a gold overlayer on Ni, $R(t)$ defined by Eq. (26), as a function of overlayer thickness at energies of: (a) 500 eV and (b) 1000 eV: (triangles and dashed line) experimental data from Jablonski *et al.*[116]; results of Monte Carlo simulations for the same configuration as used in Jablonski *et al.*[116] with elastic-scattering cross sections calculated from the TFD potential (open circles) and from the DHF potential (filled circles).

the DCS for gold at energies of 500 and 1000 eV. The vertical line with the acronym HSA indicates the average scattering angle in the experiments of Jablonski *et al.*[115,116] As discussed in Sec. 9.1, a deep minimum in the DCS occurs for gold at 500 eV in the vicinity of a scattering angle of 155°, and there are appreciable differences in the DCS values from the TFD and DHF potentials [cf. Fig. 12(b)]; smaller differences near this scattering angle occur at 1000 eV.

For an EPES experiment with normal incidence of the primary electron beam and a mean emission angle of 25°, the average scattering angle will be 155°. Calibration curves for a gold sample and a nickel standard (i.e., $R_{Au}=I_{Au}/I_{Ni}$ as a function of the IMFP assumed for Au) calculated for this configuration and for electron energies of 500 and 1000 eV are shown in Fig. 28. In these calculations, we assumed that the acceptance angle was equal to $\pm 4°$ which is typical for hemispherical analyzers.[116] We see that the calibration curves derived from DCS values that were obtained from the TFD and DHF potentials differ considerably, particularly at 500 eV. Such differences will clearly lead to different IMFP values. Suppose, for example, that R_{Au} is measured to be 0.2325 at 500 eV and 1.226 at 1000 eV (these values correspond to the recommended IMFPs for gold of 8.36 and 13.78 Å at these energies, respectively[117]). The calibration curve in Fig. 28 calculated with DCSs from the TDF potential leads to smaller IMFPs for Au, 6.93 and 12.13 Å at energies of 500 and 1000 eV, respectively. We calculate the percentage difference $\Delta\lambda$

$$\Delta\lambda = 100(\lambda_{in}^{TFD}-\lambda_{in}^{DHF})/\lambda_{in}^{DHF} \qquad (28)$$

from the IMFPs, λ_{in}^{TFD} and λ_{in}^{DHF}, derived from calibration curves calculated using DCSs obtained from the TFD and DHF potentials, respectively. The resulting values of $\Delta\lambda$ from Eq. (28) are -17.1% and -12.0% at 500 and 1000 eV, respectively. This "worst-case" example illustrates that a significant systematic error can arise in IMFPs determined by EPES with DCS values from the TFD potential for materials (in this case, Au), electron energies (in this case, 500 eV), and measurement configuration (in this case, a scattering angle of 155°) such that there is a deep minimum in the DCS. Although a measurement with this configuration for Au at 1000 eV would not occur near a deep minimum in the DCS, there is an error of 12.0% in IMFPs determined from the calibration curve derived with use of DCSs from the TFD

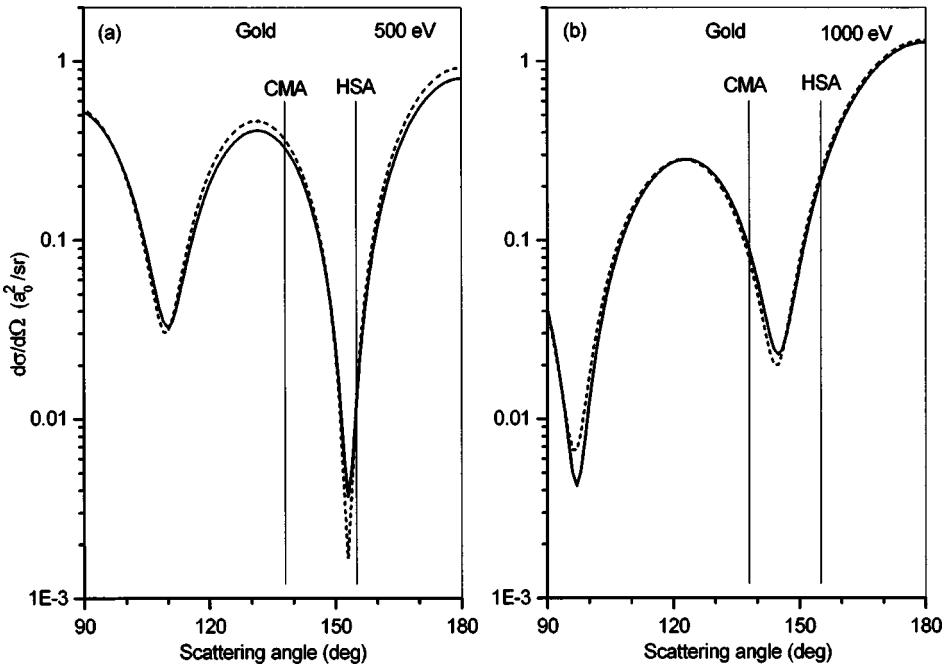

FIG. 27. Differential elastic-scattering cross sections, $d\sigma/d\Omega$, calculated for gold from the TFD and DHF potentials at scattering angles exceeding 90°: (solid line) DHF potential; (dashed line) TFD potential: (a) energy of 500 eV; (b) energy of 1000 eV. Vertical line with the acronym HSA indicates the average scattering angle for the experiments of Jablonski *et al.* (Refs. 115 and 116) and the vertical line with the acronym CMA shows the average scattering angle for the experiments of Krawczyk *et al.*[118]

potential. This systematic error arises in part from a positive error in the DCS for Au [cf. Fig. 12(c)] and in part from a negative error in the DCS for Ni [cf. Fig. 10(c)] at the scattering angle of 155°.

We consider now the determination of IMFPs by EPES with a cylindrical-mirror analyzer, the instrument that has been most frequently used in the work discussed in a recent review.[117] In this configuration, the primary electrons are incident on the surface along the normal, and the average emission angle is equal to 42.3°. For the case of Au with this configuration, EPES measurements at 500 eV would be well removed from deep minima in the DCS for Au while measurements at 1000 eV would be closer to a deep minimum (cf. Fig. 27). No minima are observed in the DCS for Cu at the considered energies in the relevant angular range. EPES measurements of AuCu alloys with a CMA and an Au standard have been reported recently by Krawczyk *et al.*[118] As an example, we consider the case of the $Au_{50}Cu_{50}$ alloy. Figure 29 shows calibration curves for four electron energies between 200 and 2000 eV for the conditions of the Krawczyk *et al.* experiments. These calibration curves were calculated assuming the same acceptance angle as for the analyzer in the experiments, i.e. ±6°. The differences between the calibration curves found using DCSs with the TFD and DHF potentials in Fig. 29 are much less than the corresponding differences in Fig. 28.

We quantify the differences between the calibration curves in Fig. 29 by defining the percentage difference ΔR_{AuCu}

$$\Delta R_{\mathrm{AuCu}} = 100(R_{\mathrm{AuCu}}^{\mathrm{TFD}} - R_{\mathrm{AuCu}}^{\mathrm{DHF}})/R_{\mathrm{AuCu}}^{\mathrm{DHF}}, \qquad (29)$$

where $R_{\mathrm{AuCu}}^{\mathrm{TFD}}$ and $R_{\mathrm{AuCu}}^{\mathrm{DHF}}$ are the values of R_{AuCu} for the TFD and DHF potentials, respectively. Values of ΔR_{AuCu} are plotted in Fig. 30 as a function of the assumed IMFP values. We see that ΔR_{AuCu} is practically always less than 10%. At 2000 eV, the percentage differences decrease to less than 5%. To determine an IMFP in the alloy, we need only a fragment of the calibration curve corresponding to measured ratios, R_{AuCu}, for particular energies.[118] These ratios and the corresponding IMFPs are listed in Table 4 for DCSs obtained from the TFD and DHF potentials. As one can see, the change of potential leads to changes in the derived IMFPs of less than 6% at energies of 200 and 500 eV. At higher energies, the changes in the derived IMFPs decrease from 3.26% at 1000 eV to 1.27% at 2000 eV. The latter change is comparable to the precision of our Monte Carlo calculations.

9.2.2. EPES Experiments without a Standard Material

We consider now EPES experiments in which a standard material is not used.[117] Measurements are made of the ratio, η_{sample}, of the elastically backscattered current, I_{sample}, in a particular solid angle (for the material and electron energy of interest) to the current of the incident beam, I_{beam}. Such experiments are more demanding than the relative measurements described in Sec. 9.2.1 because each of the currents, I_{sample} and I_{beam}, has to be measured absolutely. Monte Carlo simulations are made for the particular experimental conditions to produce calibration curves showing η_{sample} as a function of assumed values for the sample IMFP. The IMFP can then be determined from the calibration curve as the value that gives the same value of η_{sample} as that measured.

As an example, Fig. 31 shows EPES calibration curves for gold in the form of plots of the calculated elastic-backscattering probabilities, η_{Au}, as a function of assumed IMFP for normal incidence of an electron beam in a retarding-field analyzer for emission angles between 5° and 55° at electron energies of 500 eV and 1 keV. This configuration was selected to correspond to some absolute EPES

measurements.[118,119] The calibration curves of Fig. 31 were obtained, as for Fig. 28, from Monte Carlo simulations in which DCSs from the TFD potential (dashed line) and the DHF potential (solid line) were utilized. The marked ordinate values, 0.036 01 at 500 eV and 0.053 23 at 1 keV, are values of η_{Au} obtained from the simulations with DCSs from the DHF potential and the recommended IMFPs for Au of 8.36 and 13.78 Å, respectively.[117] The IMFPs derived from the calibration curves for the TFD potential for these values of η_{Au} are 7.52 and 13.60 Å, respectively. Values of $\Delta\lambda$ from Eq. (28) are -10.0% and -1.31%, respectively.

As another example, we consider the absolute EPES experiments of Dolinski *et al.* made for Cu in which the surfaces were cleaned by concurrent K^+ bombardment and heating to remove K from the surface.[120] These measurements were made with normal incidence of the primary beam and a RFA for which the range of accepted emission angles was between 5° and 44°. Table 5 shows IMFPs obtained from the experiments of Dolinski *et al.* and from DCSs calculated from the TFD and DHF potentials for energies between 250 and 1500 eV and the percentage differences between these IMFPs from Eq. (28). These percentage differences range between 2.36% at 250 eV to 6.42% at 500 eV. Table 4 also shows IMFP values, λ_{in}^{HFS}, obtained by Dolinski *et al.* using the DCSs from a relativistic Hartree–Fock–Slater potential of Fink and Ingram.[2]

9.3. Mean Escape Depths for AES and XPS

The mean escape depth (MED) is a useful parameter in AES and XPS. This parameter specifies the average depth, normal to the surface, from which signal electrons are emitted. The MED, D, is defined by[121]

$$D=\frac{\int_0^\infty z\,\phi(z,\alpha)\,dz}{\int_0^\infty \phi(z,\alpha)\,dz}, \tag{30}$$

where $\phi(z,\alpha)$ is the emission depth distribution function defined as the probability that the particle leaving the surface in a given direction originated from a specified depth measured normally from the surface into the material.[121]

The following analytical expression for the MED of signal electrons in AES and XPS has been derived by Jablonski *et al.*[31] from a solution of the kinetic Boltzmann equation within the so-called transport approximation

$$D=\frac{\lambda_{in}\lambda_{tr}}{\lambda_{in}+\lambda_{tr}}\left(\cos\alpha+\frac{S_1}{S_2}\right), \tag{31}$$

where

$$S_1=(1-\omega)^{-1/2}\chi+C_1, \tag{32}$$

$$S_2=(1-\omega)^{-1/2}-\frac{(\beta/4)(3\cos^2\psi-1)}{H(\cos\alpha,\omega)}+C_2, \tag{33}$$

$$\chi=(\omega/2)(1-\omega)^{-1/2}\int_0^1 \cos\alpha H(\cos\alpha,\omega)\,d(\cos\alpha), \tag{34}$$

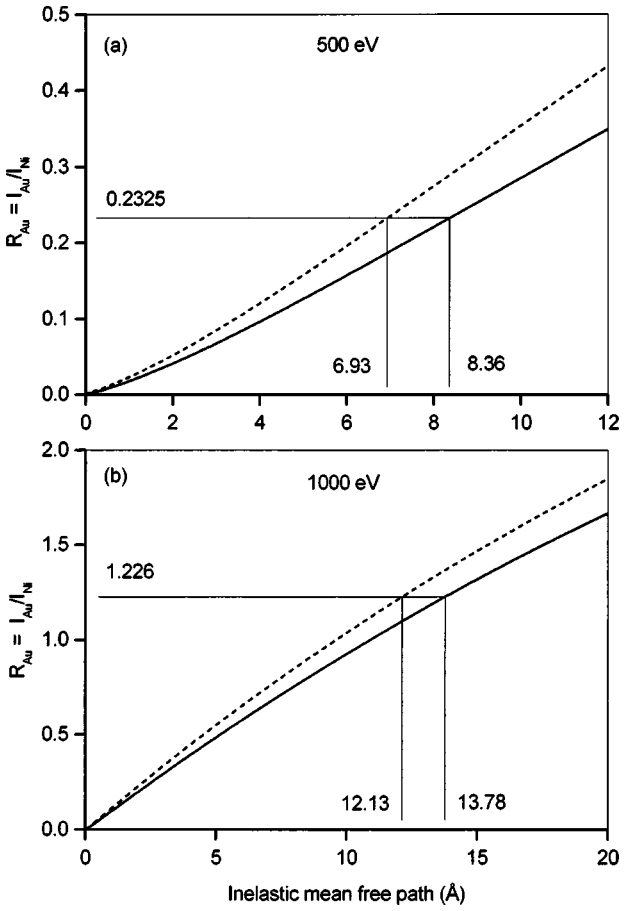

FIG. 28. Ratio of elastic-backscattering probabilities $R_{Au}=I_{Au}/I_{Ni}$ defined by Eq. (27) as a function of assumed values of the electron inelastic mean free path for gold. Two calibration curves for EPES experiments are shown based on Monte Carlo simulations with DCS values obtained from TFD and DHF potentials: (solid line) DCS calculated from the DHF potential; (dashed line) DCS calculated from the TFD potential: (a) energy of 500 eV and (b) energy of 1000 eV. The calibration curves were calculated for the experimental configuration of Jablonski *et al.*[115,116] who used a hemispherical analyzer for their measurements.

$$C_1=-\frac{\omega\beta}{16}(3\cos^2\theta-1)\times\int_0^1\frac{(x^2+x\cos\alpha)(3x^2-1)H(x,\omega)}{x+\cos\alpha}\,dx, \tag{35}$$

$$C_2=\frac{\omega\beta}{16}(3\cos^2\theta-1)\int_0^1\frac{x(3x^2-1)H(x,\omega)}{x+\cos\alpha}\,dx. \tag{36}$$

In Eqs. (31)–(36), λ_{tr} is the transport mean free path, α is the electron emission angle with respect to the surface normal, θ is the angle between the x-ray direction and the surface normal in XPS, ψ is the angle between the direction of x rays and the analyzer axis in XPS, β is the photoionization asymmetry parameter in XPS, ω is the single-scattering albedo given by $\omega=\lambda_{in}/(\lambda_{in}+\lambda_{tr})$, and $H(x,\omega)$ is the Chandrasekhar function.[122] The transport mean free path is obtained from the transport cross section

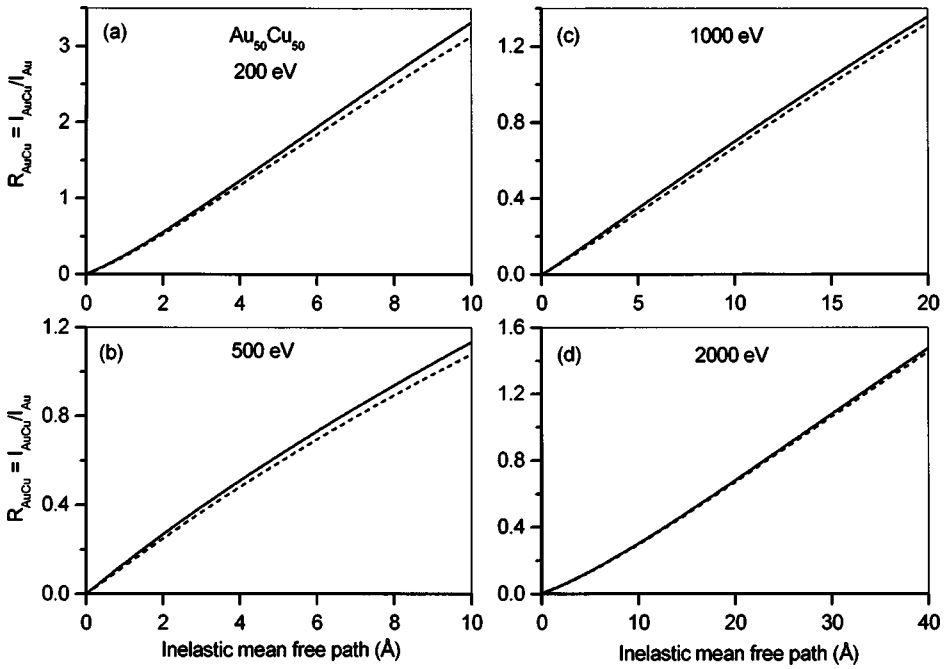

FIG. 29. Ratio of elastic-backscattering probabilities $R_{AuCu} = I_{AuCu}/I_{Au}$ defined by Eq. (27) as a function of assumed values of the electron inelastic mean free path for the alloy $Au_{50}Cu_{50}$. Two calibration curves for EPES experiments are shown based on Monte Carlo simulations with DCS values obtained from TFD and DHF potentials: (solid line) DCS calculated from the DHF potential; (dashed line) DCS calculated from the TFD potential: (a) energy of 200 eV; (b) energy of 500 eV; (c) energy of 1000 eV; and (d) energy of 2000 eV. The calibration curves were calculated for the experimental configuration of Krawczyk *et al.*[118] who used a cylindrical-mirror analyzer for their measurements.

$$\lambda_{tr} = \frac{1}{N\sigma_{tr}}, \tag{37}$$

where N is the atomic density, i.e., the number of atoms per unit volume. For AES, the emission of Auger electrons from atoms is close to isotropic for amorphous and polycrystalline solids, and $\beta = 0$. The MED from Eqs. (31)–(36) then becomes

$$D = \lambda_{in}\lambda_{tr}(\chi + \cos\alpha)/(\lambda_{in} + \lambda_{tr}). \tag{38}$$

It has been shown that the parameters C_1 and C_2 in Eqs. (32) and (33) are small compared to S_1 and S_2, respectively, and can be neglected for typical photoelectron lines in XPS.[31] The change in the MED values, due to the assumption that C_1 and C_2 are equal to zero, usually does not exceed 5%. This assumption has been made in the present MED calculations.

We consider now changes in MED values from Eqs. (31)–(38) arising from the use of transport cross sections in Eq. (37) that were computed from Eq. (20) using DCS values obtained from the TFD and DHF potentials. Calculations were made for four electron energies in gold corresponding to two Auger-electron lines (Au N_7VV and Au $M_5N_{67}N_{67}$)

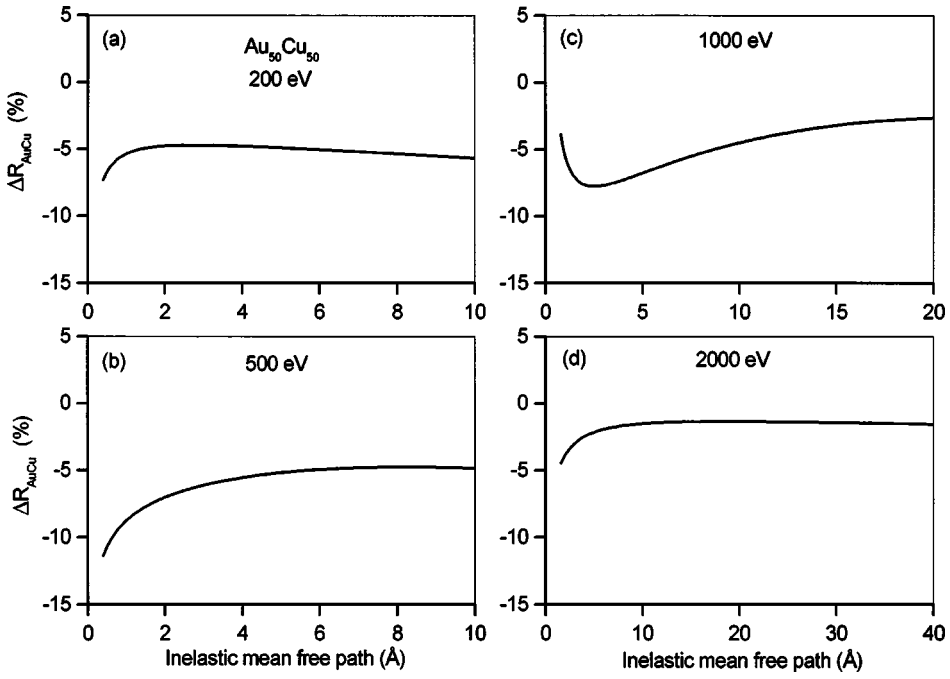

FIG. 30. Percentage differences, ΔR_{AuCu}, calculated from Eq. (29) between the calibration curves of Fig. 29 for the TFD and DHF potentials as a function of assumed values of the electron inelastic mean free path for the alloy $Au_{50}Cu_{50}$.

TABLE 4. IMFP values for the alloy $Au_{50}Cu_{50}$ derived from calibration curves for the EPES experiments of Krawczyk *et al.*[118] that were calculated using DCSs obtained from the TFD potential (λ_{in}^{TFD}) and the DHF potential (λ_{in}^{DHF}) at the indicated energies from the measured ratios, I_{AuCu}/I_{Au}, of elastic-backscattered intensities. The percentage differences in the derived IMFPs, $\Delta\lambda$, from Eq. (28) are shown in the final column.

E (eV)	I_{AuCu}/I_{Au}	λ_{in}^{TFD} (Å)	λ_{in}^{DHF} (Å)	$\Delta\lambda$ (%)
200	2.144	6.91	6.58	5.02
500	0.881	7.86	7.43	5.79
1000	1.081	16.17	15.66	3.26
1500	1.078	22.10	21.48	2.89
2000	0.859	24.78	24.47	1.27

and two photoelectron lines ($Au\,4s$ and $Au\,4f_{7/2}$) for XPS with Mg $K\alpha$ x rays. These energies cover a wide range (from 70 to 2016 eV). In these calculations, we selected a representative value[123] of the angle $\psi=54°$ and determined D for variations of the electron emission angle, α, from 0° to 80°. The variation of α corresponds to rotation of the sample in a chamber with fixed positions of the analyzer and the x-ray source (for XPS).

The transport mean free path is the only parameter in Eqs. (31)–(38) describing the strength of elastic-scattering effects in a given solid. If the transport mean free path reaches infinity, the MED approaches the value determined from the so-called common formalism of AES and XPS in which elastic–electron collisions in the solid are neglected. If we denote the MED for this case by Δ, then Eq. (31) becomes

$$\Delta=\lambda_{in}\cos\alpha. \tag{39}$$

To examine the effects of elastic scattering on D, it is convenient to determine the ratio, R_{MED}

$$R_{MED}=D/\Delta. \tag{40}$$

Figure 32 shows plots of R_{MED} calculated from values of D for the TFD and DHF potentials as a function of α for the four selected photoelectron and Auger-electron lines in gold. We see that the MED values derived from the two potentials are very similar. The differences between the D values seem to decrease with increasing emission angle and with increasing energy. The latter effect can be ascribed to the decreasing differences between transport cross sections in Au for the two potentials with increasing energy [cf. Fig. 24(e)]. To quantify the difference between the MEDs from the two potentials, we calculate the percentage difference, ΔD

$$\Delta D=100(D_{TFD}-D_{DHF})/D_{DHF}, \tag{41}$$

where D_{TFD} and D_{DHF} are the MEDs determined using transport cross sections from the TFD and DHF potentials, respectively. Values of ΔD for the Auger-electron and photoelectron lines in Fig. 32 are plotted as a function of emission angle in Fig. 33. As one can see, the values of ΔD at normal emission vary from 4.3% at 70 eV to about 0.5% at 2016 eV, and become smaller with increasing emission angle. Since elastic-scattering effects (as judged by the value of ω) are strong in gold,[124] we conclude that the change of potential will not significantly affect MED values of other elements at energies typical for AES and XPS.

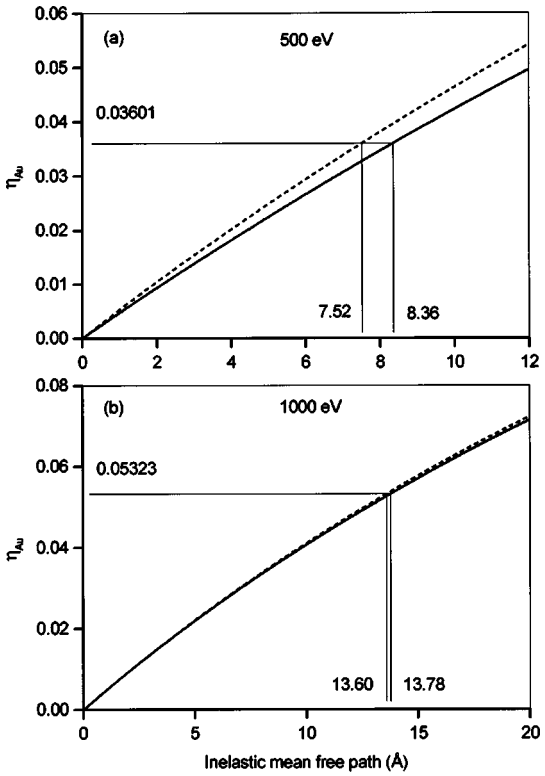

FIG. 31. Plot of the elastic-backscattering probability, η_{Au}, for gold as a function of assumed values of the electron inelastic mean free path for normal incidence of the electron beam and a retarding-field analyzer accepting emission angles between 5° and 55°. Two calibration curves for EPES experiments are shown based on Monte Carlo simulations with DCS values obtained from TFD and DHF potentials: (solid line) DCS calculated from the DHF potential; (dashed line) DCS calculated from the TFD potential: (a) energy of 500 eV and (b) energy of 1000 eV.

10. Validity of Calculated DCS Data for Atoms in Simulations of Electron Transport in Solids

Calculated DCSs for atoms have been extensively used in simulations of electron transport in solids[13–45] as well as in the three examples discussed in Sec. 9. The electron energies in these particular applications have typically been between 100 eV and 25 keV although similar simulations have been made for higher energies. The atomic data have been utilized because calculated DCSs are available[1–12] for all elements and a wide range of electron energies, whereas measured DCSs exist for a very limited number of elements and energies (such as those presented in Sec. 7.4).

We discuss here the validity of the atomic DCS data in descriptions of electron transport in solids. The interaction potential in a solid will clearly be different from that for a free atom. These differences are expected to have a considerable effect on the DCSs for ''small-angle'' scattering. Fortunately, for many problems of practical interest, the ''large-

TABLE 5. IMFP values for copper derived from the absolute EPES experiments of Dolinski *et al.*[120] that were calculated using DCSs obtained from the TFD potential (λ_{in}^{TFD}) and the DHF potential (λ_{in}^{DHF}) at the indicated energies, E, from the measured elastic-backscattering probabilities, η_{Cu}. The percentage differences in the derived IMFPs, $\Delta\lambda$, from Eq. (28) are shown in the final column. The third column shows the IMFPs reported by Dolinski *et al.*, λ_{in}^{HFS}, from calibration curves obtained with DCSs computed from a relativistic Hartree–Fock–Slater potential by Fink and Ingram.[2]

E (eV)	η_{Cu}	λ_{in}^{HFS} (Å)	λ_{in}^{TFD} (Å)	λ_{in}^{DHF} (Å)	$\Delta\lambda$ (%)
250	0.0434	4.2	3.47	3.39	2.36
500	0.0395	5.9	6.10	5.45	6.42
1000	0.0229	11.2	11.77	11.14	5.66
1500	0.0149	17.0	17.23	16.74	2.93

angle'' scattering is generally more relevant than the small-angle scattering. The atomic potential can be matched to a muffin-tin potential for the corresponding solid or can be empirically truncated in the solid.[125] While the resulting potentials lead to substantial differences in the DCSs from the atomic DCSs for small-angle scattering (with the differences depending on Z),[11] there are often only small effects on parameters such as transport cross sections, effective attenuation lengths (EALs), and backscattering factors.[6,11,38] For example, Berger and Seltzer[11] report that transport cross sections for solid Au (calculated with the Raith[125] method of potential truncation) differ from those for atomic Au by less than 0.1% for energies between 1 and 500 keV, while the similar differences in transport cross sections for Be are less than 3.3% for the same energy range. Cumpson and Seah[38] show that the differences between EALs obtained from a TF/muffin-tin potential for 18 solid elements and those from the corresponding atomic relativistic HFS potentials could be characterized by a standard deviation of 2.5% at 200 eV and of 1.5% at 1 keV. Similarly, as shown in Sec. 9 and elsewhere,[33] elastic-backscattering probabilities, IMFPs, MEDs, and XPS signal intensities calculated for solids from TFD and DHF or similar atomic potentials generally differ by less than 10% and often less than 5%. These uncertainties are generally small compared to other sources of uncertainty in many applications.

We come now to an apparently more serious problem. We have shown in Sec. 7.4 that measured DCSs for Ar agree well with DCSs calculated from the DHF potential for electron energies of 1 keV and above. Similar results have been found for He, Ne, Kr, and Xe.[11] At lower energies, however, there can be differences (away from deep minima) of often up to a factor of 2 and occasionally by a larger factor, as shown in Figs. 17–22. As noted in Sec. 7.4, these differences can be explained by the neglect of absorption and polarizability corrections in most DCS calculations. The eikonal method takes these corrections into account, and improved agreement is found between the resulting calculated DCSs for He and Ar and those measured.[107]

Figures 17–22 suggest that while atomic DCSs calculated from the DHF potential should be useful for applications at electron energies of 1 keV and above, there could be systematic errors at lower energies. Nevertheless, a large body of literature[13–45,117] indicates that atomic DCSs have been successfully used at these low energies for solids.

As an example, we now examine the use of calculated atomic DCSs for the determination of IMFPs by the EPES method. As discussed in Sec. 9.2, IMFPs can be determined from relative or absolute measurements of elastic-backscattered intensities. The IMFPs obtained from relative measurements should not be affected appreciably by systematic error in the calculated DCSs because, in effect, ratios of DCSs for two solids are employed (unless, of course, the systematic error in the DCS for one material was much greater than the systematic error for the other). In contrast, IMFPs derived from absolute measurements will have systematic errors comparable to the systematic errors in the corresponding DCSs. Comparisons of IMFPs from absolute EPES measurements with IMFPs calculated from experimental optical data for six elemental solids (Al, Si, Ni, Cu, Ag, and Au) as a function of electron energy between 150 eV and 2 keV do not show clear trends.[117] For two elements (Cu and Au), the IMFPs from the EPES measurements are lower than the calculated IMFPs for energies less than 700 eV by up to about 40%; for Ag, however, the EPES IMFPs are larger than the calculated IMFPs by up to about 17% in the same energy range. These results could possibly be due to systematic errors associated with the use of atomic DCSs for each solid. It is also possible that the results could be due to random errors associated with varying strengths of surface electronic excitations for different experimental configurations and with changes of EPES intensities with different surface roughnesses.[117] The latter effects would be expected to become larger with decreasing electron energy, and would be more significant for more grazing angles of electron incidence or emission. Further experiments are clearly needed to define the magnitudes of these effects and to clarify the magnitude of any differences between IMFPs obtained from absolute EPES experiments and calculated IMFPs.

We point out that IMFPs calculated from experimental optical data[117] have been tested experimentally in at least three independent ways. First, Seah *et al.*[126] analyzed the signal intensities of photoelectron and Auger-electron lines of some 60 elemental solids and found that these were consistent with predicted intensities within a standard uncertainty of about 28% for lines with energies greater than 180 eV. Their comparison, based on data not only for IMFPs but also for excitation cross sections and backscattering factors (for AES), did not show energy-dependent systematic deviations for energies less than 1 keV that could be associated with possible energy-dependent errors of the IMFP predictive equation TPP-2M[127] that was used in the analysis. Second, EALs derived from IMFPs have been extensively used for determination of overlayer-film thicknesses by AES and XPS.[72] Computed EALs for SiO_2, for example, agree within 10% with the average of those determined experimentally.[128] Finally, Rundgren[129] compared current–voltage curves from low-energy electron diffraction experiments for the Cu(111) sur-

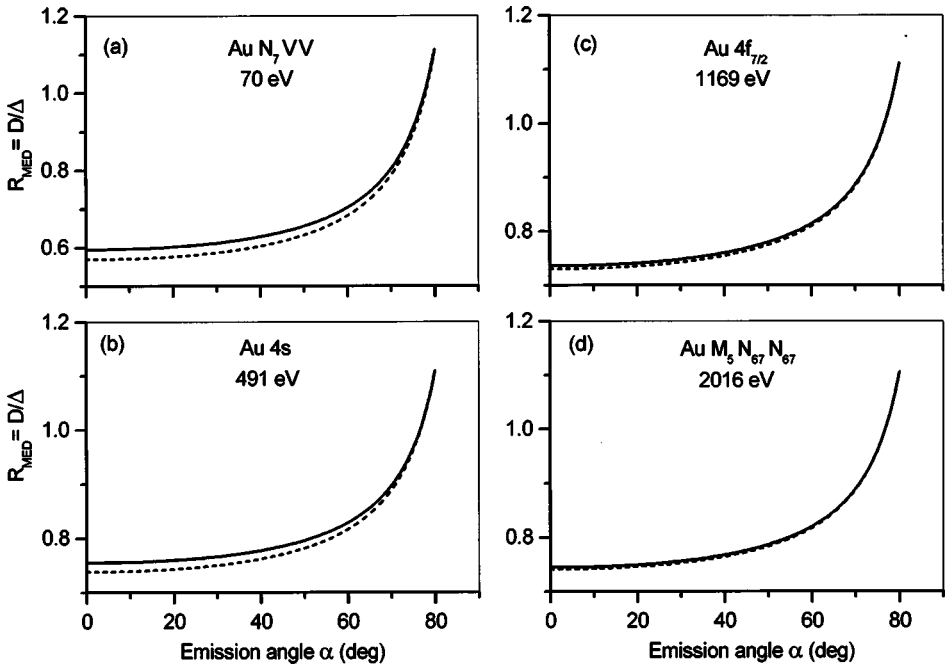

FIG. 32. Ratio of the mean escape depth, D, from Eqs. (31)–(38) to the mean escape depth, Δ, calculated with neglect of elastic scattering for two photoelectron lines and two Auger-electron lines in gold as a function of the emission angle, α: (solid line) D obtained from transport cross sections calculated with the DHF potential; (dashed line) D obtained from transport cross sections calculated with the TFD potential: (a) Au N_7VV Auger electrons; (b) Au $4s$ photoelectrons excited by Mg $K\alpha$ radiation; (c) Au $4f_{7/2}$ photoelectrons excited by Mg $K\alpha$ radiation; and (d) Au $M_5N_{67}N_{67}$ Auger electrons.

face with calculated curves in which an energy-dependent imaginary potential was used to represent the inelastic scattering. This imaginary potential was derived from Cu IMFPs computed from experimental optical data.[130] There was excellent agreement in the widths of the diffraction peaks for energies between 40 and 190 eV.

We therefore conclude that the IMFPs determined from absolute EPES experiments are unlikely to have a systematic error of as much as a factor of 2 for electron energies between 150 eV and 1 keV. While measured DCSs in this energy range for the rare gases in Figs. 17–21 can deviate by up to factor of 2 from DCSs calculated from the DHF potential, these computed DCSs seem to provide reliable IMFPs from absolute EPES experiments. It is possible that the deviations found in Figs. 17–21 for the rare gases might be much larger than those for other atoms, although we do not know of any reason to support this speculation. Nevertheless, we point out that the deviations for Hg in Fig. 22 appear to be less than those for the rare gases at similar energies. We also suggest that the absorption correction to the DCSs calculated from the DHF potential might be less for a solid than the corresponding atom. Tanuma *et al.*[131] showed that the total inelastic-scattering cross section in a solid can be much smaller, by a factor of up to about 4, than these cross sections for the corresponding free atoms. As a result, the actual DCSs in a solid at energies less than 1 keV might be closer to the atomic DCSs obtained from the DHF potential than suggested by the comparisons of Figs. 17–22.

We comment that IMFPs determined from both relative and absolute EPES measurements agree with IMFPs calculated from experimental optical data for solid Al, Si, Ni, Cu, Ge, Ag, and Au with an average mean deviation of 17.4% for electron energies between 50 eV and 5 keV.[117] Most of the IMFPs from the EPES measurements were larger than the calculated IMFPs for Al, Si, and Ge, while the reverse was true for Ni, Ag, and Au. There were no consistent systematic deviations as a function of electron energy, although it is possible that any such deviations could have been masked by varying effects of surface excitations and surface roughness in individual experiments. A more recent analysis of IMFPs from relative EPES experiments for 24 elemental solids has shown that the description of elastic-backscattered intensities using atomic DCSs is satisfactory for energies above about 200 eV.[132]

Finally, we note that calculated angular distributions of elastically backscattered electrons from Au surfaces (obtained with atomic DCSs calculated from the TFD potential) deviated considerably from measured distributions for energies below 200 eV.[49] The calculated and measured energy dependencies of the elastic-backscattered intensity from Au within the solid angle of a retarding-field analyzer are different for energies below 300 eV.[49] Similar effects have been found with other elements.[24,133] We therefore conclude from these observations and the discussion of IMFPs obtained from EPES measurements that DCSs calculated from atomic potentials appear to be at least empirically useful for simulations of electron transport in solids for electron energies above about 300 eV. At lower energies, the simulations may provide useful but more approximate guides. In addition, measurements that depend on ratios of atomic DCSs (such as relative EPES measurements) can give reliable results (such as IMFPs) down to at least 200 eV.

11. Summary

We have analyzed calculations of DCSs by the relativistic partial-wave expansion method from two commonly used potentials for elastic scattering of electrons with energies be-

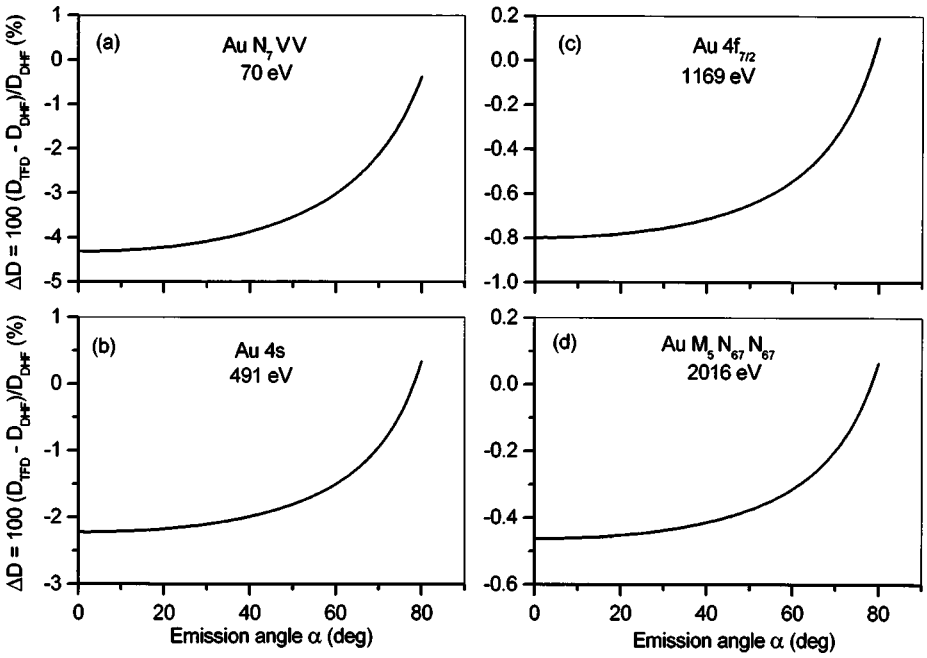

FIG. 33. Percentage differences, ΔD, between the mean escape depths for gold calculated using the TFD and DHF potentials [from Eq. (41)] as a function of emission angle for the two photoelectron lines and two Auger-electron lines in gold shown in Fig. 32.

tween 50 eV and 10 keV by neutral atoms. Calculated cross sections have been used for many applications because they are available for all elements and for a wide range of electron energies, as indicated in Table 1; in contrast, DCSs have been measured for a limited number of atoms and electron energies. Different methods have been used for the cross-section calculations (Tables 1 and 2) and, as a result, there are numerical differences in the cross-section data available in different tabulations and databases.[1–12] We note here that an additional database is available on a web site,[134] but few details of the calculations are available.[135]

We compared DCSs that were calculated from the TFD and the DHF potentials; cross sections from the latter potentials are considered more accurate because these potentials were obtained from DHF electron densities computed self-consistently.[52] These cross sections were obtained from two NIST databases for which the TFD[10] and DHF[12] potentials had been employed. Our comparisons were made for six elements spanning a wide range of atomic numbers (H, Al, Ni, Ag, Au, and Cm) and for electron energies of 100, 500, 1000, and 10 000 eV because these energies were common to both databases. While the DCSs from the two potentials had similar shapes and magnitudes, pronounced deviations (that could be as large as 70%) occurred for small scattering angles for Al, Ag, Au, and Cm. In addition, there were considerable differences in the DCSs in the vicinity of scattering angles for which there were deep minima in the DCSs. At these angles, the differences could reach 400%, although at other angles the differences were typically less than 20%. The deviations between the DCSs from the two potentials decrease with increasing electron energy. A slight oscillatory structure in the DCSs for H from the TFD potential was associated with truncation of the TFD potential at a relatively small radius.

Another factor that could lead to differences in DCSs from different sources is the choice of approximation used for the exchange interaction. We compared DCSs from two databases[11,12] in which the same DHF potential had been used (for H, Al, Ni, Ag, Au, and Cm) in the DCS calculations but different procedures had been adopted for the exchange correction. Berger and Seltzer[11] used the Riley and Truhlar[75] approximation while Jablonski *et al.*[12] used the Furness and McCarthy[64] correction. These comparisons were made for electron energies of 1 and 10 keV. For elements and energies where there are no deep minima in the DCSs, the differences between DCSs from the two databases are very small. For H, Al, Ni, and Ag, the differences generally do not exceed 0.02% although larger differences occurred for scattering angles near 180°; for example, a deviation of -0.28% was found for H at 10 keV. For Au and Cm, differences of up to -0.3% and $\pm 1\%$, respectively, were found at scattering angles where there were deep minima in the DCSs. We conclude that the exchange corrections of Riley and Truhlar and of Furness and McCarthy gave essentially equivalent results. We also note that the magnitude of the exchange correction on the DCS can be substantial. The differences between DCSs for Ag, Au, and Cm at 1000 eV can exceed 35% while differences between DCSs for H, Al, and Ni can be up to 5%. The larger deviations occur at scattering angles where there are deep minima in the DCSs.

We compared calculated DCSs from the TFD[10] and DHF[12] potentials with measured DCSs for six elements (He, Ne, Ar, Kr, Xe, and Hg) at energies between 50 and 3000 eV. For these elements, the measurements were relatively simple and there were generally two or more independent measurements available for the chosen electron energies. The consistency of the measured DCSs is typically within $\pm 25\%$, although larger deviations occur in some cases. For argon, the element with the largest number of measurements, there is excellent agreement between the measured DCSs at 2 and 3 keV and

the corresponding calculated DCSs from both the TFD and DHF potentials. At lower energies, the measured DCSs generally agree better with DCSs from the DHF potential than those from the TFD potential, particularly in the positions and the magnitudes of the deep minima, although the measured DCSs are smaller than the calculated DCSs at other scattering angles. For other elements, the measured DCSs agree better with the DCSs from the DHF potential than the TFD potential at the highest available energy; deviations between the measured DCSs and the DCSs from the DHF potential typically become larger with decreasing electron energy, and can be as much as a factor of 2. There is also often better agreement between the measured DCSs and the DCSs from the DHF potential in the vicinity of deep minima. The increasing differences between measured DCSs and the DCSs from the DHF potential generally found with decreasing energy below 1 keV are believed to be due to the neglect of absorption effects in the calculational algorithm. For scattering angles less than about 25°, the measured DCSs at energies less than about 500 eV are larger than the DCSs from the DHF potential, but the range of scattering angles where positive deviations occur gets smaller with increasing energy. These deviations are associated with the neglect of an atomic polarizability correction in the calculations. Consideration of the absorption and polarizibility corrections (an appreciably more complex calculation) leads to improved agreement between measured and calculated DCSs for He and Ar.[107,110]

The transport cross section, obtained from an integral of the DCS that emphasizes large-angle elastic scattering, is a useful parameter in simulations of electron transport in solids. We have compared TCSs derived from DCSs calculated from the TFD and DHF potentials for H, Al, Ni, Ag, Au, and Cm. For energies above 200 eV, the largest differences between the TCSs from the two potentials is for H where the deviation is about 20%. For Al, Ni, and Ag, the differences in TCSs are less than 5% for energies above 200 eV. For Au and Cm, the differences can exceed 20% for energies less than 1000 eV, but for higher energies the differences are less than 5%. For energies between 50 and 200 eV, the differences are generally larger and can be up to 43% (for Ni at 50 eV).

We have also examined the extent to which three quantities derived from DCSs varied depending on whether the DCSs were obtained from the TFD or DHF potential. First, we considered elastic-backscattered intensities from an overlayer film on a surface. As an example, calculations were made of the dependence of these intensities on film thickness for an Au film on a Ni substrate. Comparisons with two sets of experimental data for slightly different configurations at two electron energies (500 and 1000 eV) were inconclusive. For one configuration, the measured intensities at both energies agreed better with intensities calculated using DCSs from the TFD potential. For the other configuration, a similar result was found at 1000 eV while better agreement was found at 500 eV with intensities computed using DCSs from the DHF potential.

Second, we considered the determination of electron IMFPs by EPES. IMFPs can be obtained from either relative or absolute EPES measurements. For relative EPES experiments, we examined a ''worst-case'' example of a material, configuration, and energy for which there was a deep minimum in the DCS (for a single elastic-scattering event). We selected Au, a scattering angle of 155°, and electron energies of 500 and 1000 eV for this example, as there is a deep minimum in the DCS for Au at 500 eV close to this scattering angle and there are appreciable differences in the DCSs from the TFD and DHF potentials; there were smaller differences at 1000 eV. We found that Au IMFPs derived from the use of DCSs from the TFD potential (and use of a Ni reference material and a hemispherical electron energy analyzer with small angular acceptance) were 17.1% and 12.1% less than the IMFPs obtained using DCSs from the DHF potential at 500 and 1000 eV, respectively. In another example, involving EPES measurements from an AuCu alloy, an Au reference material, an analyzer with a large angular acceptance, and four energies between 200 and 2000 eV, IMFPs with DCSs from the TFD potential were about 6% larger than those found using DCSs from the DHF potential at 200 and 500 eV; the differences at 1000 and 2000 eV were 3.26% and 1.27%, respectively. For absolute EPES experiments, we considered first the case of Au, measurements with an analyzer of large angular acceptance, and energies of 500 and 1000 eV. IMFPs with DCSs from the TFD potential were 10.0% and 1.31% less than those found with the DHF potential at energies of 500 and 1000 eV, respectively. In another example involving Ni, an analyzer of large acceptance angle, and energies between 250 and 1500 eV, differences between IMFPs found with the TFD potential and those from the DHF potential were 2.36%, 6.42%, 5.66%, and 2.93% at energies of 250, 500, 1000, and 1500 eV, respectively. In these four examples, the differences between IMFPs found using DCSs from the TFD and DHF potentials varied between 1.27% and 17.1%. We conclude that, for some materials, configurations, and electron energies, IMFPs derived from EPES experiments and simulations with DCSs from the DHF potential could differ significantly from those obtained using DCSs from the TFD potential; in other cases, the differences would be comparable to the precision of the Monte Carlo simulation.

Third, we considered MEDs for the signal electrons in AES and XPS. As an example, we determined MEDs for two photoelectron lines (with excitation by Mg $K\alpha$ x rays) and two Auger-electron lines of Au where the electron energies range from 70 to 2016 eV. MEDs were calculated from a formalism in which the TCS is the only parameter describing the strength of elastic-electron scattering. Differences between MEDs obtained from TCSs derived from the TFD and DHF potentials for normal electron emission varied between 4.3% at 70 eV and 0.5% at 2016 eV, and become smaller with increasing emission angle. Since Au is an element for which elastic-scattering effects are relatively strong, we conclude that MEDs for signal electrons in AES and XPS will not change significantly if TCSs from the DHF potential

are used in the calculation instead of those from the TFD potential.

Calculated DCSs for neutral atoms have been extensively used in simulations of electron transport in solids for a large variety of applications. Although the interaction potential in a solid will be clearly different from that for a free atom, many calculated parameters of interest (e.g., TCSs, electron attenuation lengths, electron backscattered intensities, and signal intensities in AES and XPS) depend on ''large-angle'' scattering in the solid for which changes of potential are often of lesser significance than other sources of uncertainty. Our comparisons of measured and calculated DCSs for atoms have shown, however, that measured DCSs can be much less (sometimes by a factor of 2) than the calculated DCSs for energies less than 1 keV. Nevertheless, we point out that IMFPs from absolute EPES experiments agree satisfactorily with IMFPs computed from experimental optical data. The latter IMFPs have been independently tested by other experiments. We therefore believe that IMFPs from absolute EPES experiments are unlikely to have a systematic error of as much as a factor of two for electron energies between 150 eV and 1 keV. We speculate that the absorption correction to the DCSs for a solid may be less than that for the corresponding atom. While further work is needed to understand why atomic DCSs are useful for solids, we conclude that the atomic DCSs are empirically useful for simulations of electron transport in solids for energies above about 300 eV. These DCSs can also be useful for energies down to at least 200 eV where relative measurements are made (such as relative EPES measurements).

A new NIST database of electron elastic-scattering cross sections[12] implements the most accurate physical modeling that can be utilized for all atoms and that can be handled on a systematic basis (i.e., it has a robust computational scheme that can be reproduced by anyone wishing to repeat the calculations). This approach necessarily prevents the consideration of second-order effects whose proper theoretical description would require detailed knowledge of the atomic structure beyond the electron-charge distribution of the ground state. Even the latter had to be slightly ''manipulated'' (through a spherical average) for open-shell configurations to obtain a central interaction potential. As a result, the required robustness and generality of the numerical calculational algorithm mean a certain sacrifice in the accuracy of DCS values from the database. Nevertheless, the availability of partial-wave numerical DCSs from a well-defined physical model is a necessary step towards the systematization of more elaborate calculations. For instance, the effects of any improvements in the basic physics will be easier to quantify when expressed as corrections to the static-field DCSs available now.[12]

12. Acknowledgments

The authors wish to thank Dr. A. Dubus, Dr. M. Inokuti, Dr. D. Joy, Dr. D. Liljequist, Dr. S. Manson, Dr. S. Seltzer, Dr. R. Shimizu, and Dr. S. Tougaard for their many useful comments and suggestions on a previous draft of this paper.

13. References

[1] M. Fink and A. C. Yates, At. Data **1**, 385 (1970).
[2] M. Fink and J. Ingram, At. Data **4**, 129 (1972).
[3] D. Gregory and M. Fink, At. Data Nucl. Data Tables **14**, 39 (1974).
[4] M. E. Riley, C. J. MacCallum, and F. Biggs, At. Data Nucl. Data Tables **15**, 443 (1975).
[5] L. Reimer and B. Lödding, Scanning **6**, 128 (1984).
[6] Z. Czyzewski, D. O. MacCallum, A. Romig, and D. C. Joy, J. Appl. Phys. **68**, 3066 (1990); web address: http://pciserver.bio.utk.edu/metrology
[7] M. J. Berger, S. M. Seltzer, R. Wang, and A. Schechter, *Elastic Scattering of Electrons and Positrons by Atoms: Database ELAST*, NIST Internal Report NISTIR 5188 (National Institute of Standards and Technology, Gaithersburg, MD, 1993).
[8] A. Jablonski and S. Tougaard, *NIST Elastic-Electron-Scattering Cross-Section Database*, Version 1.0, Standard Reference Data Program Database 64 (National Institute of Standards and Technology, Gaithersburg, MD, 1996).
[9] R. Mayol and F. Salvat, At. Data Nucl. Data Tables **65**, 55 (1997).
[10] A. Jablonski and C. J. Powell, *NIST Electron Elastic-Scattering Cross-Section Database*, Version 2.0, Standard Reference Data Program Database 64 (National Institute of Standards and Technology, Gaithersburg, MD, 2000).
[11] M. J. Berger and S. M. Seltzer, *Database of Cross Sections for the Elastic Scattering of Electrons and Positrons by Atoms*, NIST Internal Report NISTIR 6573 (National Institute of Standards and Technology, Gaithersburg, MD, 2000); web address: http://www.nea.fr/abs/htm1/dlc-0208.html.
[12] A. Jablonski, F. Salvat, and C. J. Powell, *NIST Electron Elastic-Scattering Cross-Section Database*, Version 3.0, Standard Reference Data Program Database 64 (National Institute of Standards and Technology, Gaithersburg, MD, 2002); web address: http://www.nist.gov/srd/nist64.htm
[13] S. Ichimura, M. Aratama, and R. Shimizu, J. Appl. Phys. **51**, 2853 (1980).
[14] R. Shimizu and S. Ichimura, ''Quantitative Analysis by Auger Electron Spectroscopy'' The Toyota Foundation Research Report No. I-006, No. 76-0175, Tokyo, 1981.
[15] S. Ichimura and R. Shimizu, Surf. Sci. **112**, 386 (1981).
[16] R. Shimizu, Japan. J. Appl. Phys. **22**, 1631 (1983).
[17] R. Shimizu and Z.-J. Ding, Rep. Prog. Phys. **55**, 487 (1992).
[18] Z.-J. Ding, R. Shimizu, and K. Goto, J. Appl. Phys. **76**, 1187 (1994).
[19] Z.-J. Ding and R. Shimizu, Scanning **18**, 92 (1996).
[20] S. Tanuma, S. Ichimura, and K. Goto, Surf. Interface Anal. **30**, 212 (2000).
[21] A. Jablonski, J. Gryko, J. Kraaer, and S. Tougaard, Phys. Rev. B **39**, 61 (1989).
[22] A. Jablonski, Phys. Rev. B **43**, 7546 (1991).
[23] W. S. M. Werner, W. H. Gries, and H. Stori, Surf. Interface Anal. **17**, 693 (1991).
[24] W. S. M. Werner, I. S. Tilinin, and M. Hayek, Phys. Rev. B **50**, 4819 (1994).
[25] W. S. M. Werner, Surf. Sci. **257**, 319 (1991).
[26] W. S. M. Werner, Phys. Rev. B **52**, 2964 (1995).
[27] A. Jablonski, C. Jansson, and S. Tougaard, Phys. Rev. B **47**, 7420 (1993).
[28] L. Zommer, B. Lesiak, and A. Jablonski, Phys. Rev. B **47**, 13759 (1993).
[29] A. Jablonski and J. Zemek, Phys. Rev. B **48**, 4799 (1993).
[30] A. Jablonski and C. J. Powell, Phys. Rev. B **50**, 4739 (1994).
[31] A. Jablonski, I. S. Tilinin, and C. J. Powell, Phys. Rev. B **54**, 10927 (1996).
[32] A. Jablonski, Phys. Rev. B **58**, 16470 (1998).
[33] A. Jablonski and C. J. Powell, Surf. Sci. **463**, 29 (2000).
[34] C. Robert, S. Zuber, L. Bideux, S. Merle, B. Gruzza, V. Nehasil, and V. Matolin, Surf. Interface Anal. **30**, 341 (2000).
[35] R. Vidal, R. A. Baragiola, and J. Ferron, J. Appl. Phys. **80**, 5653 (1996).
[36] A. R. Jackson, M. M. El Gomati, J. A. D. Matthew, and P. J. Cumpson, Surf. Interface Anal. **25**, 341 (1997).

[37] J. A. D. Matthew, A. R. Jackson, and M. M. El Gomati, J. Electron Spectrosc. Relat. Phenom. **85**, 205 (1997).
[38] P. J. Cumpson and M. P. Seah, Surf. Interface Anal. **25**, 430 (1997).
[39] J. M. Fernandez-Varea, D. Liljequist, S. Csillag, R. Raty, and F. Salvat, Nucl. Instrum. Methods. Phys. Res. B **108**, 35 (1996).
[40] E. Acosta, X. Llovet, E. Coleoni, J. A. Riveros, and F. Salvat, J. Appl. Phys. **83**, 6038 (1998).
[41] E. Acosta, X. Llovet, E. Coleoni, F. Salvat, and J. A. Riveros, X-Ray Spectrometry **28**, 121 (1999).
[42] E. Acosta, X. Llovet, and F. Salvat, Appl. Phys. Lett. **80**, 3228 (2002).
[43] M. Dapor, J. Appl. Phys. **79**, 8406 (1996).
[44] M. Dapor and A. Miotello, Eur. Phys. J. Appl. Phys. **5**, 143 (1999).
[45] M. Dapor, Eur. Phys. J. Appl. Phys. **18**, 155 (2002).
[46] D. W. Walker, Adv. Phys. **20**, 257 (1971).
[47] N. F. Mott, Proc. R. Soc. London, Ser. A **124**, 425 (1929).
[48] F. Calogero, *Variable Phase Approach to Potential Scattering* (Academic, New York, 1967), Chaps. 3 and 17.
[49] A. Jablonski, Phys. Rev. B **43**, 7546 (1991).
[50] P. Gombas, *Die Statistische Theorie des Atoms und ihre Anwendungen* (Springer, Wien, 1949), p. 77.
[51] P. Gombas, in *Handbuch der Physik*, edited by S. Flugge (Springer, Berlin, 1956), Vol. 36, p. 109.
[52] J. P. Desclaux, Comput. Phys. Commun. **9**, 31 (1977); Erratum: **13**, 71 (1977).
[53] S.-R. Lin, N. Sherman, and J. K. Percus, Nucl. Phys. **45**, 492 (1963).
[54] P. J. Bunyan and J. K. Schonfelder, Proc. Phys. Soc. (London) **85**, 455 (1965).
[55] A. Jablonski and S. Tougaard, Surf. Interface Anal. **22**, 129 (1994).
[56] L. Lapidus and J. H. Seinfeld, *Numerical Solution of Ordinary Differential Equations* (Academic, New York, 1971), p. 72.
[57] R. A. Bonham and T. G. Strand, J. Chem. Phys. **39**, 2200 (1963).
[58] A. Jablonski, Physica A **183**, 361 (1992).
[59] L. H. Thomas, J. Chem. Phys. **22**, 1758 (1954).
[60] A. Jablonski, J. Comput. Phys. **111**, 256 (1994).
[61] F. Salvat and R. Mayol, Comput. Phys. Commun. **74**, 358 (1993).
[62] W. Bühring, Z. Phys. **187**, 180 (1965).
[63] F. Salvat and R. Mayol, Comput. Phys. Commun. **62**, 65 (1991).
[64] J. B. Furness and I. E. McCarthy, J. Phys. B: At. Mol. Phys. **6**, 2280 (1973).
[65] M. Abramowitz and I. A. Stegun, *Handbook of Mathematical Functions* (Dover, New York, 1974).
[66] I. S. Tilinin, A. Jablonski, and W. S. M. Werner, Prog. Surf. Sci. **52**, 193 (1996), and references therein.
[67] W. S. M. Werner, Surf. Interface Anal. **31**, 141 (2001), and references therein.
[68] I. S. Tilinin and W. S. M. Werner, Phys. Rev. B **46**, 13739 (1992).
[69] I. S. Tilinin, A. Jablonski, J. Zemek, and S. Hucek, J. Electron Spectrosc. Relat. Phenom. **87**, 127 (1997).
[70] V. I. Nefedov, J. Electron Spectrosc. Relat. Phenom. **100**, 1 (1999).
[71] C. J. Powell and A. Jablonski, Surf. Interface Anal. **33**, 211 (2002).
[72] A. Jablonski and C. J. Powell, Surface Sci. Rep. **47**, 33 (2002).
[73] A. Jablonski and C. J. Powell, J. Vac. Sci. Technol. A **21**, 274 (2003).
[74] International Standard ISO 18115, *Surface Chemical Analysis—Vocabulary* (International Organization for Standardization, Geneva, 2001).
[75] M. E. Riley and D. G. Truhlar, J. Chem. Phys. **83**, 2182 (1975).
[76] L. J. Kieffer and G. H. Dunn, Rev. Mod. Phys. **38**, 1 (1966).
[77] C. E. Kuyatt, in *Methods of Experimental Physics: Atomic and Electron Physics: Atomic Interactions*, edited by B. Bederson and W. L. Fite (Academic, New York, 1968), Vol. 7A, p. 1.
[78] S. Trajmar, D. F. Register, and A. Chutjian, Phys. Rep. **97**, 219 (1983).
[79] S. Trajmar and J. W. McConkey, in *Advances in Atomic, Molecular, and Optical Physics*, edited by B. Bederson and H. Walther (Academic, New York, 1994), Vol. 33, p. 63.
[80] M. Inokuti, in *Photon and Electron Interactions with Atoms, Molecules and Ions*, edited by Y. Itikawa, Group I and Vol. 17A of Landolt-Börnstein Numerical Data and Functional Relationships in Science and Technology, New Series (Springer, Berlin, 2000), Chaps. 2.1, 2.2, and 2.3.
[81] J. P. Bromberg, J. Chem. Phys. **61**, 963 (1974).
[82] J. W. McConkey and J. A. Preston, J. Phys. B: At. Mol. Phys. **8**, 63 (1975).
[83] S. C. Gupta and J. A. Rees, J. Phys. B: At. Mol. Phys. **8**, 1267 (1975).
[84] M. V. Kurepa and L. Vuskovic, J. Phys. B: At. Mol. Phys. **8**, 2067 (1975).
[85] R. H. J. Jansen, F. J. de Heer, H. J. Luyken, B. van Wingerden, and H. J. Blaauw, J. Phys. B: At. Mol. Phys. **9**, 185 (1976).
[86] D. F. Register, S. Trajmar, and S. K. Srivastava, Phys. Rev. A **21**, 1134 (1980).
[87] R. W. Wagenaar, A. de Boer, T. van Tubergen, J. Los, and F. J. de Heer, J. Phys. B: At. Mol. Phys. **19**, 3121 (1986).
[88] M. J. Brunger, S. J. Buckman, L. J. Allen, I. E. McCarthy, and K. Ratnavelu, J. Phys. B: At. Mol. Opt. Phys. **25**, 1823 (1992).
[89] R. D. DuBois and M. E. Rudd, J. Phys. B: At. Mol. Phys. **9**, 2657 (1976).
[90] S. C. Gupta and J. A. Rees, J. Phys. B: At. Mol. Phys. **8**, 417 (1975).
[91] J. F. Williams and A. Crowe, J. Phys. B: At. Mol. Phys. **10**, 2233 (1975).
[92] R. Panajotovic, D. Filipovic, B. Marinkovic, V. Pejcev, M. Kurepa, and L. Vuskovic, J. Phys. B: At. Mol. Opt. Phys. **30**, 5877 (1997).
[93] D. Cvejanovic and A. Crowe, J. Phys. B: At. Mol. Opt. Phys. **30**, 2873 (1997).
[94] S. K. Srivastava, H. Tanaka, A. Chutjian, and S. Trajmar, Phys. Rev. A **23**, 2156 (1981).
[95] L. Vuskovic and M. V. Kurepa, J. Phys. B: At. Mol. Phys. **9**, 837 (1976).
[96] J. F. Williams and B. A. Willis, J. Phys. B: At. Mol. Phys. **8**, 1670 (1975).
[97] L. Dou, W. E. Kauppila, C. K. Kwan, and T. S. Stein, Phys. Rev. Lett. **68**, 2913 (1992).
[98] I. Iga, L. Mu-Tao, J. C. Nogueira, and R. S. Barbieri, J. Phys. B: At. Mol. Phys. **20**, 1095 (1987).
[99] A. Danjo, J. Phys. B: At. Mol. Opt. Phys. **21**, 3759 (1988).
[100] R. H. J. Jansen and F. J. de Heer, J. Phys. B: At. Mol. Phys. **9**, 213 (1976).
[101] H. Nishimura, T. Matsuda, and A. Danjo, J. Phys. Soc. Jpn. **56**, 70 (1987).
[102] T. Ester and J. Kessler, J. Phys. B: At. Mol. Opt. Phys. **27**, 4295 (1994).
[103] G. Holtkamp, K. Jost, F. J. Peitzmann, and J. Kessler, J. Phys. B: At. Mol. Phys. **20**, 4543 (1987).
[104] R. Panajotovic, V. Pejcev, M. Kosntantinovic, D. Filipovic, V. Bocvarski, and B. Marinkovic, J. Phys. B: At. Mol. Opt. Phys. **26**, 1005 (1993).
[105] J. P. Bromberg, J. Chem. Phys. **51**, 4117 (1969).
[106] F. J. Peitzmann and J. Kessler, J. Phys. B: At. Mol. Opt. Phys. **23**, 4005 (1990).
[107] F. W. Byron, Jr. and C. J. Joachain, Phys. Rep. **34**, 233 (1977).
[108] G. Staszewska, D. W. Schwenke, and D. G. Truhlar, Phys. Rev. A **29**, 3078 (1984).
[109] L. I. Schiff, *Quantum Mechanics*, 3rd ed. (McGraw-Hill Kogakusha, Tokyo, 1968), pp. 129–138.
[110] F. Salvat, Phys. Rev. A **68**, 012708 (2003).
[111] D. Liljequist (private communication).
[112] M. T. Elford and S. J. Buckman, in *Photon and Electron Interactions with Atoms, Molecules and Ions*, edited by Y. Itikawa, Group I and Vol. 17A, Landolt-Börnstein Numerical Data and Functional Relationships in Science and Technology, New Series (Springer, Berlin, 2000), Chap. 2.5.
[113] J. W. McConkey and J. A. Preston, J. Phys. B: At. Mol. Phys. **8**, 63 (1975).
[114] D. Andrick and A. Bitsch, J. Phys. B: At. Mol. Phys. **8**, 393 (1975).
[115] A. Jablonski, H. S. Hansen, C. Jansson, and S. Tougaard, Phys. Rev. B **45**, 3694 (1992).
[116] A. Jablonski, J. Zemek, and P. Jiricek, Surf. Interface Anal. **31**, 825 (2001).
[117] C. J. Powell and A. Jablonski, J. Phys. Chem. Ref. Data **28**, 19 (1999).
[118] M. Krawczyk, L. Zommer, A. Jablonski, C. Robert, J. Pavluch, L. Bideux, and B. Gruzza, Surf. Interface Anal. **31**, 415 (2001).
[119] D. Zeze, L. Bideux, B. Gruzza, F. Golek, D. Danko, and S. Mroz, Vacuum **48**, 399 (1997).
[120] W. Dolinski, S. Mroz, and M. Zagorski, Surf. Sci. **200**, 361 (1988).
[121] Standard E 673-01, *Annual Book of ASTM Standards 2002* (ASTM, West Conshohocken, PA, 2002), Vol. 3.06, p. 755.
[122] S. Chandrasekhar, *Radiative Transfer* (Dover, New York, 1960), Chap. 5.
[123] M. P. Seah, Surf. Interface Anal. **20**, 243 (1993).
[124] A. Jablonski and C. J. Powell, J. Electron Spectrosc. Relat. Phenom. **100**, 137 (1999).
[125] H. Raith, Acta Crystall. A **24**, 85 (1968).
[126] M. P. Seah, I. S. Gilmore, and S. J. Spencer, Surf. Interface Anal. **31**, 778 (2001).
[127] S. Tanuma, C. J. Powell, and D. R. Penn, Surf. Interface Anal. **21**, 165 (1994).
[128] C. J. Powell and A. Jablonski, J. Vac. Sci. Technol. A **19**, 2604 (2001).

[129] J. Rundgren, Phys. Rev. B **59**, 5106 (1999).
[130] S. Tanuma, C. J. Powell, and D. R. Penn, Surf. Interface Anal. **17**, 911 (1991).
[131] S. Tanuma, C. J. Powell, and D. R. Penn, Surf. Interface Anal. **25**, 25 (1997).
[132] W. S. M. Werner, C. Tomastik, T. Cabela, G. Richter, and H. Stori, J. Electron Spectrosc. Relat. Phenom. **113**, 127 (2001).
[133] A. Jablonski, C. Jansson, and S. Tougaard, Phys. Rev. B **47**, 7420 (1993).
[134] Web address: http://www.ioffe.rssi.ru/ES
[135] L. A. Bakaleinikov and V. V. Tretyakov, Scanning **17**, 243 (1995).